DYNAMICS AND FUNCTION OF THE TEAR FILM IN RELATION TO THE BLINK CYCLE

By

RJ Braun, PE King-Smith, CG Begley, Longfei Li and NR Gewecke

IMA Preprint Series #2429

(August 2014)

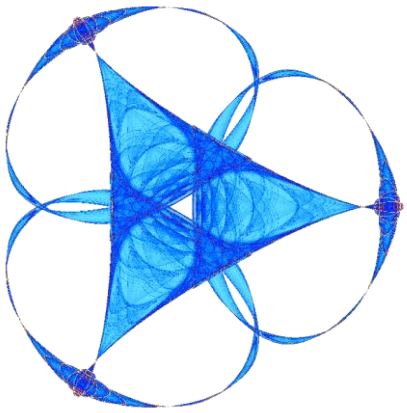

INSTITUTE FOR MATHEMATICS AND ITS APPLICATIONS
UNIVERSITY OF MINNESOTA
400 Lind Hall
207 Church Street S.E.
Minneapolis, Minnesota 55455-0436
Phone: 612-624-6066 Fax: 612-626-7370
URL: http://www.ima.umn.edu

Dynamics and Function of the Tear Film in Relation to the Blink Cycle

RJ Braun,[1,4,6] PE King-Smith,[2] CG Begley,[3] Longfei Li[1] and NR Gewecke[1,5]

1. Department of Mathematical Sciences, University of Delaware, Newark, DE, 19716 USA ; braun@math.udel.edu; longfei@math.udel.edu
2. College of Optometry, The Ohio State University, 338 W 10th Avenue, Columbus, OH, USA, 43210; king-smith.1@osu.edu
3. School of Optometry, Indiana University, 800 East Atwater Avenue, Bloomington, IN, USA 47405; cbegley@indiana.edu
4. Institute for Mathematics and its Applications, University of Minnesota, Minneapolis, MN, 55455 USA
5. Current address: Department of Technology and Mathematics, Dalton State College, 650 College Drive, Dalton, GA 30720; ngewecke@daltonstate.edu
6. Corresponding Author: Department of Mathematical Sciences, University of Delaware, Newark, DE, 19716 USA ; braun@math.udel.edu; +1-302-831-1869

Submission date: August 12, 2014

Abstract

Great strides have recently been made in quantitative measurements of tear film thickness and thinning, mathematical modeling thereof and linking these to sensory perception. This paper summarizes recent progress in these areas and reports on new results. The complete blink cycle is used as a framework that attempts to unify the results that are currently available. Understanding of tear film dynamics is aided by combining information from different imaging methods, including fluorescence, retroillumination and a new high-speed stroboscopic imaging system developed for studying the tear film during the blink cycle. During the downstroke of the blink, lipid is compressed as a thick layer just under the upper lid which is often released as a narrow thick band of lipid at the beginning of the upstroke. "Rippling" of the tear film/air interface due to motion of the tear film over the corneal surface, somewhat like the flow of water in a shallow stream over a rocky streambed, was observed during lid motion and treated theoretically here. New mathematical predictions of tear film osmolarity over the exposed ocular surface and in tear breakup are presented; the latter is closely linked to new *in vivo* observations. Models include the effects of evaporation, osmotic flow through the cornea and conjunctiva, quenching of fluorescence, tangential flow of aqueous tears and diffusion of tear solutes and fluorescein. These and other combinations of experiment and theory increase our understanding of the fluid dynamics of the tear film and its potential impact on the ocular surface.

Keywords: tear film, tear film dynamics, lipid layer, tear break-up, tear hyperosmolarity

Table of Contents

1. Introduction 3

1.1 Images of a blink 4

1.2 Four parts of the blink 6

2 Downstroke 7

2.1 Experimental observations 8

2.2 Linearized theory of ripples 10

2.3 Nonlinear thin film theory 12

2.4 Comparison between the theories 14

3 Turning point 15

4 Upstroke 16

4.1 The lid motion and the tear film 16

4.2 Upward drift 18

4.3 Early lipid spreading phenomena 19

4.4 Release of lipid 20

5 Interblink 22

5.1 Experimental results for tear film optical quality improvement 22

5.2 Leveling 23

5.2.1 Leveling in the absence of evaporation 23

5.2.2 Leveling in the presence of evaporation 24

5.3 Solutes: Osmolarity, Flourescein and Fluorescence 25

5.3.1 Measurements 25

5.3.2 Aspects of osmotic supply from the ocular surface 26

5.3.3 Theory and experiment for local flat spot dynamics 26

5.3.4 Theory over the exposed ocular surface 32

5.3.5 Tear film break up: experiment 36

5.3.6 Tear film break up: theory 39

5.3.7 Sensory perception experiments 43

5.3.8 Other observations of TBU 45

6. Summary and Future Directions 46

7. Appendices 49

7.1 Mathematical model parameters 49

7.2 FL equations and TF thinning 51

7.3 Tangential flow over a model rough corneal surface 53

7.4 Mathematical model for leveling 55

7.5 TF tangential flow with thinning and solutes 56

7.6 Eye-shaped domain models 57

Acknowledgements 58

References 59

1. Introduction

The human tear film is a very thin layer of fluid, approximately 3 microns thick (King-Smith et al., 2000). Although thin, it provides a critical function in the eye's optical system and serves to nourish, protect and enhance the differentiation of surface epithelial cells (Bron et al., 2004; Govindarajan and Gipson, 2010; Montes-Mico et al., 2010; Tutt et al., 2000). When unstable, the tear film may stress and potentially alter the underlying ocular surface, resulting in a common condition known as dry eye (DE), which affects millions in the U.S and elsewhere (DEWS, 2007; Schaumberg et al., 2003; Uchino et al., 2011; Viso et al., 2009). However, despite the common occurrence of the DE condition, knowledge of tear film dynamics remains inadequate to understand fluid dynamics during the complete blink cycle, perhaps due to the rapidity of the changes taking place in the very thin film. This review combines recent imaging of tear film dynamics and other experimental measures with mathematical modeling of tear film parameters to deepen our understanding of the dynamic processes taking place in the tear film during the complete blink cycle.

Tear film instability, which includes both rapid tear thinning and tear break-up (TBU), is considered a core mechanism of DE, along with tear film hyperosmolarity (DEWS, 2007). Theoretically, tear film instability occurs due to increased evaporation and leads to increased tear film osmolarity, which stresses the ocular surface and leads to a vicious cycle of inflammation and hyperalgesia (Baudouin et al., 2013; DEWS, 2007). Recent imaging of TBU combined with sensory measures have linked TBU to discomfort, pain and increased DE-like symptoms and suggested that tear film osmolarity may reach 800-900 MOsM within local areas of TBU (Liu et al., 2009). However, tear film osmolarity is difficult to measure directly over the ocular surface and is currently estimated by sampling tears from the lower meniscus (Bron et al., 2014; Lemp et al., 2011). Mathematical modeling of changes in tear film fluorescence within areas of tear film instability has provided a method to estimate tear film hyperosmolarity within the same regions over the ocular surface (Braun et al., 2014). In this paper, we add to previous results from mathematical models of TBU (Peng et al., 2014) and we present new results for osmolarity all over the exposed ocular surface. We also include mathematical models for the fluorescent intensity, in order to help understand this process quantitatively and how fluorescence is related to the osmolarity. Since solute concentrations are not measured outside the meniscus, these quantitative estimates may currently be the best source of concentrations available.

The tear film is usually studied in the inter-blink period, where an unstable tear film quickly becomes evident as TBU progresses rapidly (Liu et al., 2006). This is measured clinically by fluorescein tear break-up time (TBUT), or the first appearance of a dark or "dry spot" after a blink (Norn, 1969). However, conditions within areas of TBU and predisposing factors in the tear film

have been difficult to measure experimentally, although theoretical mechanisms for TBU have been proposed (Fatt, 1991; Holly, 1973; Sharma and Ruckenstein, 1985). Recent experimental evidence, combined with mathematical modeling, points to an unequal distribution or composition of lipids and evaporation as driving mechanisms for TBU and thinning (Braun et al., 2014; King-Smith et al., 2013a; King-Smith et al., 2009; King-Smith et al., 2008).

The fullness of the blink may affect the stability of the tear film and its distribution in the inter-blink period (Harrison et al., 2008). Theoretically, the tear film is "painted on" by the upper lid with each blink. Surface tension acts to smooth the tear film, improving it as an optical surface. However, many blinks are partial, leaving a visible line or groove at the fullest extent of the blink (Himebaugh et al., 2009), which may affect the optics of the tear film if the groove occurs within the pupil. Recent experimental data and modeling of tear film thickness above and below the groove has shown that thickness is decreased above the groove compared to below. Theoretically, the groove is smoothed by leveling, which occurs faster with a thicker tear film.

Aside from the inter-blink period, the dynamics of the tear film is more difficult to study, presumably due to the difficulty in imaging the ocular surface and tear film surrounding a blink. Just after a blink, the lipid layer and tear film move upwards for approximately 1-2 seconds, theoretically driven by the unequal distribution of lipids following the blink (Berger and Corrsin, 1974; King-Smith et al., 2009; Owens and Phillips, 2001). Stroboscopic imaging of the lipid layer and tear film, presented here, has confirmed that tear film lipids tend to be relatively stable from blink to blink (Bron et al., 2004), and shown that a rippling pattern is visible in the tear film during the downstroke and upstroke of the blink. These findings underscore the need to investigate the tear film during the complete blink cycle to provide a broader understanding of tear film dynamics under normal conditions and pathologies such as DE.

This review of recent work presents a combination of experimental imaging of the tear film with mathematical modeling designed to provide additional understanding of tear film dynamics. Recently, there are increasing efforts in this direction resulting in increasing synergy between theoretical and experimental approaches. This review will touch on previous results from both approaches, and will introduce a number of new results. These new results highlight what we believe are profitable interactions of the theory and experiment so that each is better understood. The bulk of the review will present experimental results and the corresponding results and interpretation from mathematical models. Some speculation regarding less well-understood phenomena as well as possible future directions is included.

The principles of the Declaration of Helsinki were followed for all studies in this paper and the studies were approved by the respective Biomedical Institutional Review Boards of the Ohio State University and Indiana University. Informed consent was obtained from all subjects after explanation of the procedures involved in each study.

1.1 Images of a blink

The blinking process and tear film dynamics have been imaged with a variety of techniques. Doane (1980) hid a high speed camera behind a one-way mirror and filmed subjects relaxing while waiting for what they thought was the upcoming test. The images were subsequently hand

processed to reveal lid motion and speed as well as other aspects of blinking and tear supply and drainage (Doane, 1981). Progress in optics and computing has led to more automated approaches; we only cite a few of the possible studies (Cruz et al., 2011; Wu et al., 2014). Results from a new stroboscopic imaging system are presented here here to illustrate both the blink process and the dynamics of the tear film related to the blink cycle.

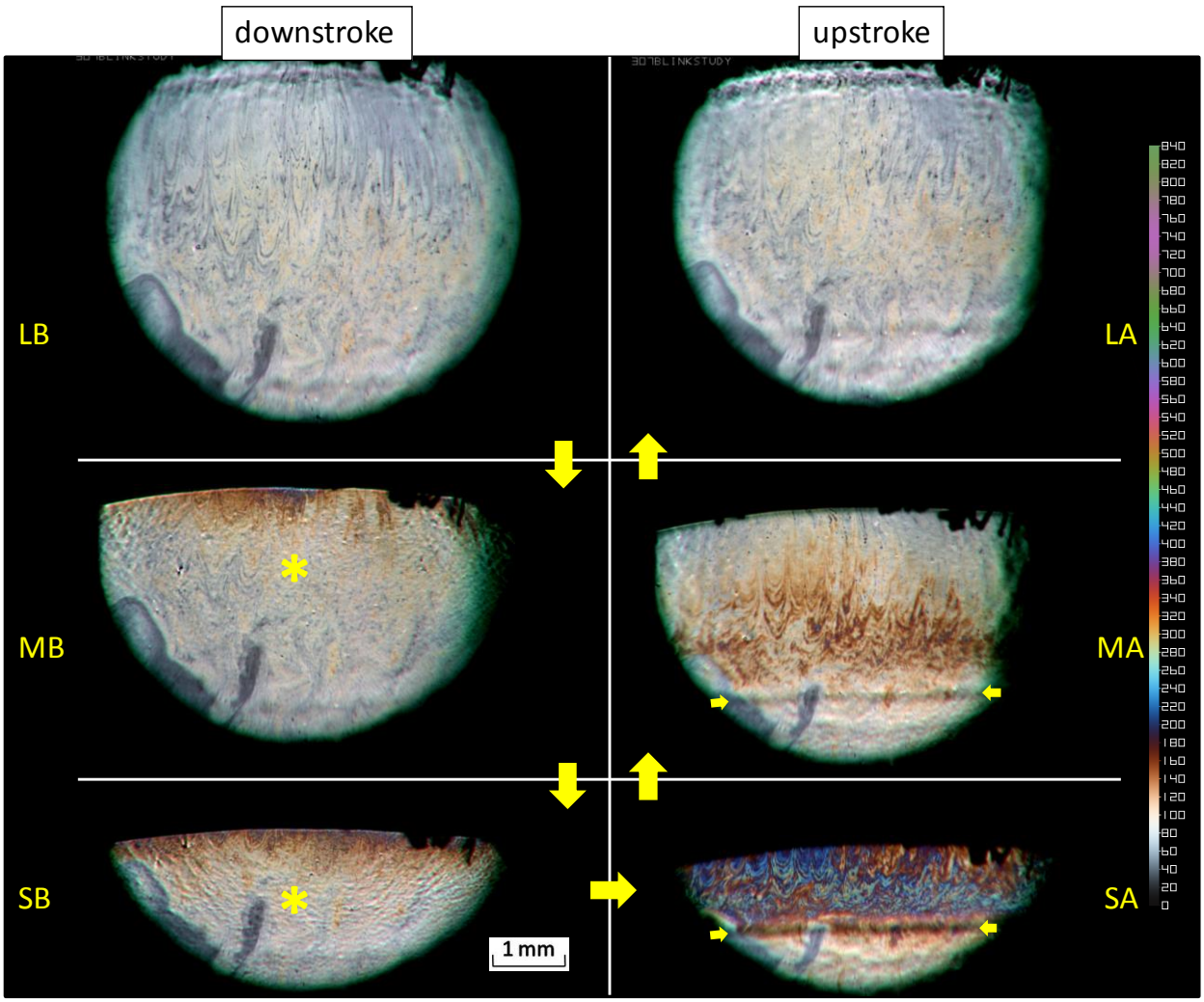

Fig. 1. A "blink composite" showing a series of images from a lipid imaging system that are arranged to show selected times from a partial blink. Right eye of 64 year old white female with DE disorder assessed by OSDI score (Schiffman et al., 2000). Images during the downstroke and upstroke are shown at left and right respectively. Large arrows indicate the order of image recording. The illuminated region is 6mm in diameter. See text for more explanation. (color on web and in print)

Fig. 1 is a "blink composite" showing images of the tear film surface during a partial blink. An area of 6 mm in diameter was recorded with a microscopic system based on previous designs (Doane, 1989; King-Smith et al., 2006). A high performance video camera, Basler (Ahrensberg,

Germany) avA1600-gc, was used with a video rate of 67 frames per second at a resolution of 1400 ×1100 pixels. Stroboscopic illumination with a flash duration of 0.04 msec was used to eliminate blur from eye and tear film movements. Images on the left and right correspond to the downstroke and upstroke respectively. L, M and S correspond to large, medium and small areas while B and A correspond to before and after the blink; thus LB corresponds to a large area imaged just before any lid movement in the downstroke. LA was recorded at a long time after the blink, just before the next blink.

Colors are generated by optical interference in the lipid layer (Fogt et al., 1998). The contrast of the images has been enhanced by a factor of 2, and an approximate scale of lipid thickness in nm is given in the key on the right. Lipid thickness less than about 100 nm generates little color, but thicker lipid generates stronger colors. It should be noted that, in addition to recording lipid thickness, the optical system is also sensitive to any distortions of the tear film surface. The meniscus is generally not visible in these images because light is reflected at angles that do not pass into the camera.

The following aspects may be noted. First, during the downstroke, there are distortions or "ripples" on the tear film surface – yellow asterisks in Panels MB and SB. The reason for using the term "ripples" will be described later. These Panels can be compared to Panel LB where the surface is smoother and the image shows the lipid layer without obvious surface distortions. Second, some thicker (more colored) lipid is seen to accumulate under the lid in the downstroke. This indicates a downwards movement of the lipid layer in the downstroke, particularly just under the lid. This lipid movement is much slower than the downward movement of the lid; this implies that lipid accumulates just under the lid, particularly in the meniscus and perhaps on the lid margin which are not visible in the image. Third, at the position of lowest descent of the lid, the "turning point", a groove is formed in the tear film surface which is indicated between small yellow arrows in Panels SA and MA (Deng et al., 2013; Heryudono et al., 2007). Fourth, the thick lipid which has accumulated under the lid is released at the beginning of the upstroke – shown by the strong colors in Panel SA. Fifth, the final image, LA, is very similar to the initial image LB (Bron et al., 2004).

1.2 Four parts of the blink

The following caricature of the blink cycle seems useful for this review. The blink cycle is considered to be in four parts, which are illustrated in Fig. 2. The downstroke is the motion of the superior lid in the inferior direction to where it stops; where it stops is the turning point. The turning point appears to have some separate phenomena from both the preceding downstroke and the succeeding upstroke. For this review, we take the upstroke to be the superior lid motion in the superior direction plus the events directly tied to this motion that occur in the first roughly two seconds following the lid motion. The interblink is the subsequent time until the next downstroke begins. The collection of all of these events is a blink cycle.

We note that the separation of the different parts of the blink cycle is not always clean or easy. For example, for some subjects with MGD, TBU may actually occur just as the superior lid motion is ending, even though we tend to place TBU firmly in the interblink in this review and in our thinking of the blink cycle in general. Some events that are often thought of as occurring early in

the interblink, we placed in the upstroke; optical quality measurements often span those events and well into the interblink, and we view that as a method that straddles the two parts of the blink cycle.

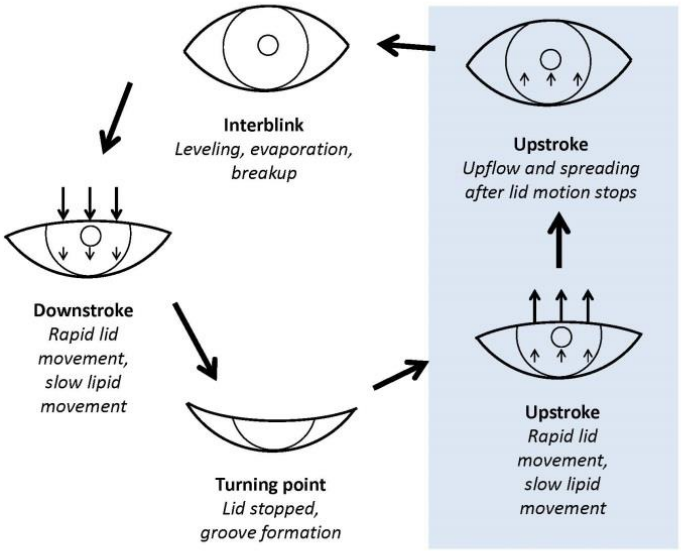

Fig. 2. A sketch of a blink illustrating the four phases we discuss for the blink. Downstroke and turning point are determined solely by the upper lid motion. The upstroke includes the lid motion and the period of strong upflow just after the lid stops. The interblink begins thereafter and lasts until the downstroke begins. (color on web only)

In this cycle, the tear film is both disturbed and replenished. In the downstroke and upstroke, the tear film is forced to move particularly quickly. This leads to visible ripples on the tear film surface that are waves that appear to mimic aspects of the ocular surface. We distinguish them from other waves that may be on the tear film surface because these ripples tend to have wavelengths below 0.2 mm (or 200 μm). Other disturbances to the tear film may have much different wavelength. For example, the meibomian orifices are approximately 1 mm apart around the lid margins, and the may induce waves on the tear film surface due to uneven supply and spreading of the lipid layer and its polar lipids with about this wavelength (Bron et al., 2004; Goto and Tseng, 2003). Another possible wavelength is the about 1 cm, which is the size of the palpebral fissure, and it may arise if gravity is allowed to act for a long enough time on a thick tear film (Braun and Fitt, 2003; Maki et al., 2008). We refer to disturbances with longer wavelengths such as these simply as waves.

2 Downstroke

In the downstroke, we see the formation of what appears to be ripples at the surface of the tear film. These ripples are waves on the surface of the tear film, and they may be described in different ways. After discussing a sample of our observations, we proceed to mathematical models to help interpret the experiments.

2.1 Experimental observations

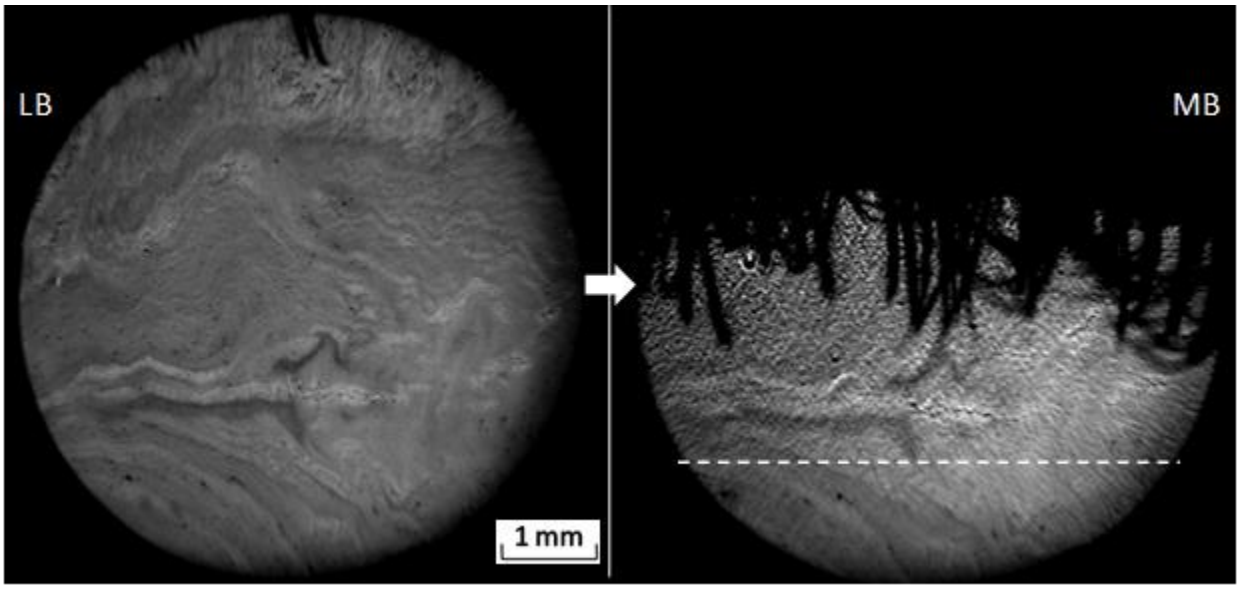

Fig. 3. An example of ripples during the downstroke; labels as in Fig. 1. Left eye of a normal white male, 32 years old. LB (labels as in Fig. 1) shows the lipid layer before the downstroke without evident ripples. MB shows also ripples during the downstroke which are evident above the dashed line.

Panels MB and SB of Fig. 1 showed ripples in the tear film during the downstroke of a blink. The visibility of ripples during the downstroke varies from subject to subject – they are sometimes hard to observe, particularly when there is a strong lipid pattern. A clear example of ripples is given in Fig. 3. Panel LB shows the lipid layer before the downstroke without evident ripples. Panel MB shows the same lipid pattern but also shows ripples during the downstroke which are evident above the dashed line. As in many examples, ripples are strongest near the upper lid.

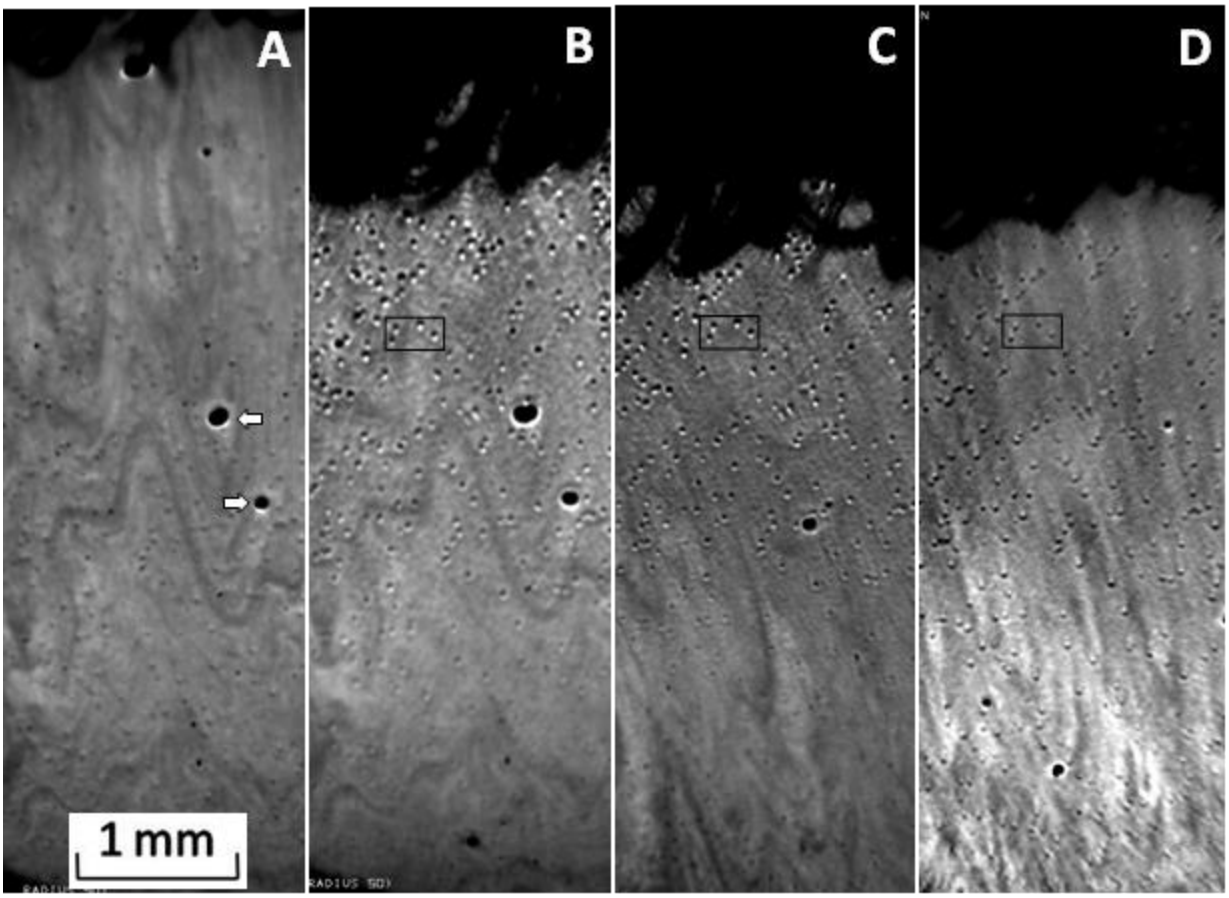

Fig. 4. Ripples recorded for one subject during downstrokes and upstrokes. Right eye of normal white female, 58 years old. A. Before a downstoke. Arrows mark probable bubbles in the tear film. B. During a downstoke. A pattern of four "dots" is shown in the rectangle which were hard to observe before the downstroke in Panel A. C. Downstroke in a second recording about one minute later. The same pattern of four dots is observed in the rectangle. D. Upstroke of the blink after the downstroke in Panel C. The same pattern of four dots is seen in the rectangle. Contrast was increased by a factor of 2 in Panels A to C and by a factor of 4 in Panel D.

Fig. 4 shows the repeatability of ripples from blink to blink and from downstroke to upstroke. Panel A was recorded before the downward movement of the first blink and records the lipid layer with only minor ripples. Panel B was recorded near the start of a downstroke and shows ripples which are strongest near the lid, as in Fig. 1. The rectangle encloses a ripple pattern of four "dots." Panel C was recorded during the downstroke of a blink from a second recording made about one minute after Panel B. The same ripple pattern is seen within and surrounding the rectangle. It should be noted that despite the reproducibility of the ripples, the lipid pattern in Panel C is quite different from that in Panels A and B. Panel D shows the ripple pattern during the upstroke of the same blink as Panel C. The same pattern of ripples is seen despite the fact that the lipid layer is again quite different from that in Panels B and C. The stability of the ripples from blink to blink and between downstroke and upstroke can be explained if the ripples are related to the structure (e.g., roughness) of the corneal surface rather than an independent structure in the tear film such as the lipid layer.

From Fig. 4, it should be noted that the light and dark sides of each ripple have switched in Panel D compared to Panels B and C. This is consistent with the shift or offset of the peaks of the tear film surface switching sign compared to the peaks of the ocular surface because the flow has switched direction. This point will be taken up again in the next section.

There are three aspects of the ripples that are captured by the theories of this section. (1) The ripples only appear while the tear film is moving, most visibly during the downstroke or the upstroke. (2) The wavelength of the ripples appears to be close the spacing of several squamous cells in the corneal epithelium, thus they seem to take on filtered, low-frequency version of the actual corneal surface. (3) The ripples appear to remain in essentially the same location, that is, they are approximately stationary with respect to the corneal surface and roughly independent of the tear film and lid motion.

2.2 Linearized theory of ripples

The fluid motion in the tear film may be analyzed a number of ways, but we give two approaches here. First, we study a linearized theory of the surface ripples. We assume that the flow in the tear film is slow and that the amplitude of the waves on the surface of the tear is small compared to the wavelength. The equations and analysis for this theory are in Appendix 7.3. A conceptual sketch is shown in Fig. 5.

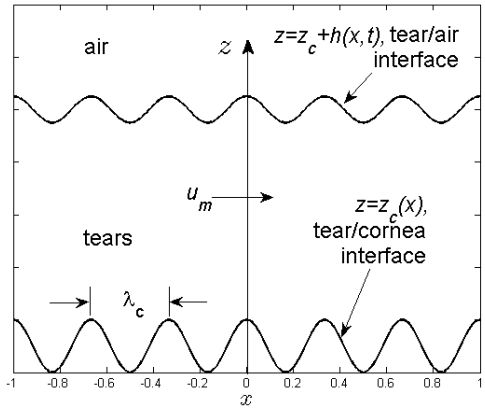

Fig. 5. A sketch of the tear film with thickness h. Tears are in the interval $z_c < z < z_c + h$. Air is above this surface; the cornea is in $z < z_c$.

The theories discussed here assume that the corneal surface is sinusoidal with wavelength λ_c and wavenumber $k_c = 2\pi/\lambda_c$. The corneal surface is specified by $z = z_c(x)$; the corneal surface height thus depends on location but not time, and we express it as $z_c(x) = Z_c e^{ik_c x}$. The thickness of the tear film is given by $z - z_c = h(x,t)$; thus the location of the tear film surface is given by $z = z_c + h$. The tear film surface waves are assumed to be sinusoidal with the same wavenumber as the corneal surface, with $h(x,t) = d' + He^{ik_c x}H$ is the complex-valued amplitude. The average speed of the tear film is specified to be u_m which is assumed to be constant. In this case, the equations simplify to a linearized problem which may be solved up to an arbitrary constant; the resulting equation for the location of the tear film surface is

$$\frac{|H + Z_c|}{|Z_c|} = \frac{\alpha}{\sqrt{1+\alpha^2}}, \qquad (1)$$

where

$$\alpha = \frac{6\mu u_m}{\sigma H^3 k_c^3} = \left(\frac{\lambda_c}{\lambda_{co}}\right)^3, \qquad (2)$$

σ is the surface tension of the tear/air interface and μ is the viscosity of tears. Here

$$\lambda_{co} = 2\pi H \left(\frac{\sigma}{6\mu u_m}\right)^{1/3} \qquad (3)$$

is the cutoff wavelength above which the relative amplitude is effectively one and below which the ripples are effectively attenuated. In Fig. 6, we plot the relative amplitude of the ripples on the tear film surface as a function of the parameters α and λ_c/λ_{co}. As α increases, the relative amplitude becomes one, which indicates that the size of the ripples is the same as that of the corneal surface. As $\alpha \to 0$, the amplitude approaches zero; in particular, this happens as the surface speed of the film decreases to zero, or as H or k become large (a thick tear film or short wavelengths). In Fig. 6B, we see that relative amplitude changes quickly around the cutoff wavenumber, effectively allowing only wavelengths near to or larger than this wavelength.

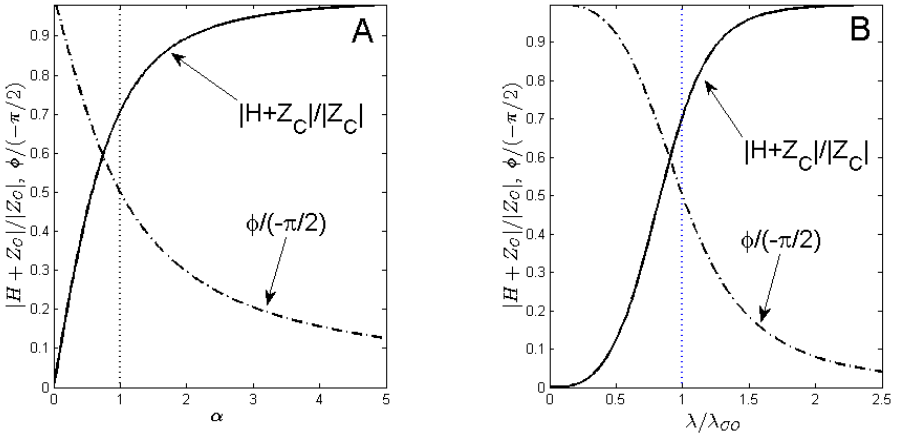

Fig. 6. A. Relative amplitude of the ripple compared to the corneal surface roughness as a function of the parameter α. B. Relative amplitude of the ripple as a function of wavelength normalized to the cutoff wavelength. This figure shows how short wavelength ripples are filtered by the tear film surface.

The crests of the ripples on the tear film surface don't align with the crests of the model epithelial surface; the difference in location can be expressed as a phase shift, or offset, given by $\phi = \arctan(-1/\alpha)$. The phase shift (or offset), normalized with $-\pi/2$, is plotted in Fig. 6 as the dash-dot curve. For small α, ϕ is approximately $-\pi/2$; for large α, ϕ approaches zero and the crests tend to align.

From this analysis, we can see that the wavelength of the tear film surface ripples is the same as that of the model corneal surface since the same wavenumber appears in both expressions for the tear film and the corneal surfaces. This agrees with requirement (1) above. Also, we see that the tear film surface ripple amplitude is approximately proportional to the speed of the surface; this means that the fluid must be moving to make the ripples on the tear film surface. This agrees with requirement (2) above. Finally we see that the tear film surface is sinusoidal but stationary

in x; it is not moving, even though both the surface of the film and the fluid inside are moving. This agrees with requirement (3) above. Furthermore, bigger wrinkles on the corneal surface cause bigger ripples on the tear film surface.

2.3 Nonlinear thin film theory

To complement the linearized theory, we also studied a second, nonlinear theory with moving ends. The problem that we solved is given in detail in Appendix 7.3. The fluid dynamics literature often calls this approach "thin film flow over topography" (Gaskell et al., 2006; Kalliadasis and Homsy, 2001), and the flow in those cases is often driven by an applied pressure gradient or gravity. The model we present here is illustrative and may be slightly different than previous works due to the lid-driven motion of the tear film.

In this case, the thickness of the tear film is assumed to be small compared to the length along the tear film; these are roughly 3 μm and 1 cm, respectively, so this requirement is easily satisfied. The fluid dynamic problem is simplified to a nonlinear partial differential equation for the tear film thickness on a domain with moving ends that simulate the blink. The tear film surface is assumed to have a very strong surfactant (polar lipids) that causes the surface to stretch like a rubber band; this is the so-called "uniform stretching limit" (Braun and King-Smith, 2007; Jones et al., 2005). The consequences of this assumption are discussed further below. We again assume a model sinusoidal corneal surface, and we further assumed sinusoidal motion with time for the ends. The problem is symmetric about the middle of the film; one could say that this model film has two upper lids. These last two items are simplifications, but the problem has all the ingredients that we need.

Results for the nonlinear model problem are shown in Fig. 7. In this picture we see a sequence of plots at different times for fixed thickness under the lids (3.5 μm, which normalizes to 1) and at the moving end of the domain (80.5 μm at the lids). The simulation starts at the closed state ($X(0) = 0.3$) with zero speed and a flat tear film surface outside of the meniscus. In the first five plots of the figure, an upstroke is being simulated; the rectangle that is changing size in the plots represents the moving lid. There is clearly a wrinkled tear film surface, and for the more rapidly moving parts of the upstroke, the wrinkles are larger. The wrinkles are clearly larger when the film is thinner as well. When the fully open state is reached at $t = \pi$ (3.1 in label), the wrinkles are rapidly dying out except at the very thinnest location where they decay more slowly. The wrinkles return in subsequent plots representing the downstroke, only to die out rapidly when the domain becomes fully closed (according to the model). We note that the wrinkles are again approximately stationary with respect to the lid motion; that is, the maxima and minima remained roughly aligned with those of the model corneal surface, even though the surface speed increases from zero at $x = 0$ to the moving end speed at the lid. This nonlinear time dependent result agrees with all of the features obtained for the linearized theory.

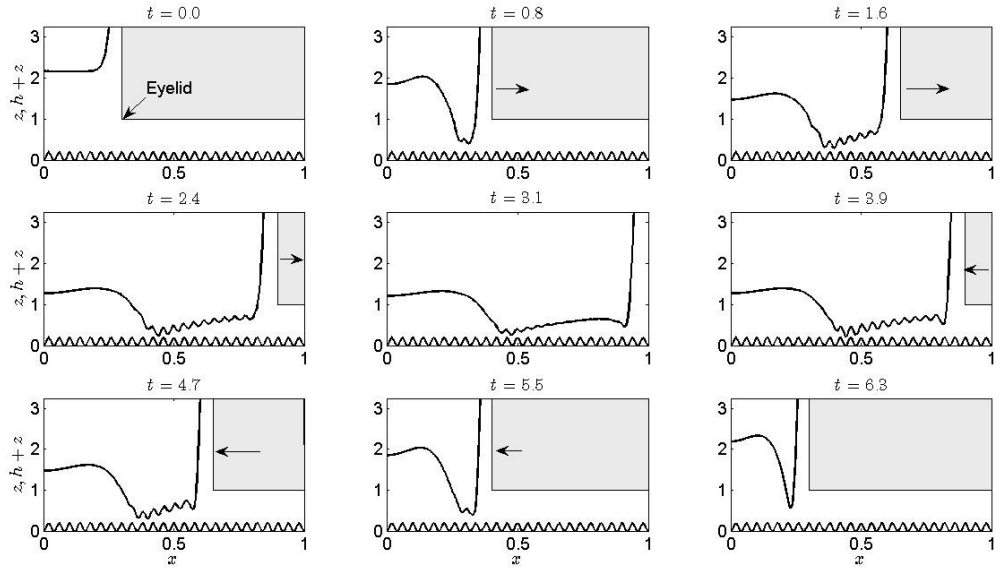

Fig. 7. Time sequence for model blinking problem with a model corneal surface. In this case, the lid, located at $x = X(t)$, started at $X(0) = 0.3$ and then was fully open at $t = \pi$ (i.e., $X(\pi) = 1$); the lid then started to close and that is the state shown in the figure. (color on web only)

A zoom on the middle of the domain from Fig. 7 during the upstroke ($t = 1.6$) and downstroke ($t = 4.7$) is shown in Fig. 8. The tear film thickness is shown as the two upper curves, and the maxima in two locations are shown (dotted for upstroke, dashed for downstroke). The figure shows that the maxima are on different sides of the corresponding maxima of the corneal surface, and that the shift is greater on the downstroke than the upstroke. This may be expected by the linear theory because the shift predicted there is proportional to the speed of motion, and the downstroke is roughly twice as fast as the the upstroke (Doane, 1980). Thus the nonlinear and linear theories agree on the direction and size of the shift due to the direction of lid motion. This result also supports our interpretation of the shifts of light and dark in Fig. 4 due to the different lid motion directions.

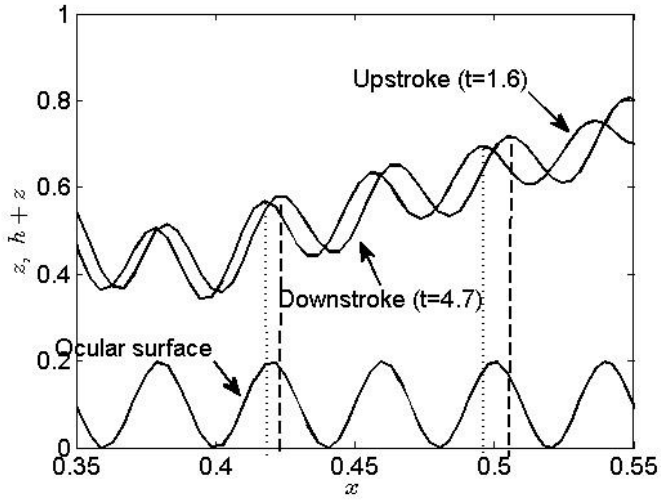

Fig. 8. Zoom of the tear film thickness (upper curves) during the upstroke and downstroke in the middle of the domain from Fig. 7. The local maxima in the tear film shift to different sides of the local maxima in the corneal surface with different lid motion direction as predicted by the linear theory and as observed in Fig. 4.

In Fig. 9, results after the start of the downstroke at $t = 13\pi/12$ are shown for three different conditions of the

model corneal surface. In this case, the lid started at $x = 0.3$ and then was fully open at $t = \pi$; the lid then started to close and that is the state shown in the figure. The wavelength of the model corneal surface is varied; there are zero, 10 and 25 bumps in the interval from $0 \le x \le 1$. It is readily seen that the number of bumps on the tear film surface is the same as that on the model corneal surface. The results shown are normalized for a tear film thickness of 3.5 microns, peak-to-valley size of 0.7 microns, a pre-existing layer under the lids of $h_e = 0.25$ or 0.875 microns, a small meniscus size of 80.5microns. The remaining parameters are given in an appendix.

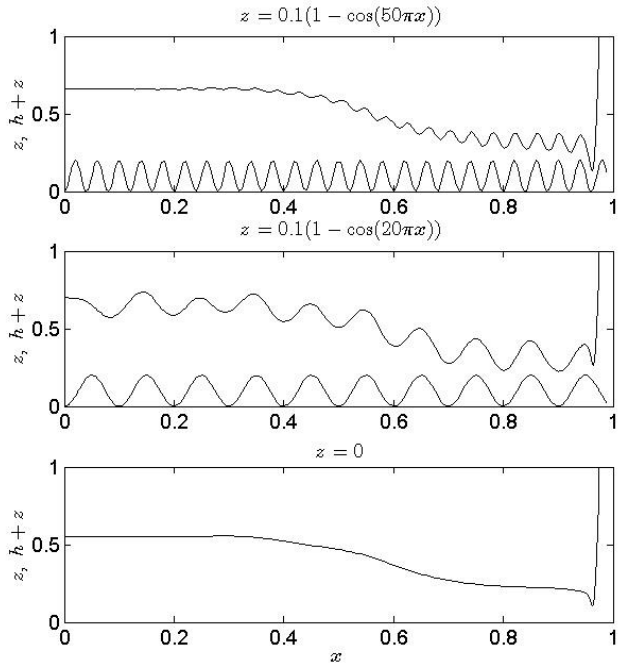

Fig. 9. The wavelength of the model corneal surface roughness is varied; there is zero, 10 or 25 peaks in the interval from$0 \le x \le 1$. The equation for the model corneal surface is given at the top of each panel. Only the range of the normalized thickness from 0 to 1 is shown for clarity. Based on the mean size of squamous epithelial cells of 36 μm (ref), the number of peaks could be as high as about 140. However, the peak to trough amplitude has been estimated to be 0.5 μm (ref), so the amplitude used here would on this order.

In the nonlinear theory of this section, the size of the meniscus may be varied for the same parameters as in the previous figure. We varied the tear meniscus height to 14, 28 or 80.5 μm, and the results away from the meniscus still retained the features discussed above.

2.4 Comparison between the theories

We can use Fig. 7 to quantitatively compare the results from the linear and nonlinear models. At t=1.6, the lid is moving at its maximum (normalized) speed of 0.35. Ripples on the tear film surface can be clearly seen in $0.35 \le x \le 0.55$, with a wavelength matching that of the corneal surface. We use the center point of that interval $x = 0.45$ to draw our conclusions. The wave number of the corneal surface is $k_c = 50\pi$; the magnitude of the oscillations in the corneal surface is $|Z_c| = 0.1$. The surface tension number is $S = 3.07 \times 10^{-6}$, specified in the appendix, shows that surface tension is smaller than the viscous forces inside the film.

Near $x = 0.45$, the thickness of the aqueous layer varies, but is approximately an average of $d \approx 0.4$. By comparing the nearby peaks and troughs of the air/tear film interface, we find that the ripples have $|H + Z_c| \approx 0.0875$, yielding $|H + Z_c|/|Z_c| = 0.875$. The velocity across the domain varies linearly as a result of our uniform stretching limit, so we can identify that $u_m = 0.24$ at x=0.45. The linear theory yields $|H + Z_c|/|Z_c| = 0.89$, with $\alpha = 1.97$ (see Section 2.2).

The results from these two theories agree well with the *in vivo* observations of the tear film during the blink. They capture the three important features listed earlier, and on the strength of that agreement, we conclude that ripples are due to the corneal roughness together with the motion of the lids and tear fluid. We note that real corneal surfaces are more complex, and that the theories can be extended to more complex cases. It is also true that the speed of the tear film is generally more complicated than the linear variation in x at the tear film surface that is found in this model, both for mathematical results (Aydemir et al., 2011; Bruna and Breward, 2014; Jones et al., 2006) and for experimental results (Berger and Corrsin, 1974; King-Smith et al., 2009; Owens and Phillips, 2001). However, the limiting case did allow a particularly easy estimate that is effective.

3 Turning point

At the turning point, the downward motion of the superior lid stops and then reverses direction to start the upstroke. This phase of the blink cycle is different from the downstroke and the upstroke in that the lid motion stops and the painting of the tear film onto the ocular surface is least effective there, leaving a thin aqueous region, or groove. The lipid layer is also affected by the location of the turning point, since it can leave behind a significant amount of lipid there at the beginning of the upstroke.

Many blinks are partial (Cruz et al., 2011; Doane, 1980; Harrison et al., 2008; Himebaugh et al., 2009; Wu et al., 2014) and this makes the effects of the turning point more visible than the full blinks in the optical systems we have used. Fig. 1 may be considered a partial blink because Panels SA and MA show evidence of the turning point. The short arrows in these panels indicate the turning point after the lid has begun the upstroke. The aqueous layer at the indicated line is thinner and discussed below. The lipid layer is colorful just above the indicated line, implying a thick lipid layer there and that this thick lipid layer could not keep up with the lid during the upstroke. The upstroke is discussed in the next section.

Results for a half blink are shown in Fig. 10. In the experimental image, simultaneous narrow and broad band interferometry was used to image the pre-lens tear film thickness (Braun and King-Smith, 2007). The capture of the half blink was fortuitous, but the simultaneous methods allowed the quantitative estimate of the tear film thickness. A groove or partial blink line is left behind near the turning point; this phenomenon has been qualitatively described in a number of previous papers (Harrison et al., 2008; Himebaugh et al., 2009; Jones et al., 2005). The quantitative estimate along the vertically-oriented line segment in the experimental images is shown as the grey dots in the right side of Fig. 10 with computed results from a mathematical model (Deng et al., 2013); the details of the model may be found in the original paper. The results of previous models (Braun and King-Smith, 2007; Heryudono et al., 2007) were improved in this more recent work by allowing the thickness of the tear film under the lids to vary during the computed sequence of blinks. In particular, the TF thickness on either side of the groove corresponds well with the observations, with the superior side smaller than the inferior side. This improvement was obtained by reducing the thickness under the lid for partial blinks. Leaving the TF thickness under the lids the same for the partial blinks results in the opposite occurring, with a thicker tear

film superior to the groove. This result suggests that the thickness under the lid is not constant for different types of blinks.

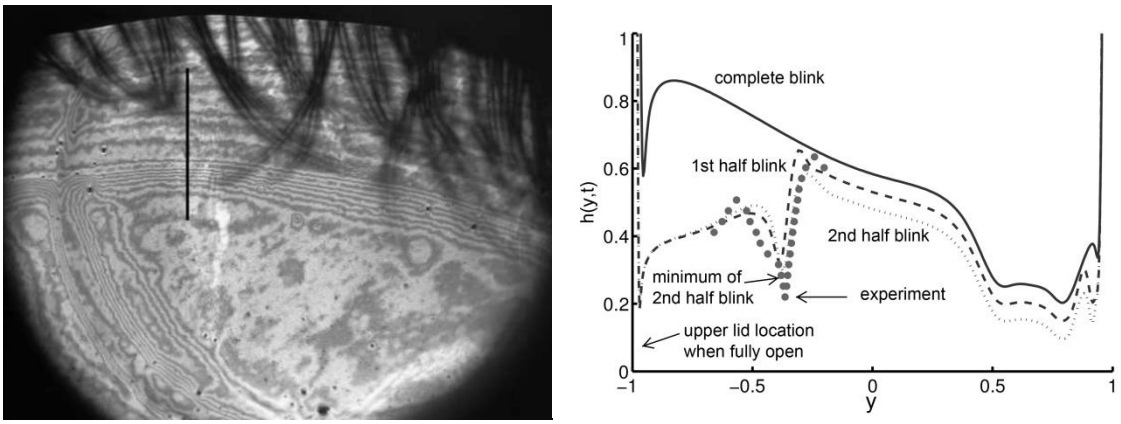

Fig. 10. Left: Interference fringes for a pre-lens tear film using narrow band interferometry (Braun and King-Smith, 2007; Nichols and King-Smith, 2003). A separate simultaneous imaging system allowed estimation of the absolute thickness. Right: Results from the theory of Deng et al. (2013) for a full blink followed by two half blinks. The gray circles are the experimentally determined thickness. For further explanation, see text.

4 Upstroke

After the turning point, the upstroke proceeds at roughly half the speed of the downstroke (Doane, 1981). During the upstroke, the tear film is effectively painted onto the ocular surface. The aqueous layer is partly from the meniscus and partly from the existing layer under the lids (Jones et al., 2005; King-Smith et al., 2004; Wong et al., 1996). When the superior lid motion stops, the surfactant action of the polar lipids and possibly other surface active components of the tear film cause the tear film to continues to move superiorly, often against gravity (Berger and Corrsin, 1974; King-Smith et al., 2009; Owens and Phillips, 2001). Because it is often against gravity, we call this phenomenon "upward drift." This superior motion typically lasts one or two seconds beyond the superior lid motion ends, and is clearly a result of the lid motion. For this reason, we include this part of the blink cycle in the upstroke. We first discuss the tear film dynamics while the lid is moving, and then move on to events such as upward drift that are closely associated with the superior lid motion.

4.1 The lid motion and the tear film

Fig. 4 shows that corresponding ripples can be observed during both the downstroke and upstroke of a blink, but they are generally weaker during the upstroke. Ripples in the upstroke are often difficult to observe in still images, but can be easier to see in video recordings where the lipid layer appears to move upwards over a weak, stationary pattern of ripples This relative weakness during the upstroke may be related to the lower superficial velocity of the tear film – see Eqs. (1), (2) and Fig. 6. The lower tear film velocity in the upstroke may be related to the lower lid velocity in the upstroke (Doane, 1980). The relative weakness of ripples in the upstroke may also be related to increased tear thickness – see Eqs. (1) and (2) – as tears lost by evaporation are

replenished by the blink. Ripples in the upstroke may also be difficult to observe because they are often masked by a relatively thick, colored lipid layer, e.g., Fig. 1 Panel SA.

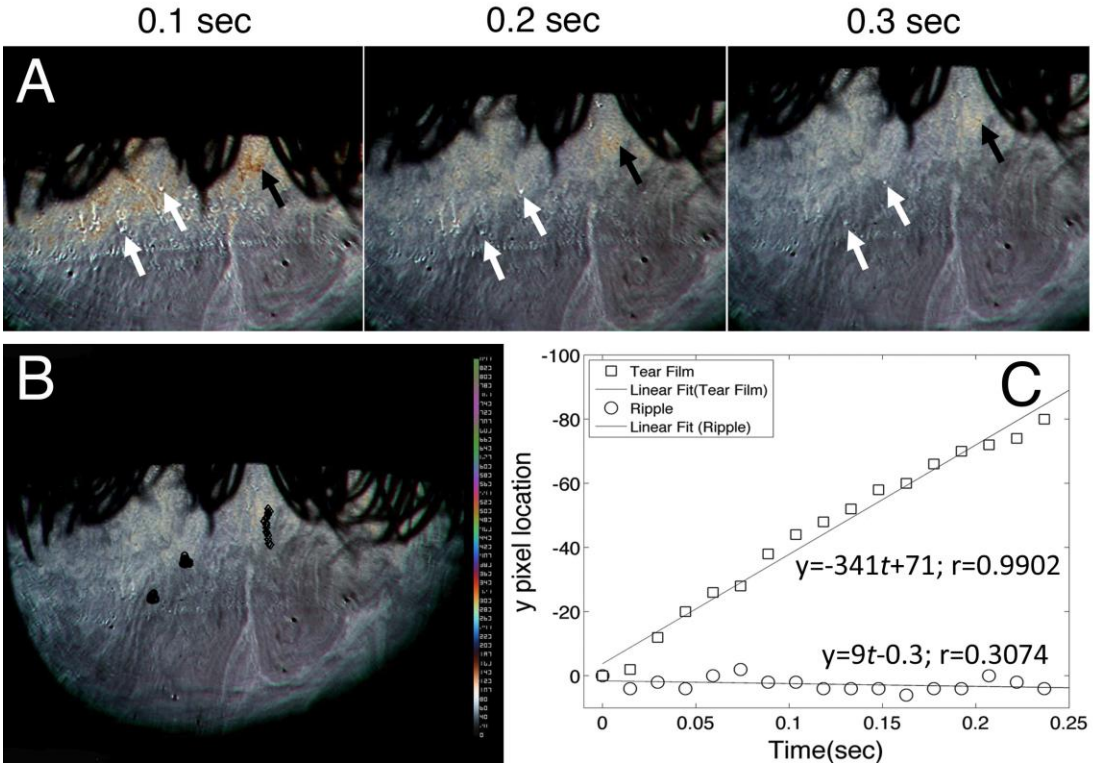

Fig. 11. Analysis of lipid and ripple positions in an upstroke; DE disorder, 48 year old white female. A. Several images of the lipid layer during the upstroke. The points that are tracked in the images (not all are shown) are indicated with arrows. B. The position of the three features was traced and processed over a sequence of frames; the last image is shown. The two points at left are ripples; the point at right is in the lipid layer (labeled "tear film"). C. The difference in vertical locations (*y* values) of the features with time relative to the lowest point, and a linear least squares fit. The locations are in units of pixels. (color on web only)

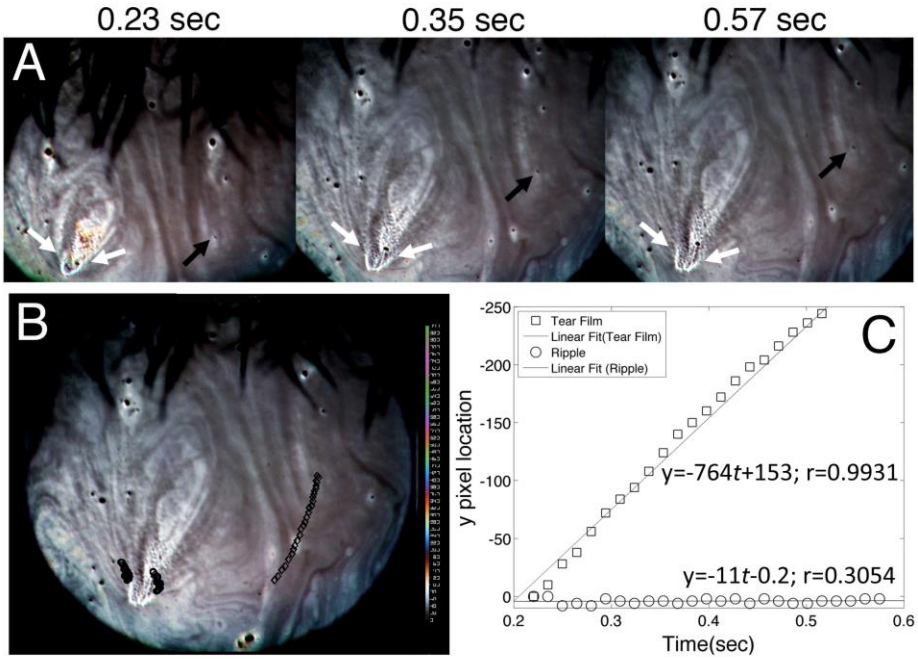

Fig.12. Analysis of lipid and ripple positions in an upstroke; normal white female, 22 years old. A. Several images of the lipid layer during the upstroke. The points that are tracked in the images (not all times are shown) are indicated with arrows. B. The position of the three features was traced and processed over a sequence of frames; the last image is shown in the background. The two points at left correspond to ripples; the point at right is in the lipid layer. C. The difference in vertical locations of the features with time relative to the lowest point, and a linear least squares fit, both in pixel coordinates. (color on web only)

In Figs. 11 and 12, ripples and lipid features are tracked. The positions of two points that are stationary with respect to the ocular surface (white arrows) were recorded. The difference between the lowest location and the other two locations was plotted in panel C in both figures to approximately eliminate eye movement. The ripples appeared to be stationary apart from eye movement because the difference between their locations is approximately zero, as is indicated by the lower curve in each Panel C. In contrast, the motion of the lipid layer much larger in both figures, as indicated by the upper line in each Panel C. In Fig. 12, a movement toward the nasal side can also be seen besides the upward drift. This is observed in a significant number of subjects, but the typical prevalence of such motion is not yet known. These images lend further support to the notion that the ripples appear due to flow in the tear film over the rough epithelial surface.

4.2 Upward drift

During superior lid motion and for up to about two seconds after, the tear film and lipid layer move superiorly (King-Smith et al., 2009; Owens and Phillips, 2001) . The motion is not uniform across the ocular surface. In observations of the lipid layer, it is not uncommon to see more lipid left behind in central regions of the cornea during the upstroke which subsequently spreads. The

dynamics and mechanisms of this lipid motion are an area of considerable interest (King-Smith et al., 2013a; Rosenfeld et al., 2013).

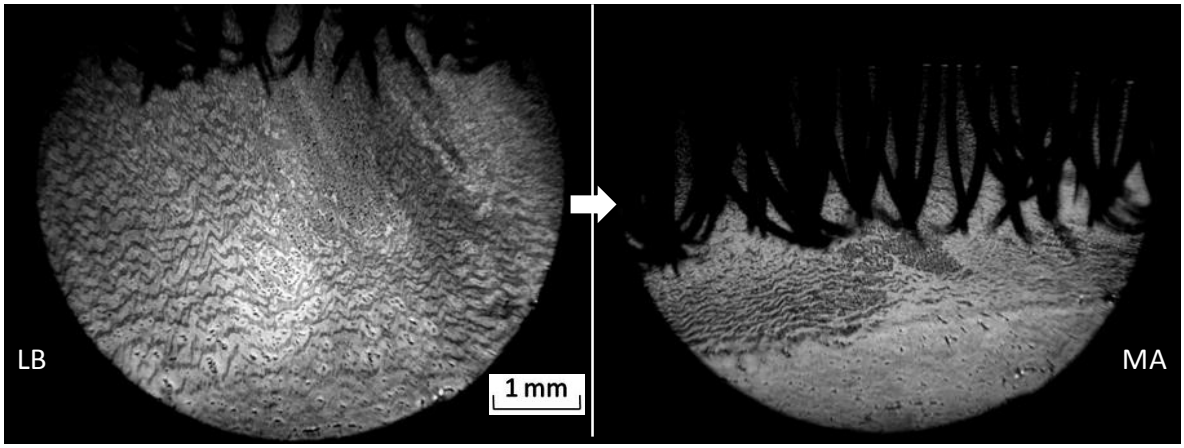

Fig. 13. Blink composite showing near horizontal stripes. Color images have been converted to grayscale – some color was seen above the turning point in Panel MA. Right eye of a 27 year old, normal white male.

McDonald (1969) reported that, during the downstroke in rabbits, "the visible oil layer was pushed ahead, becoming thicker and more bunched up, as a pleated drape gathers itself together." Conversely, in the upstroke, he reported that the lipid layer could be reformed by unfolding of this bunched up structure. Bron et al. (2004) noted that this folding/unfolding mechanism could help to explain why the lipid layer pattern is often little changed by a blink cycle. This pleated sheet could be generally hidden near the lid and the upper meniscus. However, it seems possible that when stretched out in the upstroke, the remains of the pleated sheet might be visible as a pattern of near horizontal stripes. Fig. 13 shows an example of such a pattern with relatively broad stripes before the blink, Panel LB, and more compressed stripes during the upstroke in Panel MA. If these stripes correspond to the folds of a pleated sheet, this indicates that the folds are asymmetrical and have a non-uniform lipid thickness – e.g., the outer parts towards the air have thicker lipid than the inner parts towards the aqueous tears. Such an asymmetry in the folds might occur because the viscosity of aqueous tears is much greater than that of air; as the folds form, the greater viscosity of aqueous tears will cause the outward pointing folds containing aqueous tears to be broader than the inward pointing folds containing air.

4.3 Early lipid spreading phenomena

During and just after the superior lid motion, fine localized features in the lipid layer may be observed (King-Smith et al., 2011). In their high resolution stroboscopic microscope study, King-Smith et al. (2011) called such features "snowflakes" and "clouds;" examples can be seen in their Figure 10. In that figure, these features were observed in less than 0.1 s post-blink in DE subjects. It seems possible that rapid stretching of the lipid layer during the upstroke may cause it to fracture, forming these snowflakes and clouds. A model of the lipid layer has been proposed based on lamellae containing dense arrays of saturated hydrocarbon chains (King-Smith et al., 2013a). It is suggested that rapid stretching of the lipid layer may fracture these lamellae, generating the observed snowflakes and clouds. They most likely contribute to the lipid

spreading time course on the order of a few tenths of seconds observed previously (Goto and Tseng, 2003).

4.4 Release of lipid

The new lipid imaging system can capture some aspects of lipid release from the lids. Fig. 14 shows a "blink composite" (as in Fig. 1) for a subject with a very thick lipid layer. There is some thickening of lipid in the downstroke, e.g., between Panels LB and MB, regions having a dark brown or purple color corresponding to about 180 nm are converted to pale blue or cyan of about 240 nm. Early in the upstroke, Panel SA, the lipid layer trailing the moving superior lid is significantly thinner, but a relatively thick region drifts back into the bottom of the images in Panels MA and LA. This is an example of the uneven upward drift mentioned previously. In these latter two panels, additional features are observed that appear to be related to lipid release. It has been proposed that lipid is delivered from the meibomian glands during the blink (Knop et al., 2011). Fig. 14 shows what seem to be "globs" of lipid released during the upstroke, particularly in Panel MA. The globs have come from the upper lid because there has not been time for them in Panel MA to travel from the lower lid. The lipid layer in Panel LA has been displaced downwards compared to LB, presumably because of the extra lipid which has spread out from the globs. This may contribute to the turnover of meibum in the lipid layer which is a little understood process (Khanal and Millar, 2010; Mochizuki et al., 2009). The marked change in lipid layer pattern between Panels LB and LA should be compared to the reproducibility in Fig. 1. The blink in Fig. 14 may be described as a "covering blink" because the lid covered the visible cornea at its lowest point; it may have been a full blink or a more complete partial blink than in Fig. 1.

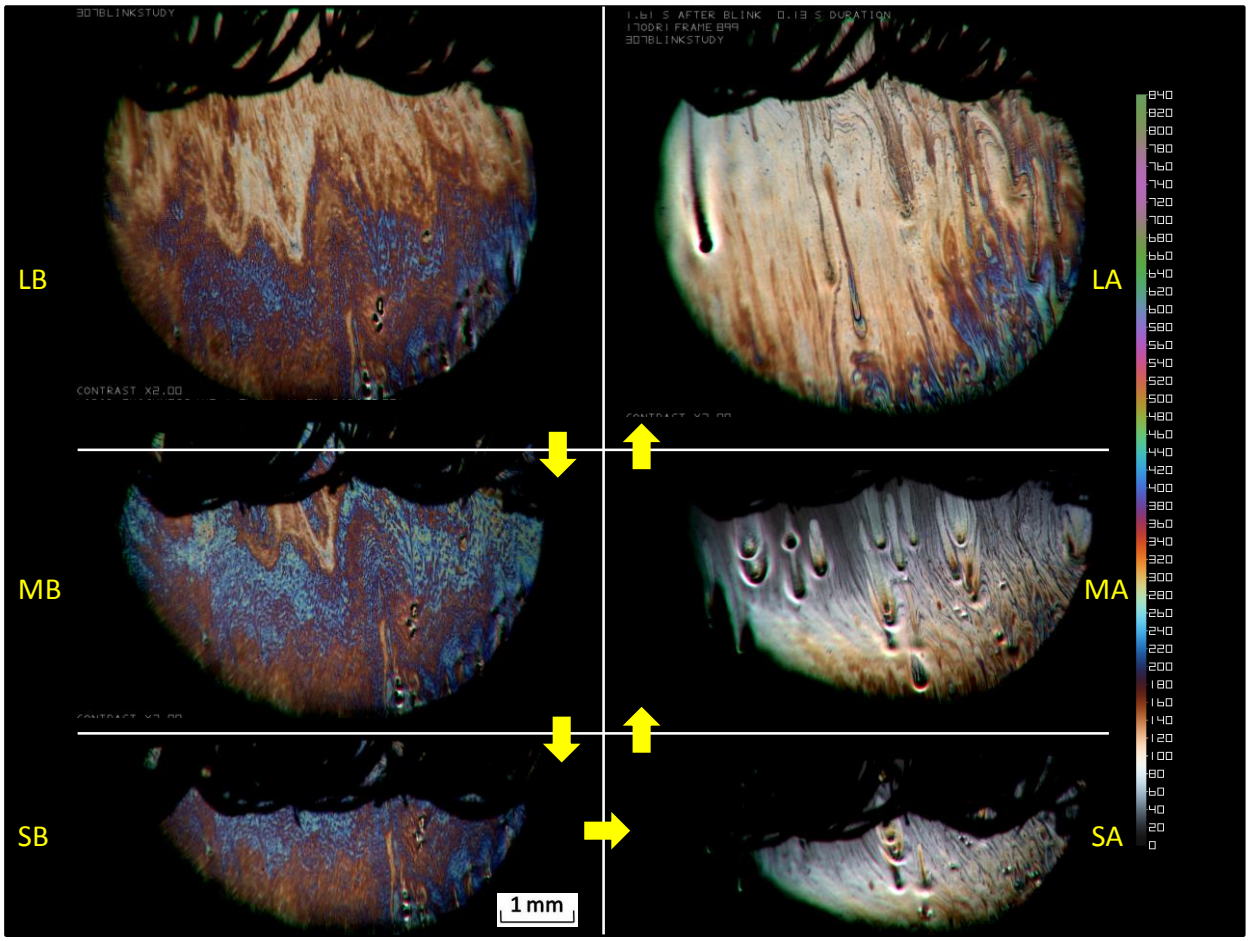

Fig. 14. This blink composite shows release of lipid during the upstroke. See text for more explanation. Labeling as in Fig. 1. (color on web and in print)

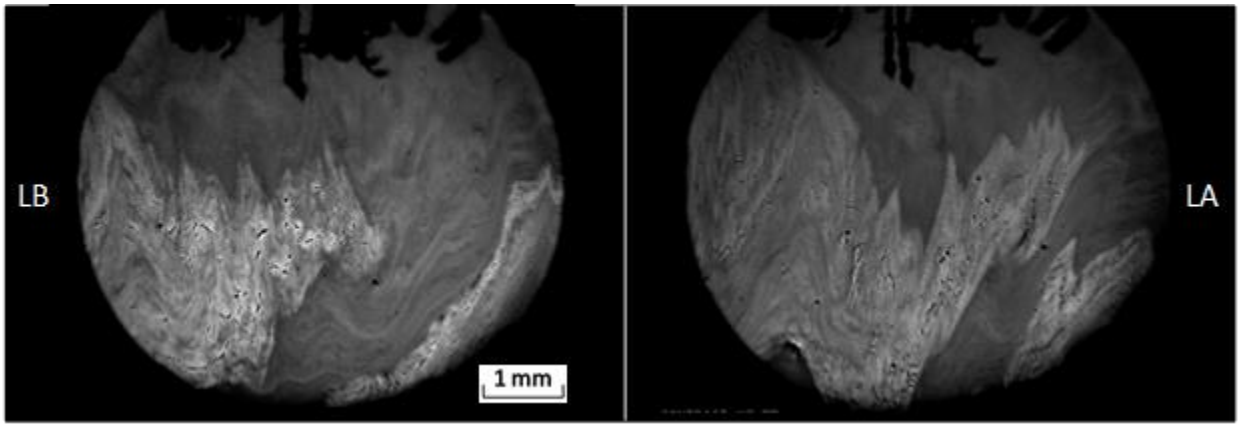

Fig. 15. Blink composite showing displacement of the lipid layer caused by a blink – compare Panel LA with LB (labeling as in Fig. 1). Because there was little color in the original images, these images have been converted to grayscale. Right eye of 24 year old normal white female.

Fig. 14 shows how the lipid layer can be displaced downwards by a blink, probably contributing to the turnover of lipid. Fig. 15 illustrates how the lipid layer can also be displaced laterally by the blink, in this case in a nasal direction. In succeeding blinks, the nasal displacement of the lipid layer continued (not shown). As in the downward displacement of the lipid in Fig. 14, this lateral displacement could contribute to the turnover of the lipid layer of the tear film (Khanal and Millar, 2010; Mochizuki et al., 2009).

5 Interblink

We begin this section by considering flows distant from the menisci and black lines. We then consider flows in the interblink that involve the meniscus and black line in significant ways.

5.1 Experimental results for tear film optical quality improvement

A number of studies in the tear film literature have studied the dynamic changes in optical quality following a blink. Generally, the literature for tear films in this area is experimental using surface imaging or surface interferometry. In this approach, the tear film/air interface reflects light from a controlled source and the resulting image is manipulated to deduce information about the shape of tear film surface. How the reflection from the tear film surface is manipulated determines the method.

Nemeth et al 2002 analyzed the images from the photokeratoscope part of corneal topography instrument; we would call this a surface imaging method. They computed the surface regularity index (SRI) and the surface asymmetry index (SAI) developed by Klyce and co workers (Dingeldein and Klyce, 1989; Wilson and Klyce, 1991). They found that there was typically improvement (smoothing) of the tear film surface followed by decreased quality (roughening) of the tear film. Significant variation was among subjects; the mean time to reach the minimum SRI, which was taken to be the best optical quality, ranged from about 2 to 13 s. Similar approaches were used by Goto et al. (2004) and Kojima et al. (2004) but the sampling rate was 1 Hz; a high speed videokeratoscopy method was developed by Iskander and Collins (2005). The faster frame rate and measures from fitting smooth functions to the SRI and SAI data allowed them to estimate the time course of the optical quality and TBUT.

Kasprzak and coworkers have developed two different types of interferometers: the Twyman-Green (TGI) and lateral shearing interferometers (LSI). To our knowledge, only results for TBU have been published to date with the TGI approach (Licznerski et al 1999). Licznerski et al (1998) developed an LSI for observing tear film changes and breakup. Several improved versions of the LSI have been developed (Dubra et al., 2004; Szczesna et al., 2006; Szczesna and Kasprzak, 2009). These and related methods have recently been reviewed by Montes-Mico et al. (2010).

Of particular interest to us is Szczesna and Kasprzak (2009); they used an LSI to characterize the tear film improvement after a blink and they found different rates of decay to a leveled tear film using different measures. The "*B*" measure had a time constant of 2.5s, while the "*T*" measure had a shorter time constant around 0.5 s for the same subjects. Their optical imaging indicated that perhaps 5 or 6s were required to damp out the variation. We believe that the ripples formed during blinking contribute to the initial times of optical quality improvement. These short-

wavelength distortions on the optical surface will scatter light and exist on the same time scale as the upflow due to the Marangoni effect and its associated film motion (Berger and Corrsin, 1974; King-Smith et al., 2009; Owens and Phillips, 2001). Thus, it seems likely that they will contribute during the roughly 2 s upward drift duration, but they will contribute more at the beginning when the upflow is faster and decay as the upflow does. However, the longer time scales of some measures suggest that one or more other mechanisms for smoothing the tear film are present as well. We discuss surface-tension driven leveling as one such mechanism, which may act on longer waves on the tear film surface for longer times scales which may be appropriate in some cases.

Other methods have come up with other characteristic times as well. Ferrer-Blasco et al. (2010) found that it took 5 to 6 s to reach optimum optical performance using their modulation transfer function approach. Using wavefront aberration, they found that dry eyes had RMS values that reached a minimum in an average time of 2.9 s while for normal the mean time to minimum was 6.1 s (Ferrer-Blasco et al., 2010). Goto and Tseng (2003) found healthy subjects had a mean of 0.3 s for lipid spreading, but lipid deficiency led to mean times for spreading of 3.5 s and aqueous deficient subjects averaged 2.2 s for spreading. These methods may also emphasize different contributions to lipid motion and/or tear film disturbances.

5.2 Leveling

In this section, we assume that the upward drift is effectively finished, and that any fluid motion is driven by capillary pressure due to the average surface tension of the air/tear film interface. Similar flows have been studied in the context of paint and other coatings (Orchard, 1962) and have included additional physicochemical effects such as evaporation and the Marangoni effect (Howison et al., 1997; Schwartz et al., 1996).

5.2.1 Leveling in the absence of evaporation

We now consider the theoretical flattening of the film in the absence of evaporation or osmosis. It is convenient to work with the dimensional form of the lubrication equation in this case. If we further assume that the anterior surface of the aqueous layer is completely clean, then the theoretical consequence is that there are no mechanical shear stresses there. This case is often called the “stress free” case in the fluid mechanics literature; the free surface of the film is free to move along itself without resistance.

It is possible to gain insight into what happens to the tear film in the leveling process by considering only small waves on the surface of the tear film. In this process, we assume that the thickness of the aqueous layer is very close to its average value d, and write an approximate equation for the waves relative to the average. The small size of the wrinkles is contained in the (small) amplitude $h' \ll d'$. Using this information we may write

$$h(x,t) = d' + h'(x,t). \qquad (4)$$

Solutions for h' are given by a product of an exponential decay in time and a sinusoidal wave in space; see Appendix 7.4. The half life of the decay is given by

$$t_{1/2} = \frac{3\mu}{d^3\sigma}\left(\frac{\lambda}{2\pi}\right)^4 \ln 2. \qquad (5)$$

For the tangentially immobile case, the 3 in the numerator is replaced by a 12. Some numerical results are in Fig. 16. It can be seen that the dependence on the wavenumber on either the thickness or the wavelength is very strong: the half-life of the waves changes over orders of magnitude. For a 3 μm film, sinusoidal waves with 1mm wavelength decay to half their amplitude in a little more than one second; this wavelength is about the wavelength of the spacing of the meibomian gland orifices and is about the same time scale as the tear film build-up observed experimentally (Montes-Mico et al., 2010; Szczesna et al., 2007). For a wave of 5mm wavelength, which is on the order of the palpebral fissure, has a half-life of about 900 seconds. This suggests that the surface-tension-driven relaxation of wavelengths at the meibomian gland spacing or shorter may contribute for the observations for up to 2 to 3 seconds, but longer waves are likely to be responsible for the longer time scales observed by some methods (Ferrer-Blasco et al., 2010; Iskander and Collins, 2005; Nemeth et al., 2002).

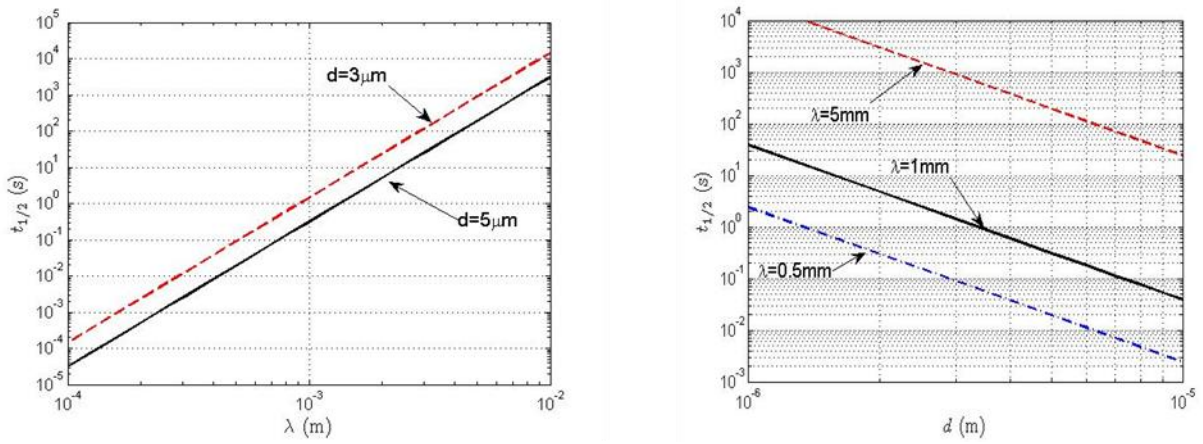

Fig. 16. Left: Half life of waves on the surface of the tear film as a function of wavelength for two different thicknesses. Right: Half life of waves on the tear film surface as a function of thickness for three different wavelengths. (color on web only)

5.2.2 Leveling in the presence of evaporation

When the film is evaporating, the tear film gets thinner at the same time that waves on the tear film surface are flattening out. Because the amount of flow inside the tear film is proportional to h^3 (for models considered here), this slows down the leveling process, and preserves the waves or other surface disturbances longer than the case without evaporation. We solve a simple mathematical model (described in Section 7.4) to illustrate this phenomenon.

The chief advantage of integrating the nonlinear partial differential equation(PDE) directly is that when the film gets thin, it cannot become negative (a negative tear film thickness would be nonsense), and it is still valid even if the disturbances or waves are not small compared to the thickness of the tear film.

In Fig. 17, the initial tear film thickness is a sum of two sinusoidal waves with wavelengths of 5mm and 1mm. These were chosen to be representative of longer waves that may arise from

disturbances due to the size of the palpebral fissure and the meibomian orifice spacing, respectively. The tear film thickness is normalized by its mean value of 3.5 μm in this case; the length scale along the film is normalized by 5mm. The figure shows many instances of the tear film thickness plotted as a curve at different times, in a format called a waterfall plot. The plot shows that in a very short time, the 1mm wavelength component is flattened out, while the 5mm wavelength component is being flattened out only very slowly. The minima and maxima persist for the long wave, and the minimum of this wave reaches the equilibrium thickness where, in this model, evaporation is balanced by the attraction of the tear film for the model ocular surface, and no more water is lost via evaporation. In the model, this corresponds to the first breakup time at about $t = 40$ in the figure. This TBU region then spreads as time goes on, and just before $t = 55$ the tear film is completely broken up, corresponding to complete dry out of the tear film.

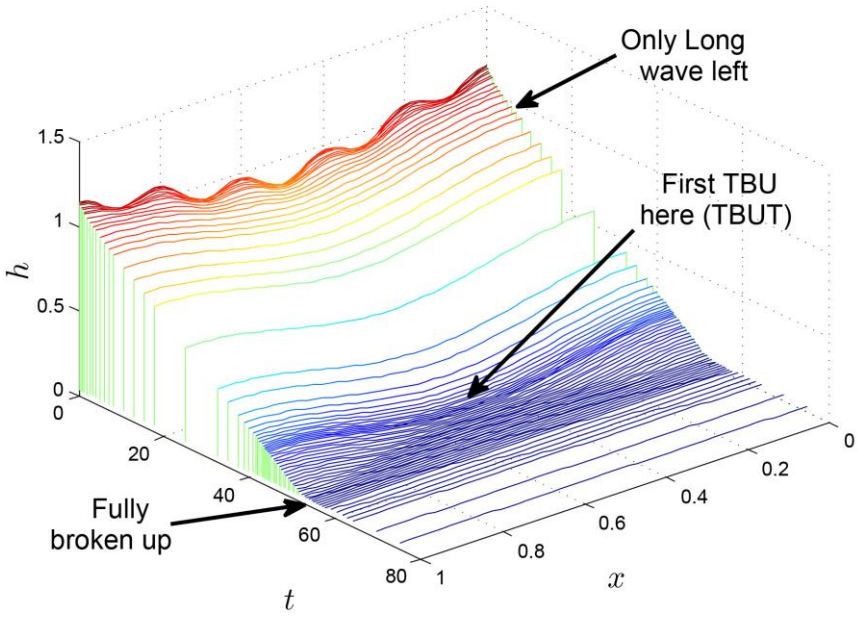

Fig. 17. Results for the tear film thickness for increasing time. The short wavelength component dies out much faster than the long wavelength. (color on web only)

Of course, this example is only illustrative since we wouldn't force subjects to keep their eyes open until complete dry out of the ocular surface. However, the model helps illustrate some of the basic processes at work. The slow decay of longer waves is related to λ_c^4 in the numerator of the equation for the decay rate, Eq. (5); longer waves take dramatically longer to decay. The slower decay of the waves due to evaporation preserves wrinkles in the tear film, which is related to the d'^3 in the denominator of Eq. (5) because decreasing thickness causes dramatically longer half-life.

5.3 Solutes: Osmolarity, Flourescein and Fluorescence

5.3.1 Measurements

Tear film hyperosmolarity is considered a core mechanism of DE and is thought to be a key variable in its development, diagnosis and progression (Baudouin et al., 2013; DEWS, 2007). Tear

film osmolarity is usually clinically evaluated by sampling tears from the inferior tear meniscus, yielding values of 296-302 mOsM in normal patients and range of values from 300-360 mOsM or higher in patients with DE. Clinical cutoffs for the diagnosis of DE vary based on the study and the severity of DE, but most fit within the range of 305-318 mOsM (Gilbard et al., 1978; Lemp et al., 2011; Tomlinson et al., 2006; Versura et al., 2010). DE patients also show increased variability in tear film osmolarity measurements from the lower tear meniscus, compared to controls (Bron et al., 2014; Keech et al., 2013). Recently, a calibrated resistance measurement using the TearLab device allows rapid determination of osmolarity from very small tear samples with an error for *in vitro* samples of about 1-2% (Lemp et al., 2011).

However, the clinical measurement of tear osmolarity from the lower tear meniscus may not fully represent the increased tear film osmolarity over the corneal compartment of the tear film (Bron et al., 2002; Gaffney et al., 2010). Indirect evidence from sensations recorded during TBU and with hyperosmolar drops indicates that tear film osmolarity could reach 800-900 mOsM within areas of TBU or thinning. Recent mathematical modeling also predicts spikes in osmolarity within TBU (Braun, 2012; Braun et al., 2014; Peng et al., 2014; Zubkov et al., 2012). The theories we describe here will supply quantitative estimates for the osmolarity in locations that cannot be measured at the time of writing, in situations like TBU which may have very localized and high values of osmolarity. We begin discussing theory with results in a spatially uniform approximation, then progress to theories over the exposed ocular surface and TBU, both of which have solute concentrations varying with both location and time.

5.3.2 Aspects of osmotic supply from the ocular surface

We present models in the next few sections that incorporate fluid motion as well as transport of solutes representing the osmolarity c and the fluorescein concentration f, osmosis from the ocular surface, evaporation, wetting of the ocular surface, and the fluorescent intensity I that we compute from f.

We assume that the ocular surface is healthy and in this condition is an ideal semipermeable membrane that allows water to pass through it but no solutes. Fluorescein penetrates the normal ocular surface on the time scale of minutes (Webber and Jones, 1986) so that for the time intervals for which we compute solutions, this is a good approximation for this molecule. For ions like sodium and chloride, this is a simplification, but it is a reasonable first step (Levin and Verkman, 2004). For these choices, and after normalizing the osmolarity with the isotonic value (c_0=300 mOsM), the osmotic supply may be written as $P_c(c-1)$. Here P_c is the nondimensional permeability. Here we have neglected any contribution of fluorescein to the osmotic flux in this paper; this is justified in Appendix 7.2.

5.3.3 Theory and experiment for local flat spot dynamics

Video recordings were made from 30 subjects (including normals and dry eyes). The subject's head was positioned on a chin and head rest. After instillation of 1 µl of 5% fluorescein and alignment, video was recorded for a 60 second period. Subjects were instructed to blink about 1 second after the start of the recording and try to hold their eyes open for the remainder of the recording. Exciter and blocking interference filters were used to reduce the response to reflected illumination light. Horizontal illumination width was 15 mm, thus including the cornea and part

of the conjunctiva. Images were stabilized by using a cross-correlation method (King-Smith et al., 2009) to align the regions of conjunctiva (which gives a high contrast image that is stationary relative to the conjunctival surface).

Tear film thickness was studied by using the self-quenching of fluorescein, i.e., the reduction of fluorescent efficiency with increasing fluorescein concentration shown at high concentrations in Fig. 5 of Webber and Jones (1986) and more recently treated in the Appendix of Nichols et al. (2012). In these papers, the critical concentration of fluorescein, beyond which quenching occurs, is about 0.2 % and concentrations above this value are in the concentrated (quenching) regime. When 1 µl of 5 % fluorescein solution is diluted by about 7 µl of tears, fluorescein concentration in the tears is estimated to be about 0.625 %, which is in the concentrated regime for the fluorescent quenching. As the tear film thins from evaporation, the efficiency (and hence fluorescent intensity) is approximately inversely proportional to the square of concentration and so is proportional to the square of tear thickness. Thus tear thickness is proportional to the square root of fluorescent intensity (Nichols et al., 2012).

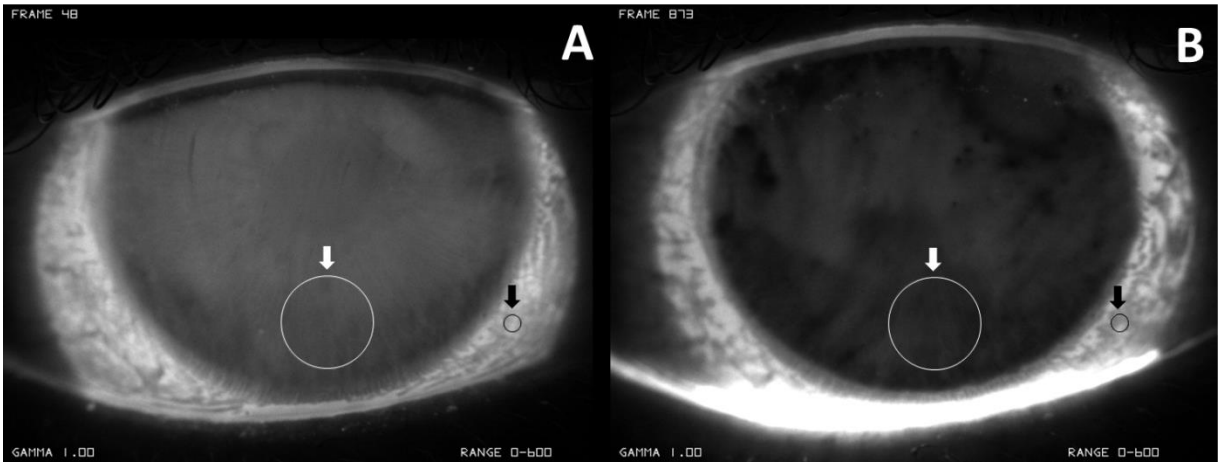

Fig. 18. Fluorescent images at, A, 2 s and, B, 57 s after a blink. Arrows in A indicate circular areas used for averaging intensities over the cornea and conjunctiva for the analysis illustrated in Figs. 19 and 20.

Statistical analysis was performed with Sigmaplot 9.0 (Systat Software, Chicago, IL) for least squares fitting of thinning of the tear film. Results of this analysis are shown for the pre-corneal tear film in Fig. 19 and for the pre-conjunctival tear film in Fig. 20.

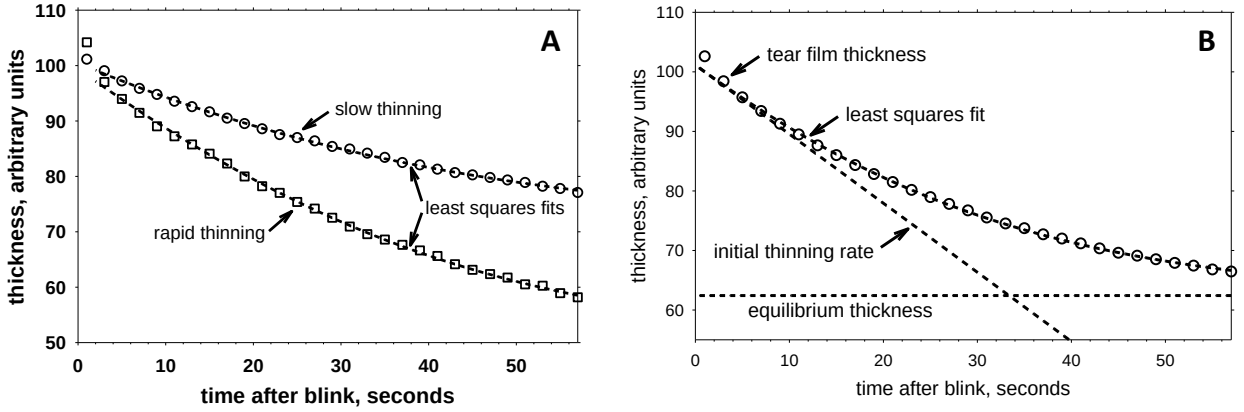

Fig. 19. A. Examples of rapid and slow thinning of the pre-corneal tear film from two subjects (circles and squares). The dashed lines show the fits of a model based on constant evaporation and increasing osmotic flow through the corneal epithelium surface (Eqn. (8) below). B. Average thinning curve (circles) for the pre-corneal tear film from 15 subjects for the rapid case are shown together with a least squares fit of the model (dashed curve). The "initial thinning rate" is thought to be mainly due to evaporation. The "equilibrium thickness" is the final thickness which would have been reached when evaporation is balanced by osmotic flow out of the cornea.

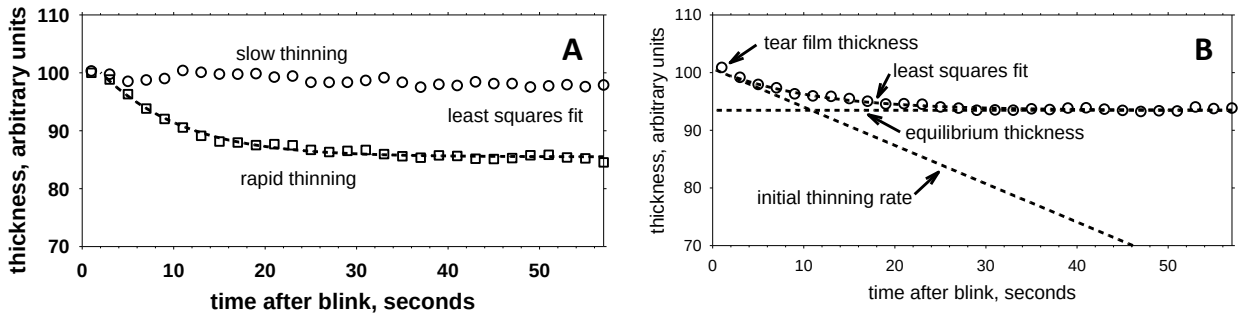

Fig. 20. A. Examples of rapid and slow thinning of the pre-conjunctival tear film in two subjects are shown (circles and squares). The dashed line shows the fit of a model based on constant evaporation and increasing osmotic flow through the corneal surface. These should be compared to corresponding curves for the pre-corneal tear film in Fig. 19A. B. Average thinning curve are shown for the pre-conjunctival tear film for 15 subjects in the rapid case, together with a least squares fit of the model (dashed curve). The initial thinning rate is less than for the pre-corneal tear film shown in Fig. 19B, perhaps because of increased outward osmotic flow relative to the cornea.

We now turn to solving the mathematical model for the evaporating pre-corneal tear film. The theoretical treatment of the local region that corresponds to a spot measurement where the tear film is assumed to be flat. When the tear film surface is assumed to be flat, with no variation along the film, conservation of mass leads to

$$hc = 1, \qquad (6)$$

when one normalizes with c_0 and the initial thickness of the tear film d' as we do here. Assuming a constant normalized rate of thinning due to evaporation, $J = J_0$, the tear film thickness is governed by

$$\frac{dh}{dt} = P_c(c - 1) - J_0. \qquad (7)$$

If the normalization d'/v_0 is used for the time, then $J_0 = 1$. Eliminating c from the last equation yields

$$\frac{dh}{dt} = P_c\left(\frac{1}{h} - 1\right) - J_0. \qquad (8)$$

The dimensional initial value for the tear film thickness is assumed to be 3.5 μm and is used to normalize the thickness so that the initial thickness is $h(0) = 1$; the model is solved for a 60 s period. The osmolarity may then be found using mass conservation. The (numerically) computed solution for the thickness $h(t)$ are the dashed curves indicated in Figs. 19 and 20. To obtain these curves, a least squares fit is performed using the initial thinning rate and the permeability of the cornea as parameters. In terms of the parameters from Levin and Verkman (2004), the permeability as derived from Fig. 19B is $P_f = 12.1$ μm/s when treating the cornea as single zero-thickness semi-permeable membrane. We can express this permeability using the notation of Fatt and Weissman (1992); in that case, the total flow resistance for the cornea is $R_t = 8.06 \times 10^{11}$ dyn s /cm^5. This value is more than three times the resistance given in Fatt and Weissman (1992) for a composite model from various animal tissues measured *in vitro*. However, this permeability is in the range of some other animal tissue measurements (Klyce and Russell, 1979); this occurs despite the fact that some of the assumptions there are different than in our work.

The rapid or slow thinning cases are based on the initial thinning rates, which are determined from the initial slopes of the solution curves. From Fig. 19B, the initial thinning rate for the pre-corneal tear film was 2.5 μm/min. From Fig. 20B, the initial thinning rate for the pre-conjunctival tear film was 1.4 μm/min and the permeability of the conjunctiva was determined to be 55.4 μm/s.

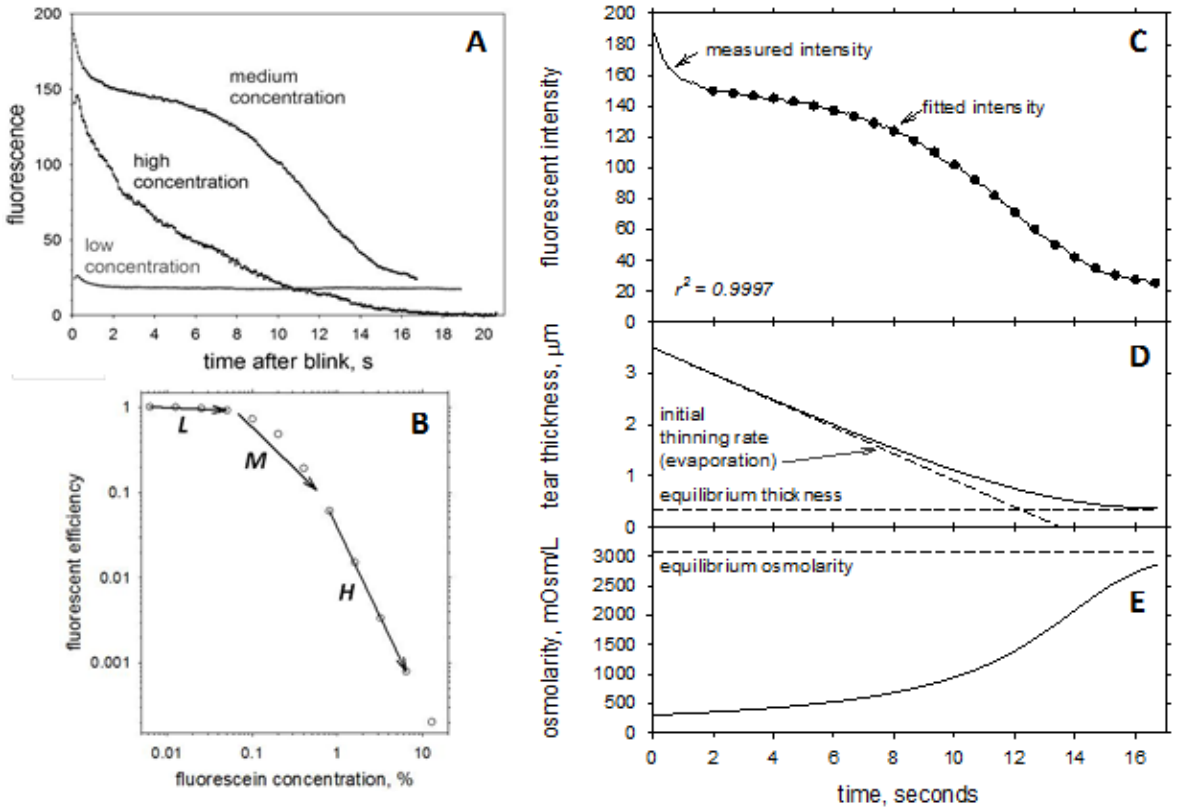

Fig. 21. A. Decay of fluorescence for 3 different concentrations of fluorescein in the tear film. DE, 68 year old white male. For the high and medium concentration conditions, 1 µL of 10% and 0.2 µL of 2% fluorescein were instilled, For the low concentration condition, another attempt was made to instill 0.2 µL of 2% fluorescein but most of the fluorescein remained in the micropipette tip so only a small amount was instilled. Fluorescence was averaged over a circular area of radius 3 pixels. Eye movements were tracked by a cross-correlation method and the video recording was "stabilized" by compensating for these eye movements (King-Smith et al., 2013b). Measurements were performed on different days. B. Self quenching of fluorescence of fluorescein. Circles are measurements of (Nichols et al., 2012). Arrows labeled ***L***, ***M*** and ***H*** help explain the decay of fluorescence for low, medium and high fluorescein concentrations in Panel A. The arrows show the reduction of fluorescent efficiency when the fluorescein concentration is increased by a factor of 8 by evaporative thinning to 1/8th of the original thickness after a blink. C, D and E. Analysis of the decay curve for medium fluorescein concentration in A. C. Flourescent intensity versus time after blink. Curve gives the measured intensity while circles give the fitted intensity curve starting 2 seconds after the blink to omit the initial transient thought to be due to upward drift. D. Calculated tear thickness assuming that the initial tear thickness is 3.5 µm. E. Calculated osmolarity. See text for details.

Fig. 21A shows the effect of fluorescein concentration on decay of fluorescence in a patient with evaporative DE. There is a large decay for the high concentration of fluorescein but little decay for the low concentration condition (a slight decay for about the first 2 seconds after the blink was probably related to the upward drift of the tear film after a blink – Section 4.1). Fig. 21B shows the

self-quenching of fluorescence of fluorescein solutions, i.e., the reduction of fluorescent efficiency caused by increasing concentration of fluorescein (Nichols et al., 2012). If the decay of fluorescence is due to evaporation causing increased fluorescein concentration, then there will be little fall in efficiency for a low initial fluorescein concentration – arrow ***L***. A large fall in efficiency is expected in the high concentration condition – arrow ***H***. The recordings of Panel A are in agreement with these observations thus supporting the proposal that the decay of fluorescence is due to the effects of evaporation and quenching. The predicted decay for the medium concentration condition, Arrow ***M*** in Panel B, is that decay should be slow at first and then more rapid as the slope of the quenching function in Panel B increases. Again, the observed fluorescence decay curve in Panel A obeys these predictions after allowing for a rapid initial decay for about 2 seconds after the blink, probably related to the upward flow in Section 4.1.

The fluorescence decay results in Fig. 21A were used to evaluate a model based on evaporation, quenching and osmotic flow through the corneal surface. The medium fluorescein concentration was used because the final fluorescence in the high concentration condition was so small that the measurements suffered from noise and stray light (the final fluorescence for the medium concentration condition can be seen to be considerably higher than for the high concentration condition). In Fig. 21C, the curve is the measured fluorescence from Fig. 21A and the circles gives a least squares fit to this function starting 2 seconds after the blink to omit an initial transient probably related to upward drift (Section 4.1). Parameters adjusted for the best fit were, first, the initial concentration of fluorescein, second, the evaporation rate (relative to initial tear thickness), third, the osmotic permeability of the corneal surface (again relative to initial tear thickness) and fourth, a response scaling factor (related to illumination level and video recording system sensitivity, I_0 in Eqn. (9)). The equations of Section 7.2 were used for the model. The model was found to be a good fit to the fluorescence decay curve ($r^2 = 0.9997$). Fig. 21D shows the tear film thinning curve assuming an initial thickness of 3.5 μm (the fit in Fig. 21C is independent of this assumed initial thickness). The dashed curve labeled "initial thinning rate" shows the effect of evaporation without any osmotic flow. The dashed curve labeled "equilibrium thickness" is the thickness which would be reached finally when osmotic flow exactly matched evaporation rate. Fig. 21E shows the increase in osmolarity which rises to nearly 3000 mOsM. The "equilibrium osmolarity" is the osmolarity which would be reached finally when osmotic flow exactly matched evaporation rate. It should be noted that initial osmolarity of the tear film and corneal epithelium is assumed to be 300 mOsM but the calculated osmolarity does not depend on the assumed value of initial tear film thickness. This calculation is based on the assumption that evaporation and tear film thickness are spatially uniform; complications due to non-uniformity of spatial characteristics are discussed in Section 5.3.6.

The theory is clearly able to fit the data very well, and to give an estimate for the permeability that is comparable to previous measurements. It should be noted that the estimates of water permeability and initial thinning rates are dependent on (and proportional to) the assumed thickness of the pre-corneal and pre-conjunctival tear film of 3.5 μm.

5.3.4 Theory over the exposed ocular surface

The value of the osmolarity and other solute concentrations that occur in the tear film may be affected by diffusion and advection (fluid motion). We have computed overall tear film dynamics for the interblink period over the exposed ocular surface using these assumptions; the details of model used and problem solved are given in Appendix 7.6. A sketch of the eye-shaped domain on which we solved the problem is shown in Fig. 22. In this section, P_f^{tiss} will take on different values over different parts of the ocular surface; when normalized this variable permeability is $P_c = P_{c0}(x, y)$ and it is a function of location. We note that the boundary conditions for the flux of the aqueous fluid were time dependent corresponding to lacrimal supply and punctual drainage in a flux cycle that was designed to mimic blinks, but the lid margins of the domain were stationary.

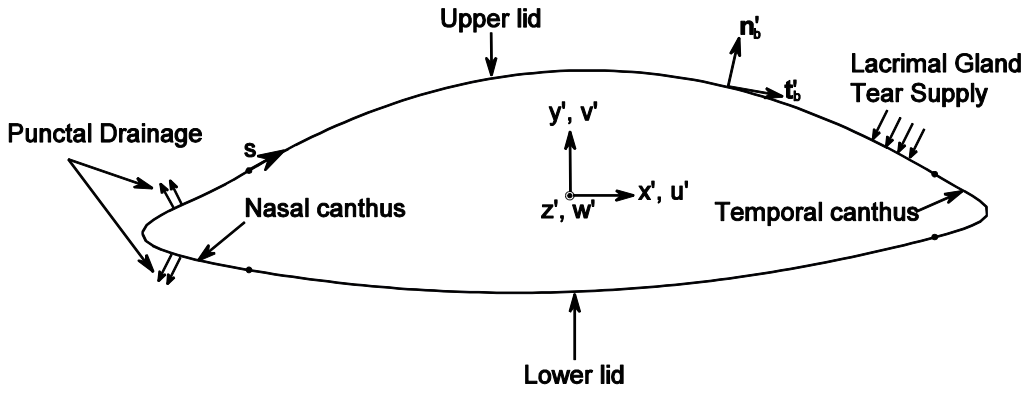

Fig. 22. Sketch of eye-shaped domain problem. The arc length variable s defines locations around the boundary; $\mathbf{n}_b'$ and $\mathbf{t}_b'$ are the unit normal and tangential vectors to the boundary. Detailed equations inside the domain and plots of the flux boundary condition are given in Appendix 7.6.

We note that in this model, the permeability of the cornea to water, $P_{corn}^{tiss} = 12.1\mu m/s$, is smaller than the permeability of the conjunctiva, $P_{conj}^{tiss} = 55.4\mu m/s$, based on estimates discussed above. Evaporation that matches experimental thinning rate of 4μm/min is also included, as is surface tension and viscosity for a single layer of tear fluid (there is not a separate lipid layer present). In this section, the diffusivity of salt and fluorescein are assumed equal and to be that of the salt value from Zubkov et al. (2012), and the isotonic osmolarity is 302 mOsM. We focus on results for the thickness, osmolarity (Li et al., 2014a) and fluorescence distributions over the exposed ocular surface shown in Figs. 23 and 24. The latter are new in this work. In Fig. 23, the left column of color contour plots is the tear film thickness at several times, and the right column is the osmolarity at the same times. The tear film thins overall, and this is more noticeable away from the menisci. Black lines form, as has been recovered in many theoretical models; this is the dark blue ring inside but not adjacent to the lid margins. The tear film has a relative thickness of 3 or more (15μm or more dimensionally) in the maroon band adjacent to the lid margins. The tear

film becomes thinner over the cornea due to its lower permeability, and this appears as the circular disk region in the left column of Fig. 23.

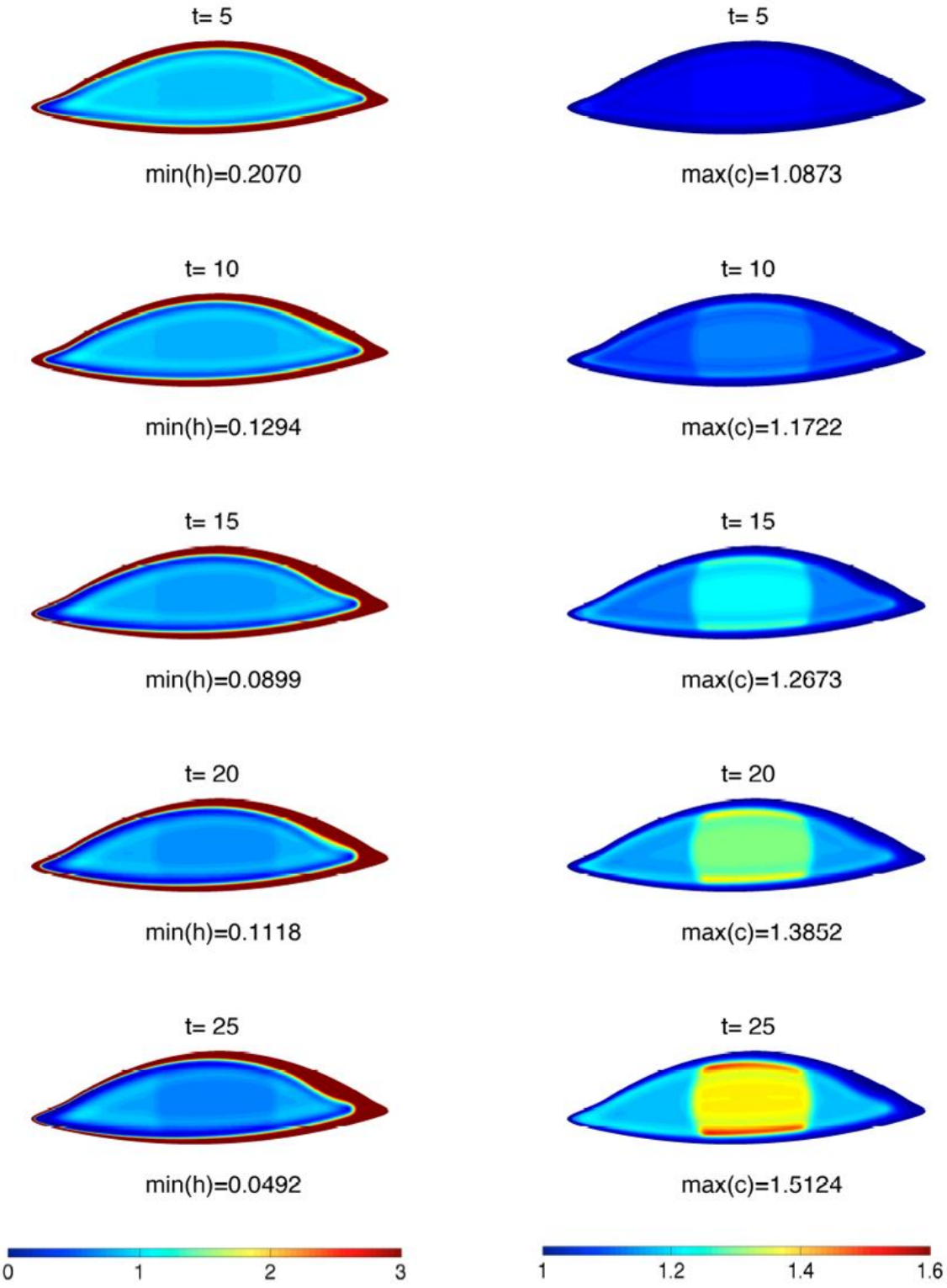

Fig. 23. Computed thickness (left) and osmolarity (right) for 4 micron/min thinning rate and $P_c = P_c(x, y)$, which has a lower permeability for the cornea than the conjunctiva. Both plots are for normalized quantities. (color on web and in print)

The osmolarity increases as the tear film thins due to mass conservation of the solutes; they neither evaporate with the water nor penetrate the ocular surface. The osmolarity increases more over the cornea than the conjunctiva, and the osmolarity is highest in black lines over the cornea. In this simulation lasting 25 s, the maximum value over the exposed is about 1.5 times the isotonic value, resulting in about 450 mOsM. This is just at the sensory threshold (Liu et al., 2009). For a thinning rate of 10 μm/min, this value is increased to about 900 mOsM, while at 20 μm/min, it is increased to very large values, 1830 mOsM at 25 s. It is likely that a subject would blink before reaching such large values, but these values may possibly be reached if the subject is performing a task with intense concentration or is in a controlled experiment and asked not to blink (Cruz et al., 2011; Wu et al., 2014). Results at other times are given in Table 1; such long times are not needed to reach what is currently thought to be high osmolarities in the menisci over the cornea. Perhaps these elevated values help signal partial blinking, which occurs frequently (Cruz et al., 2011; Doane, 1980; Wu et al., 2014).

Table 1. The maximum osmolarity in mOsM is shown for several thinning rates for model over the exposed ocular surface.

Time (sec)	1 μm/min	4 μm/min	10 μm/min	20 μm/min
5	308	328	374	472
10	314	354	456	831
15	319	383	601	1610
20	326	418	787	1800
25	332	457	951	1830

Fig. 24 shows the distribution of fluorescent intensity over the exposed ocular surface. . We use Eq. (9) of Appendix 7.2 to convert FL concentration f to intensity I, but it also depends on the thickness of the tear film h. Both f and h are computed dynamically in the model and are subsequently converted to I using Eq. (9). That computed intensity is shown in the contour plots. A dilute initial concentration that is 20 times less than the critical concentration $f_{cr} = 0.2\%$ is shown in the left column; in the right column, the initial concentration is at f_{cr}. In the dilute case, essentially nothing happens except for a widening of the meniscus due to influx of aqueous from the lacrimal gland. This happens because the interior of the tear film has little flow, leading to mass conservation in that case being closely approximated by $hf = f_0$ in our normalization. That product appears in the equation for the intensity but stays smaller than unity in the denominator, leading to the intensity being approximately constant there. In the right column, f is in the quenching regime, and so as the tear film thins, the intensity drops in the interior, and more so over the cornea where thinning is greater. In this case, the drop in intensity is because f is larger than unity and the denominator causes the intensity to drop with inverse square power of f.

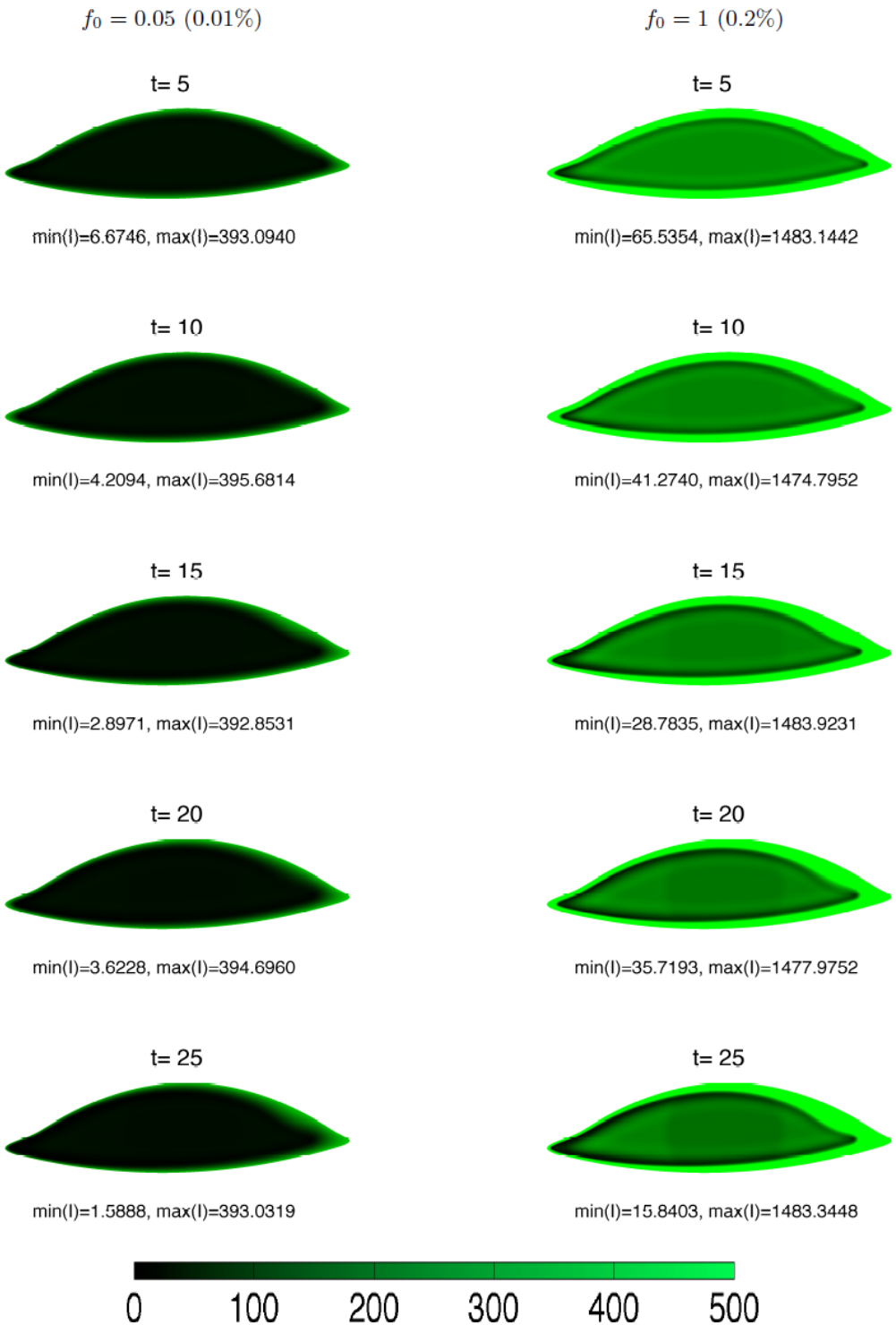

Fig. 24. Computed FL intensity for the dilute case (left) and quenching case (right) for 4 micron/min thinning rate and $P_c = P_c(x, y)$. The intensity is an arbitrary scale. (color on web and in print)

5.3.5 Tear film break up: experiment

In this section we give experimental results on TBU using several imaging techniques.

Tear film instability has traditionally been viewed following instillation of sodium fluorescein and TBUT measured. TBUT is defined as the time until the first break in the tear film occurs (Norn, 1969). but the tear film can be imaged well beyond that point to obtain more quantitative measures of its overall dynamics and instability (Begley et al., 2013; Begley et al., 2006; Liu et al., 2006). Fluorescence quenching of fluorescein allows interpretation of relative thickness changes (see above) during tear film instability to quantify tear film instability in the inter-blink period (Begley et al., 2013).

Other measures of TBU can also be used to visualize TBU and do not involve instillation of fluorescein drops. Some of these methods delineate "edges" of TBU or other optical disturbances (Himebaugh et al., 2012; Szczesna et al., 2010). but may not contain information about overall uniform thinning of the tear film (Guillon and Maissa, 2010; Himebaugh et al., 2012; Szczesna et al., 2010). One of these non-invasive methods, retroillumination of the tear film, is a high resolution imaging method that shows local intensity differences where TBU is located. Thus, even though it does not detect overall thinning of the tears, it can be used to quantitatively map optical aberrations produced by local areas of tear film disruption. Intensity bands in these images are thought to represent the slope of edges of TBU, so that mathematical integration of the intensity values can be used to obtain thickness changes and reconstruct the original surface (Himebaugh et al., 2003).

Thus, the fluorescein method for tear film imaging is not ideal because it involves instillation of fluid, the concentration of fluorescein is usually unknown, and concentration quenching of fluorescein molecules complicates interpretation of the images due to a two part solution for fluorescence intensity (Nichols et al., 2012). However, fluorescein imaging of the tear film is considered the "classic" clinical method and concentration quenching of fluorescein molecules allows viewing of local and overall tear film thinning (see above). For these reasons, simultaneous fluorescein (FL) and retroillumination (RI) imaging of the tear film during TBU and thinning was implemented to track dynamic changes in the tear film thickness. Because the two methods were completely independent of each other and were recorded on different cameras (aligned and registered with each other), the results from each support interpretation of the dynamics of tear film instability.

Fig. 25 shows FL images of TBU progressing over an approximately 24 second time period. RI images taken at the same time period are adjacent to the FL images and the red boxes on both represent the area studied. The surface maps for FL images show areas of TBU deepening with time. A flat surface (constant tear thickness) is represented by a certain intensity in the RI image whereas positive or negative surface slopes are represented by higher or lower intensities. RI images have been integrated (in the sense of the calculus from mathematics) to obtain changes in thickness. A baseline tear film thickness must be assumed because integration introduces an arbitrary constant that is not determined separately by the methods. It is clear from Fig. 25 that both sets of surface maps, obtained by very different methods, show a similar deepening of the area of TBU with time.

In order to measure the correlation between the two types of images and to estimate tear film thinning rates, a line was drawn across an area of TBU (Fig. 26). This line was within the red box shown in Fig. 25. Fluorescein and retroillumination images at the top of Fig. 26 show this area changed over time as TBU occurred. Surface maps at the bottom of Fig. 26 show the effect of time on the area demarcated by the red line, demonstrating a locally thinning area in both fluorescein and retroillumination images. The correlation between fluorescein and retroillumination images at the end of TBU was very high (r=0.889 in this case).

Fig. 27 shows relative thinning rates in two locations (white lines) shown in Fig. 26.

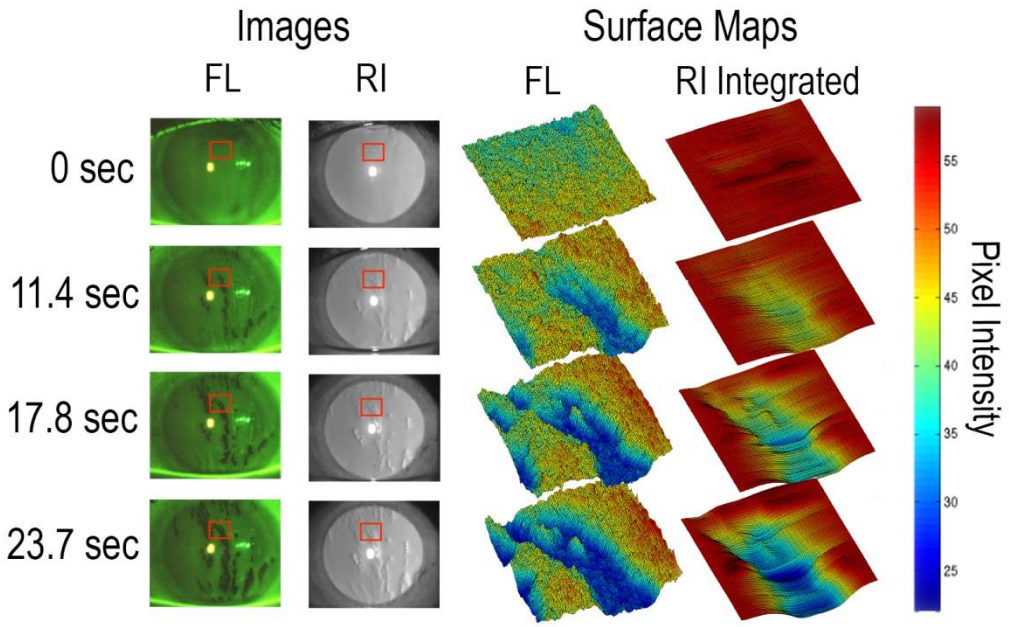

Fig. 25. First column: FL images of the ocular surface in actual color. Second column: Simultaneous RI images of the same area. Third column: False color images from FL column intensity for the area in the indicated red square. TBU regions emerge and spread as dark blue regions of low intensity. Fourth column: False color images from RI column for the area inside the red square. The edges of the TBU region in the RI image appear to have more gradual slopes than those in the FL image; see text for discussion. (color on web and in print)

It appears that TBU region in the FL image in Fig. 26 has steeper sides than the corresponding RI image there. In our theoretical calculation below, we see that the interpretation of the TBU region in the FL images requires some care.

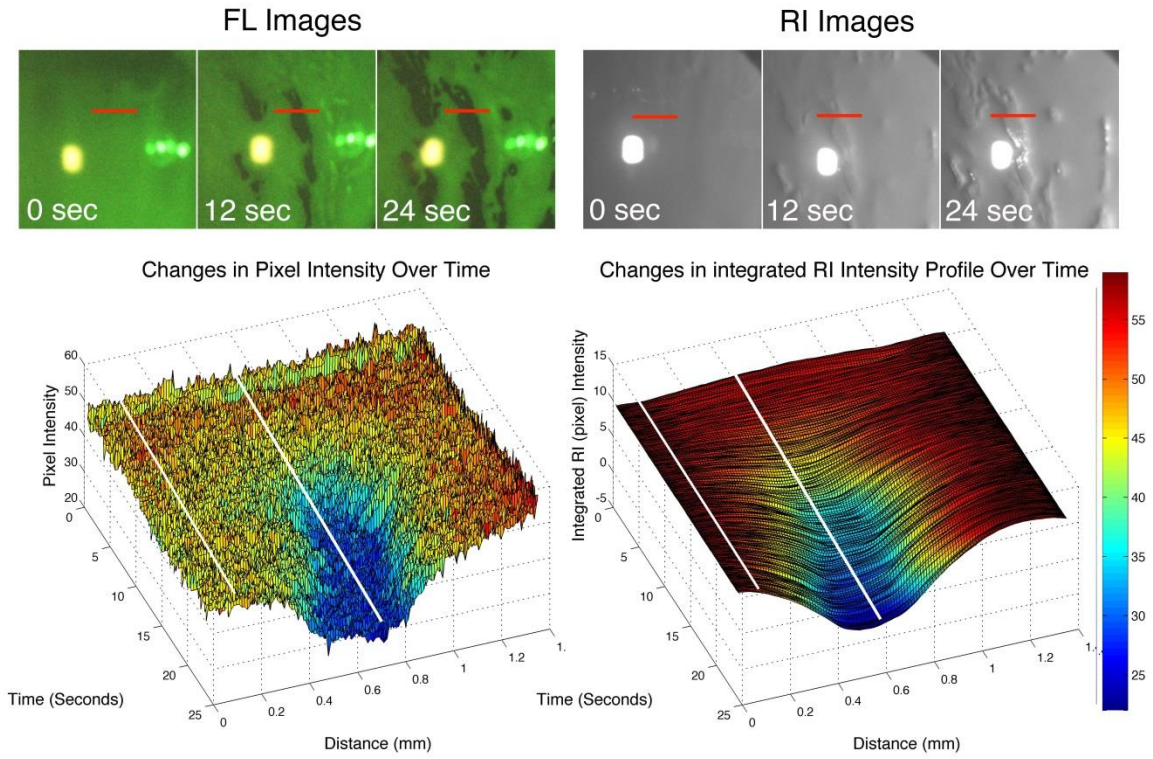

Fig. 26. Processed results from the FL and RI images. The red line segment in the reference FL (top left) and RI (top right) images indicates the location of the data at each time. The FL surface plot (lower left) has been converted to false color; the RI surface plot (lower right) uses this and an integration of the intensity to obtain the thickness values. In both cases, an initial value is assumed when converted to estimating the tear film thickness. (color on web and in print)

The FL images can be further processed to calculate the thickness when the FL concentration is in the quenching regime (Braun et al., 2014; Nichols et al., 2012). Effectively when the concentration is above the critical FL concentration f_{cr}, the thickness is, to a good approximation, proportional to the square root of the intensity. This method requires an estimate for the initial thickness. Results for this case shown in Figure 26 are given in Fig. 27. The two curves plotted correspond to the locations shown by the white lines in Fig. 26, with one inside the TBU region and one outside. The location outside changes little, but there is a rapid decrease in the thickness of the tear film in the TBU region. We compare with theory for the TBU region next.

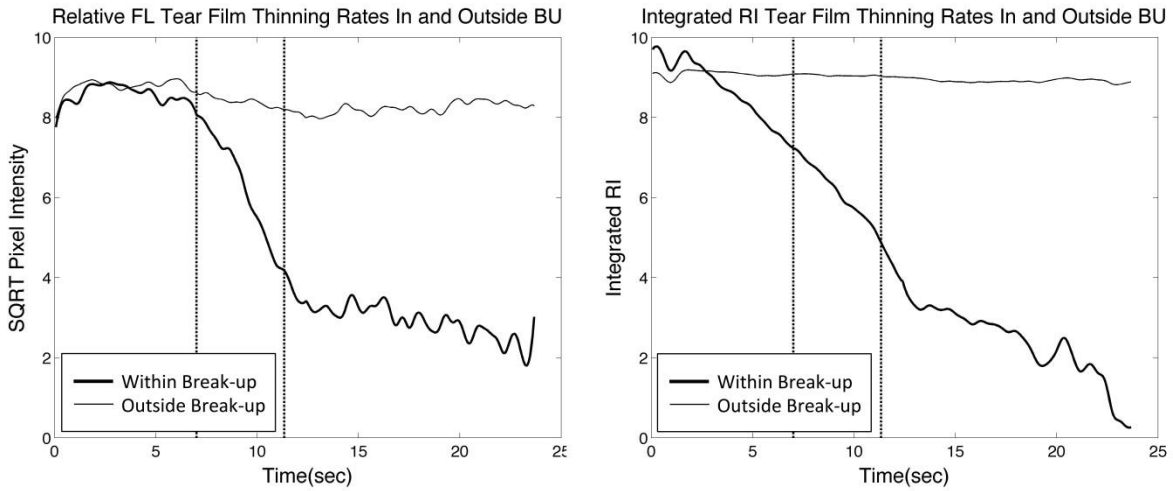

Fig. 27. The square root of FL intensity (left) and integrated RI intensity (right, scaled to the same ranges as the FL plot) as a function of time for the locations indicated in Fig. 19. In the TBU region, the FL plot shows an initial delay then a rapid decrease. The RI plot shows a consistent decrease.

5.3.6 Tear film break up: theory

To date, theoretical models of TBU have used heavily simplified models of the tear film. Some have used no lipid layer but a simplified surface behavior that approximates a very strong surfactant limit (Winter et al., 2010). Others have used different simplifications to describe In another recent approach, an immobile lipid layer with fixed thickness with an improved approximation to the resistance of evaporation from the lipid layer and the surrounding air (Peng et al., 2014). Still others have used multilayer models with an explicit mucin layer that was thought to drive TBU but with no explicit lipid layer or osmolarity (Zhang et al., 2003). A fully dynamic model of localized TBU that has dynamic lipid and aqueous layers together with an evaporation rate that depends on the lipid layer has yet to solved.

In this paper, results are computed from models that simplify the lipid layer and its role affecting evaporation rate but includes osmolarity and fluorescence in the TBU region. The details of the problem solved here for TBU is given in the Appendix 7.5. The purpose of the theory here is to compare closely with the TBU observations of the previous section to both understand the observations better and to predict the osmolarity in TBU for those experimental condtions.

Several levels of such models have predicted elevated osmolarity. Our model above for a spatially-uniform thinning tear film predicted values above 3000 mOsM. Peng et al. (2014) included a fixed narrow distribution with a stationary lipid layer but took into account the vapor transport outside the tear film; they included the extreme case of 38 μm/min peak evaporation rate. They found around 1850 mOsM peak values in the TBU region, and that increasing diffusion reduces the peak value of osmolarity. Here we include fluorescence as well in order to directly compare with the experimental observations *in vivo*.

To compute the theoretical curves, we assumed an initial thickness of 3.5 μm, initial FL concentration at one-third of the critical value (0.0667%), a diffusivity of FL that is 0.39 cm^2/s (Casalini et al., 2011), a permeability of the ocular surface to water of 12.1 μm/s as measuredabove, and a tangentially-immobile tear/air interface. A fixed Gaussian evaporation distribution with 0.13mm standard deviation, 1 micron/min background thinning rate and peak rate of 30 μm/min was used to recover the same time for thinning observed *in vivo* above. The width of the distribution was chosen to be compatible with hypothesized lipid variation based on the spacing of the meibomian orifices (references) and observed lipid patterns *in vivo* (Goto and Tseng, 2003; King-Smith et al., 2009) .

In Fig. 28, contour plots of the dependent variables h, c, f and the estimate of the tear film thickness $\alpha\sqrt{I}$ computed from a model of TBU, are shown. The tear film thins in response to a narrow Gaussian distribution of evaporation. The thickness decreases to about 0.082 of its original thickness, and this causes both c and f to rise due to mass conservation. However, the fluid motion and diffusion modify the peak values from the spatially uniform case. The osmolarity rises to a peak value of 1900 mOsM (about 6.33 times the initial value) and the fluorescein reaches a maximum of about 14 times its original value in the TBU. This large value of osmolarity is lower than the estimate for the spatially uniform case (e.g., Fig TE) because it diffuses away from the large peak sufficiently fast in the computed time interval. Nonetheless, the osmolarity is clearly large enough to be perceived as painful (Liu et al., 2009) and can lead to potential irritation and damage (Begley et al., 2002). The peak fluorescein concentration is is raised by a larger factor than peak osmolarity because it diffuses more slowly than the relatively small ions contributing to the osmolarity. The smaller diffusivity of f compared to the osmolarity definitely led to better agreementthan choosing equal diffusivities. . Using the intensity function from the appendix, we estimated the thickness using $a\sqrt{I}$, corresponding to the quenching regime (Nichols et al., 2012). The thickness estimate from the intensity in the quenching regime is a bit narrower than the computed thickness from the model. We note that the final thickness and the peak values of the solutes depend on the initial thickness of the tear film in our model.

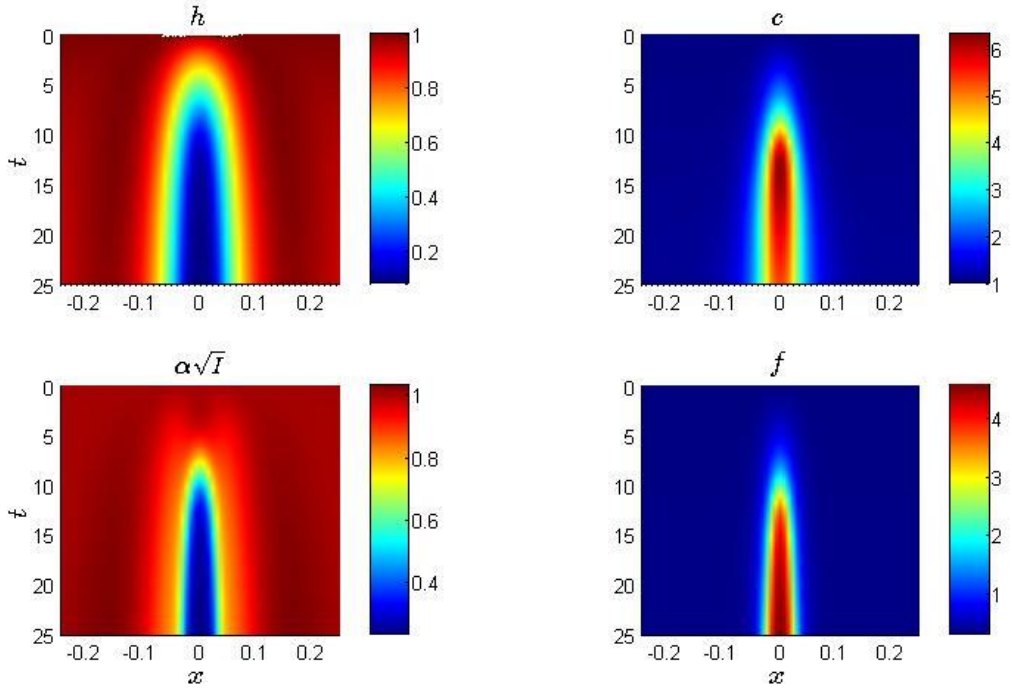

Fig. 28. Contour plots of the dependent variables h, c, f and the estimate of the tear film thickness $\alpha\sqrt{I}$ computed from a model of TBU, shown clockwise from upper left. The vertical axis is time, increasing downward; the horizontal axis is normalized location with a width of 2.5 mm. Note that the fluorescein concentration starts at a uniform value of 1/3, while the osmolarity starts with a uniform value of unity. See text for discussion. (color on web and in print)

A sketch of the competing processes in the TBU region is shown in Figure 29 (after King-Smith et al. (2013c)). In this view, the TBU is driven by loss of water via evaporation to the environment. The tear film thins as a result, and solutes are left behind with increasing concentration in an area of low pressure Partially compensating for the loss of water from evaporation in the breakup region, some water is replenished by osmotic flow out of the cornea and some by water flow into the central low pressure region. The solutes are carried ("advected") by fluid motion toward the low pressure in the center of the TBU and they also diffuse via the usual Fickian diffusion from high to low concentration. The directions of these processes are indicated in the figure by arrows. The relative importance of the advection and diffusion are important. The ions of salts are relatively small and diffuse about 4 times more rapidly (Riquelme et al., 2007) than the larger FL ions (Casalini et al., 2011). Because of this, the osmolarity in the TBU starts to drop by 15 s post-blink, even though fluid motion is toward the center of TBU. The FL concentration continues to rise because it does not diffuse fast enough to overcome the flow toward the center of the TBU region. The drop in the osmolarity is different than the spatially uniform result in Fig. 21, Panel E, because in that case there is no diffusion along the tear film to lower the maximum osmolarity. The result in Fig. 21 may still be applicable to a region which is thinning relatively uniformly in a wide space, but for localized TBU, we would expect diffusion to mitigate the osmolarity increase somewhat based on our results here and on previous results (Peng et al., 2014).

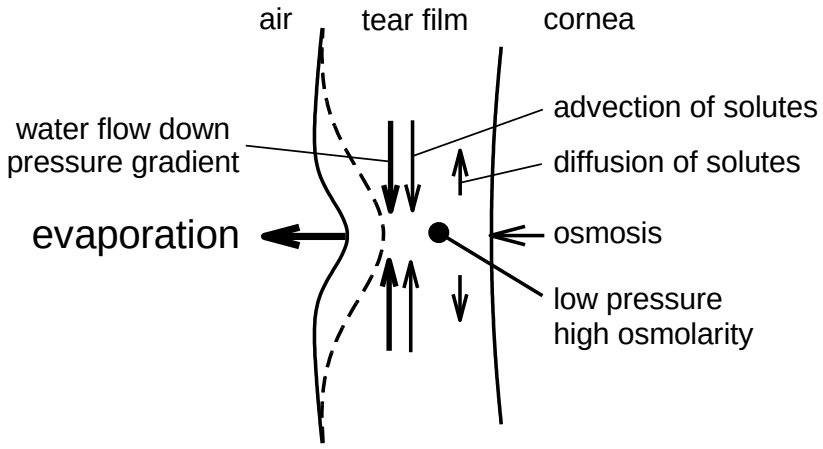

Figure 29. Sketch of the dominant processes in TBU. The outer surface of the tear film is indicated at an early time (solid line) and a later time (dashed line). See text for discussion.

We plotted the extrema of the dependent variables and a detailed comparison on the computed thickness h and the estimate $a\sqrt{I}$ in Fig. 30. In this figure, it may be easier to see that the thickness decreases and remains small while the osmolarity peaks around 13 s at a normalized value of about 6.33 and then decreases. The maximum f begins at 1/3 and increases by about a factor of 14 to about 4.6 at 25 s. As mentioned above, the larger diffusion of c is responsible for the decrease, while f does not because of its diffusivity is roughly four times smaller. There is a small flow of fluid toward the center of the TBU region due to surface tension and the shape of the tear film (Fig. 29); this tends to bring solutes toward the center of the TBU region, and if the solute diffuses too slowly, its concentration builds up there for a time. This is why f becomes relatively large there and does not yet decrease during the time interval of our computation. The comparison of the computed h and the estimate from the intensity are not very close for the parameters that we used; the time to the minimum values are essentially the same however. The same time course appears to agree with the simultaneous RI imaging in the sense that the rough texture of the cornea becomes visible by 15 s, so we believe that TBU has occurred by that time.

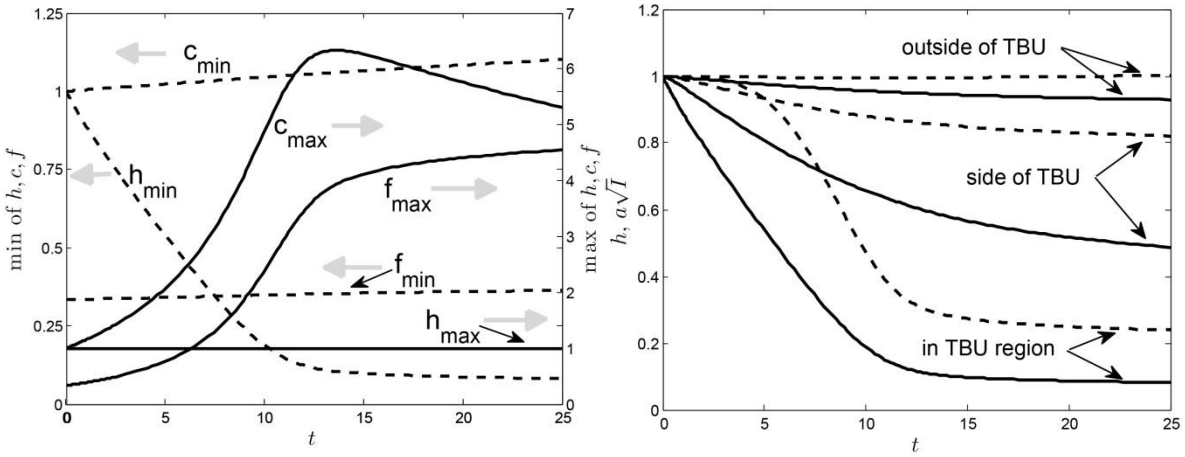

Fig. 30. Left: Maxima (solid curves, right axis) and minima (dashed, left axis) for h, c and f for the model of TBU. The grey arrows point to the corresponding axis. The maximum c, normalized to $c_0 = 300$ mOsM, is about 6.33 or 1900 mOsM dimensionally. The maximum f is about 14 times its initial value of 1/3 (relative to f_{cr}). Right: Theoretical results with initial time corresponding to the start of the rapid thinning of Fig. 27. The curves in TBU and outside of TBU correspond to the curves shown there. The dashed curved are proportional to the square root of the intensity, the solid curves are computed thickness. The factor a was used here to normalize the initial values of the intensity to one for each location.

In our computations we found that the results depended, among other parameters, on the initial value of the TF thickness, the initial FL concentration, the thinning (evaporation) rate, the permeability of the ocular surface to water and the diffusivity of the FL in water. Using a "medium" concentration less than f_{cr} and the literature value of D_f gave a good approximation to the time delay in the decrease of the FL intensity and the relative steepness of the sides of TBU. The initial tear film larger than 3 μm also led to better agreement between the computed thickness and the indirect calculation of the thickness from the intensity. Fast evaporation in the TBU was required for good agreement as well.

If the thinning in the TBU region were fit only to the fast decrease indicated by the vertical lines in Fig. 27, then it is assumed that there is no delay of the FL intensity compared to thinning. In this case, a good fit to the thickness was found $f(0) = 1$ (that is, at critical concentration) and that $D_f = 1.2 \times 10^{-6}$ cm²/s (about the same diffusivity as a protein). Both the rate of thinning and the final values of the h and $a\sqrt{I}$ agreed well in this case, but the initial decay was absent. Both of these parameter values are plausible, but in this experiment it appears that the initial f was below the critical concentration and that there was a delay in FL intensity decrease while the concentration built up to reach the quenching regime. This agrees well with the results in Section 5.3.3.

The agreement between the actual computed thickness and the square root of the intensity was worst in the sides of the TBU region. Though the inside and outside of the TBU agreed well between these two calculations, the sides clearly had $a\sqrt{I} > h$, which is consistent with the FL images appearing to have steeper sides than the RI image.

5.3.7 Sensory perception experiments

The elevated osmolarity over the corneal surface modeled in the previous section cannot be measured directly by current techniques. Measurements of tear film osmolarity from the inferior tear meniscus rarely exceed 400 mOsM (Gilbard et al., 1978; Lemp et al., 2011; Tomlinson et al., 2006; Versura et al., 2010), even though the threshold for sensation of hyperosmolarity is approximately 450 mOsM (Liu et al., 2009). However, there is supporting evidence for marked increases in osmolarity of the tear film by examining the sensory response to TBU and thinning. Sharp increases in ocular discomfort accompany the development of TBU and slow thinning of the tear film is known to be associated with similarly slow increases in burning and stinging (Begley et al., 2013; Varikooty and Simpson, 2009). Fig. 31 is an example of the sensory response to TBU and tear thinning. In this example, 2 microliters of 2% fluorescein dye was instilled into

the eye and the subject was asked to keep one eye open as long as possible while the subject monitored discomfort on a 0-10 scale. Tear film fluorescence was monitored and surface maps created (as in Section 5.3.5 above) showing differences in relative tear film thickness over time. As Fig. 31 shows, discomfort markedly increased when TBU occurred, with presumed spikes in tear film osmolarity and possible drying/surface deformation as TBU deepened. Although not shown in Fig. 31, the quality of the increasing discomfort was described as irritation, pain and burning, which is consistent with the idea of increased hyperosmolarity within local areas of TBU stimulating underlying ocular surface polymodal nociceptors or cold receptors (Acosta et al., 2001; Parra et al., 2014). Thus, the discomfort associated with DE may have origins in repeated stress to the ocular surface by TBU (Begley et al., 2013), which may, in part, explain the increase in DE symptoms noted later in the day .

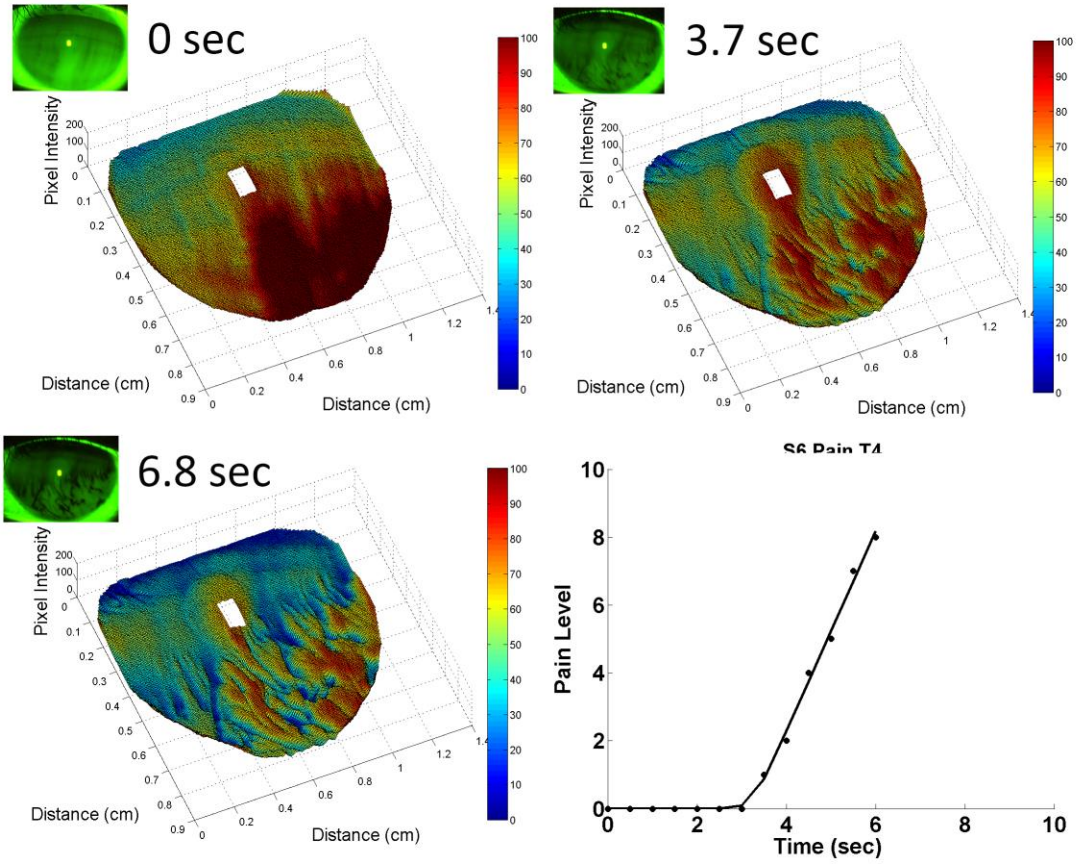

Fig.31. FL images with surface maps of relative tear film thickness over a 6.8 sec time period (white area within each surface map is a reflection) and associated sensory response. Top left: Tear film at the beginning of the trial. Top right: Tear film after 3.7sec showing thinning and some TBU. Bottom left: At 6.8 sec, more extensive and deep TBU. Bottom right: Sensory response from subject showing an increasing pain level as TBU develops. (color on web and in print)

The definition of DE includes both sensory consequences, such as discomfort, and also visual disturbances,(DEWS, 2007). Many have shown that higher order aberrations (HOA) are increased in DE (Denoyer et al., 2012; Koh et al., 2008; Montes-Mico et al., 2005). It is likely that the tear film is a major source of these aberrations, given that the largest refractive index difference in ocular media occurs between air and the tear film. As TBU progresses, spatially localized differences in tear film thickness (as shown in Figs. 25, 26 and 31) create increasing optical aberrations that decrease retinal image quality and reduce visual acuity and contrast sensitivity(Liu et al., 2010). Recent work has shown that optical scatter emerges at the base of areas of TBU, presumably as surface or mucin layer drying occurs, exposing a rough corneal surface.

5.3.8 Other observations of TBU

It is of great interest to know in detail what the elevated osmolarity in TF thinning and TBU does to the corneal epithelial cells. Yet, this is very difficult observation to make. Gipson and coworkers have discussed possible effects on the glycocalyx and transmembrane mucins (Govindarajan and Gipson, 2010). Chen et al. (2008) used in vivo exposure of cultured epithelial cells to hyperosmolar solutions to observe cornification and to identify active pathways in the chemical processes. Levin and Verkman (2004) observed thickening of mouse eyes in response to hypo-osmolar solution using FL imaging. However, there appears to little direct observation of *in vivo* epithelial cells for humans. The high resolution spectroscopic microscope (King-Smith et al., 2011) occasionally produced images with additional information besides the lipid layer. In this section, we discuss a fortuitous capture of the ocular surface itself in a TBU region using that approach.

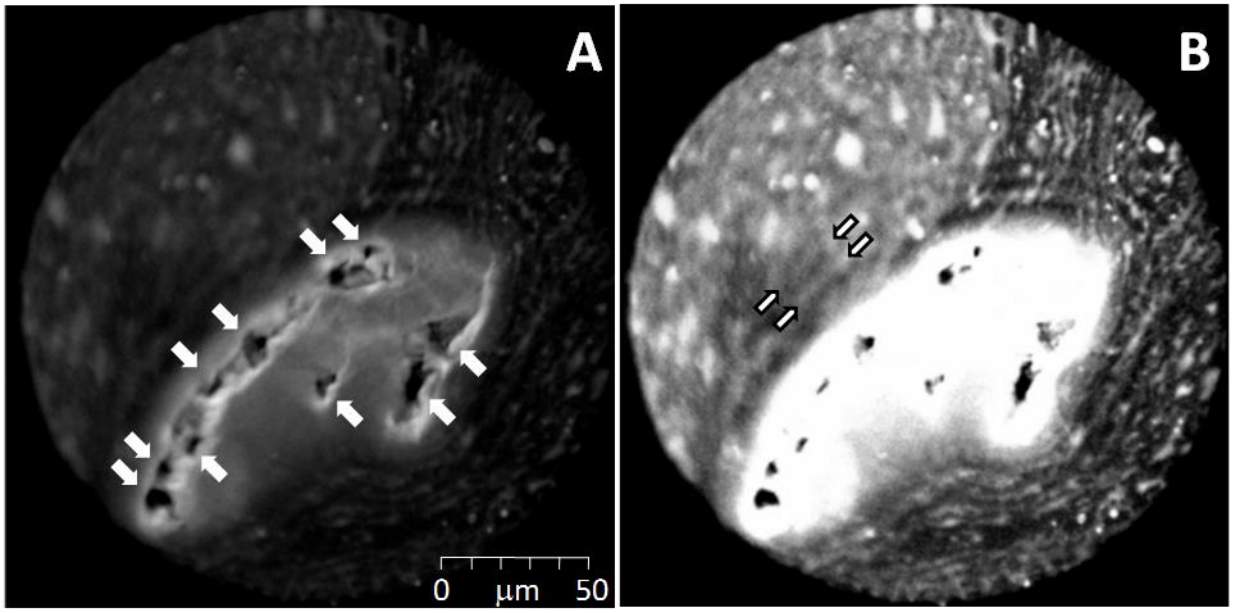

Fig, 32. A. High resolution stroboscopic micrograph recorded from a 62 year old white DE female. The light area of about 150 × 60 µm is interpreted as an area of breakup surrounded by tear film. Arrows point to dark areas which are interpreted as crevices between corneal surface cells caused by cell shrinkage. B. Image from A repeated with increased brightness and contrast,

to show details of the surrounding tear film. Interference fringes from the whole thickness of the pre-corneal tear film are seen surrounding the region of breakup, e.g., bright fringes between the arrows. White flecks in the tear film area are probably due to patches of lipid.

Fig. 32 shows high resolution images which may be interpreted as an area of tear film breakup. Arrows in Panel A indicate possible crevices between superficial corneal cells. It is proposed that localized evaporation has caused increased tear film osmolarity causing osmotic flow out of superficial corneal cells. This would induce cell shrinkage, causing cells to pull apart forming crevices as indicated by the arrows. This is consistent with evidence that evaporation is the main cause of pre-corneal tear film thinning between blinks and tear film breakup (Kimball et al., 2010; King-Smith et al., 2009; King-Smith et al., 2008; King-Smith et al., 2013b; King-Smith et al., 2013c; Nichols et al., 2012). Panel B is the same image with increased brightness and contrast, to show details of the surrounding tear film. Interference fringes corresponding to the whole thickness of the pre-corneal tear film are seen surrounding the region of breakup. Arrows indicate bright fringes – the thickness difference between neighboring bright fringes is about 200 nm. White flecks probably correspond to patches of thicker lipid.

6. Summary and Future Directions

In this review, we have emphasized recent progress in imaging and mathematical models of tear film dynamics during the blink cycle. This combination of methods has allowed a deeper understanding of the tear film and the conditions it creates for the ocular surface, including fluid motion and osmolarity over the ocular surface. In order to best describe our results, we considered the blink cycle in four parts designed to elucidate the impact of the blink on the tear film.

The new stroboscopic imaging system described here provides detailed images of lipid thickness and dynamics sufficiently quickly to observe the tear film during blinking in detail. The images obtained from this system substantiated the results of others and provided new evidence of several phenomena involving the tear film. As others have reported, repeatability of the observed lipid patterns was seen in some subjects (Bron et al., 2004), suggesting that tear film lipid turnover can be relatively slow. Lipid build up at the upper lid seems virtually certain based on our observations, and thick regions of lipid are left behind at the turning point and early part of the upstroke. In some recordings, changes in lipid structure from blink to blink were described which could contribute to the turnover of the lipid layer.

The high spatial and temporal resolution of the stroboscopic system also provided a serendipitous finding that we have termed rippling. This novel experimental observation could have been predicted when considering the effect of the downstroke and upstroke of a blink on the tear film, but has not been described elsewhere to our knowledge. We chose the term rippling because it helps to visualize the changing surface of a thin fluid rapidly moving over a rough service, similar to a shallow stream flowing over a gravel bed. Understanding of this experimentally observed phenomenon was aided by simple mathematical models of the tear film over an idealized corneal surface. Aspects of those models closely matched the observed ripples *in vivo*, lending credence to both our interpretation of the observation and the associated mathematical modeling. For

example, ripples appear in both the upstroke and the downstroke, but the offset of the peaks of the tear film compared to corneal surface changes from one to the other. These findings underscore the need for a full understanding of tear film dynamics over the blink cycle to improve our knowledge of the forces affecting the tear film and ocular surface.

It is likely that these ripples play a transient role in the optical quality improvement that others have observed during the first few seconds after a blink(Montes-Mico et al., 2005). As the ripples fade with upward drift of the tear film, the subsequent improvement, if it occurs, is likely to be due to surface-tension-driven leveling. The later decrease in optical quality is, in our view, most likely caused by evaporation-driven TBU(Kimball et al., 2010; Liu et al., 2010). It is notable that modeling predicts that thickness of the tear film affects rippling; a thinner tear film should be more affected by rippling than a thicker one. This may impact the visual disturbances that characterize the DE condition, especially in cases of aqueous deficiency(DEWS, 2007).

We used mathematical models and experimental methods to study evaporative driven thinning using FL imaging. A close match between FL imaging and a mathematical model incorporating evaporation and osmosis was found by using a medium concentration of FL and an intensity function that is valid over a wide range of FL concentration. With that understanding, the osmolarity of the uniformly thinning tear film was computed and found to be as high as ten times the isotonic value, or 3000 mOsM, in the worst case of extended eye opening with possible drying of the surface. However, even though extreme cases are probably unrealistic in natural conditions, a number of approaches, including the predictive mathematical modeling for osmolarity, recent drop testing using hyperosmolar solutions, and sensory findings, indirectly point to local spikes in tear film hyperosmolarity associated with TBU (Liu et al., 2009).

We used mathematical models to compute osmolarity and FL intensity over the exposed ocular surface during the interblink using a model for tear film supply and drainage with blinking. The resulting computation estimated osmolarity at all locations over the interpalpebral area. The peak values of osmolarity varied depending on the thinning (evaporation) rate applied in the model. For an intermediate thinning rate of 4 μm/min, the peak value was about 450 mOsM after 25 s; for rapid thinning of 20 μm/min, the peak value was about 1850 mOsM in the same time. These peak values occur in the black line over the cornea in this model, and they are lowered from the uniformly thinning film because of diffusion of solutes inside the tear film. The peak values highlight the significant variation of osmolarity over the ocular surface that may occur during the interblink, even in the absence of localized TBU away from the menisci and black line. The capability to measure osmolarity outside the inferior meniscus would all the model to be tested.

The temporal and spatial changes that occur during TBU in the interblink period were studied by simultaneous imaging of FL and RI. Although areas of TBU viewed by FL have long been termed “dry spots,” (Norn, 1969) the relative changes in tear film thickness during TBU remain unclear. FL imaging, with uncertainties in initial concentration and thickness, could be better understood when used in conjunction with RI imaging (Himebaugh et al., 2003). Thinning rates within areas of TBU, obtained using this combination of methods, are consistent with the hypothesis that locally increased rates of evaporation drive the steady deepening of TBU. In addition, tear film thinning within areas of TBU appeared “hit bottom” and stop changing with both FL and RI

methods, supporting the idea that the corneal surface was reached. It was interesting to note that the fully quenched regions at the base of TBU in FL images showed a rough texture when viewed with RI. However, we did find that the details of the FL and RI images could differ, particularly in the onset of apparent thinning and the steepness of the sides of the apparent TBU regions between the two methods. These differences could be understood by comparing detailed results from mathematical models. The computed results showed that flow of the tear fluid into the TBU inside the film, driven by capillarity, could affect the FL distribution such that the sides of the TBU would appear steeper than the corresponding tear film thickness. This is another instance of the synergy between the experimental and mathematical approaches.

Furthermore, the mathematical model was used to compute osmolarity within and around areas of TBU by employing FL intensity changes in experimental FL images. We found what appeared to be a good fit to the *in vivo* observations with rapid localized thinning rate of 30 μm/min, yielding a peak osmolarity value of approximately 1900 mOsM in that simulation. The value was similar to the interblink simulation above, and similar to modeling results of Peng et al. (2014). These estimates of local spikes of hyperosmolarity within areas of TBU greatly impact our understanding of the condition known as DE, for which tear film hyperosmolarity putatively poses a major source of repeated stress to the ocular surface and is considered a core mechanism of the condition(DEWS, 2007). Because tear film osmolarity can currently be measured only from the meniscus or fornix, these modeling results provide estimates of spatial and local changes in tear film osmolarity in the interblink period grounded in experimental FL imaging and strongly suggest that hyperosmolar stress to the underlying epithelium may be transiently quite high.

In support of this idea of local hyperosmolar stress within areas of TBU, a high-resolution micrograph from the system of King-Smith et al. (2011) captured the ocular surface in a TBU region. The image appears to show gaps between adjacent epithelial cells, presumably from shrinkage due to osmotic forces within TBU. This fits with sensory perception data presented here where subjects indicated significant increase in discomfort as TBU progressed. Imaging methods that can investigate tear film dynamics as well as epithelial cell dynamics simultaneously in humans, and that could link them to sensory perception, would be an exciting development. Mathematical models could also be developed that calculate what happens to both the tear film and the epithelial cell layers within these areas of putative high hyperosmolar stress. Possible directions have been explored for mathematical compartment models for the cell layers (Levin et al., 2006; Levin and Verkman, 2004), and continuum models for the cornea (Leung et al., 2011), but a model that combines tear film dynamics and the effect on the underlying cells would be new and informative.

The imaging and mathematical methods of this work put together a more comprehensive picture of tear film dynamics than was previously available, but much remains to be understood. The increased use of simultaneous imaging will help in the understanding of tear film dynamics, as will development of higher resolution OCT devices. However, imaging of fluorescence quenching as the tear film thins provides mathematical estimation of increases in hyperosmolarity during TBU and tear thinning, as noted here. Simultaneous imaging of the lipid layer and the aqueous layer would greatly aid understanding what we and others believe is the critical role of the lipid

layer and its influence on evaporation. It may be possible to use simultaneous interferometry, or interferometry of the lipid layer together with other imaging methods for the aqueous layer to clarify the interaction of these two tear film components. For video systems based on the usual silicon sensors, the quality of interference imaging of the precorneal tear film has been limited by low contrast (King-Smith et al., 2006). It has recently been demonstrated that considerably higher contrast can be obtained using sensors based on indium-gallium-arsenide (King-Smith et al., 2014), indicating the potential for improved interferometric imaging of the aqueous tear film.

A significant future challenge for theoreticians is to produce mathematical models with a dynamic lipid layer that interacts with evaporation in a sensible way to cause TBU. Such models may add a new level of accuracy to the predictions of osmolarity in TBU regions. They may also greatly aid in understanding the function and properties of the lipid layer, as well as testing of multilamellar models of the lipid layer structure (King-Smith et al., 2013a; Leiske et al., 2012; Rosenfeld et al., 2013). Another challenge is a tear film model on an eye shaped domain that blinks; clearly blinking is important to establishing and refreshing the tear film (Li et al., 2014b). An *in silico* model of blinking could be very helpful for understanding the subtleties of tear film formation. An effort to develop these models is underway, but given the complexity of tear film dynamics and the manifold consequences, it is assured that more than one type of model will be required. The same can be said of experimental approaches. Close cooperation between mathematical and experimental approaches will continue to be mutually beneficial as the complexity of the approaches will increase to understand more complex aspects of the tear film and its interaction with the ocular surface.

7. Appendices

7.1 Mathematical model parameters

Here we give the detailed mathematical models solved to obtain the results in the text. We begin with a comprehensive list of the parameters used in the models. First, the dimensional quantities and values are given; then, non-dimensional parameters that arise after normalizing the variables in the problem are given. Detailed discussion of the meaning of nondimensional parameters are given in the sources.

Table 2. Dimensional parameters used in the model. The parameters α and A^* were estimated. They are only needed in combination to get h_{eq} =0.25μm in this work.

Parameter	Value	Quantity	Source
d'	3.5 μm	tear film thickness	(King-Smith et al., 2004)
L'	5 mm	length scale along film	
U	5 mm s^{-1}	velocity along film	(Maki et al., 2010)
v_0	1 - 30μm min^{-1}	initial thinning rate	(Nichols et al., 2005)

ρ	1000 kg m^{-3}	aqueous layer density	(Pandit et al., 1999)
μ	1.3x10^{-3} Pa s	viscosity	(water)
Vw	18 cm^3/mol	molar volume of water	
A^*	(1x10^{-17} m^3Pa)	Hamaker constant	(Winter et al., 2010)
α	1.87 x 10^{-2} m^2K Pa^{-1}	evaporation pressure coefficient	(Winter et al., 2010)
K'	1.5 x 10^5 $Kkg^{-1}m^2s$	nonequlibrium coefficient	(Li and Braun, 2012)
k	0.68 W m^{-1} K^{-1}	Thermal conductivity of tears	(water)
L_m	2.3 × 10^6 J kg^{-1}	Latent heat of vaporization	(water)
P_{corn}^{tiss}	12.1 μm/s	corneal permeability	(This workSec. 5.3.3)
P_{conj}^{tiss}	55.4 μm/s	conjunctival permeability	(Sec. 5.2.2This work)
h'_{eq}	$A^*\alpha/(6\pi\rho v_0 d^3)$=0.22μm	equilibrium film thickness	(Winter et al., 2010)
c_0	300 mOsM or 0.54mol %	isotonic concentration	(Lemp et al., 2011)
D_c	1.6 x 10^{-9} m^2s^{-1}	diffusivity of osmolarity (salt)	(Mota et al., 1991)
M_f	376 g/mol	molecular weight of sodium fluorescein	(Mota et al., 1991)
D_f	0.39 x 10^{-9} m^2s^{-1}	diffusivity of fluorescein	(Mota et al., 1991)
ε_f	7.6 x 10^4 $cm^{-1}M^{-1}$	molar extinction coefficient of fluorescein	(Mota et al., 1991)
f_{cr}	0.2%	critical fluorescein concentration	(Nichols et al., 2012)
f_0	0.01 – 0.2%	initial fluorescein concentration	(Nichols et al., 2012)

The flow resistance of the corneal epithelium, in the notation and units of Fatt and Weissman, (Fatt and Weissman, 1992) may be given as $R_t = R_{gc}T_{eye}/(P_f^{tiss}S_cV_w) = 8.06 \times 10^{11}$dyn s/cm. Here we have used the following: $S_c = 1.47\text{cm}^2$ is the corneal surface area,(Tiffany et al., 1998) $T_{eye} = 308$K is the ocular surface temperature (Efron et al., 1989; Mapstone, 1968) and $R_{gc} = 8.314 \times 10^7$dyn cm/mol/K is the universal gas constant. We note that R_t here is larger than the animal model estimate of Fatt and Weissman (Ch 6), so that the rate of osmosis is smaller than their estimate.

Table 3. Representative non-dimensional parameters that are indicative of the leveling and TBU models. These parameters are for a thinning rate of $v_0 = 4\mu$m/min and $P_{corn}^{tiss} = 12.1\ \mu$m/s. For the open-eye model of Sec. 5.3.5 and Appendix 7.6, slightly different parameters were used (P_{corn} and P_{conj} were only used in those sections and use the latter).

Parameter	Definiton	Value	Meaning
$\boldsymbol{\varepsilon}$	d'/L'	7×10^{-4}	Ratio of characteristic lengths
$\boldsymbol{h_{eq}}$	h'_{eq}/d	0.0616	Normalized minimum thickness
$\boldsymbol{P_c}$	$P_{corn}^{tiss} V_w c_0/(\varepsilon U)$	0.0185	Normalized constant permeability
$\boldsymbol{P_{corn}}$	$P_{corn}^{tiss} V_w c_0/(\varepsilon U)$	0.013	Normalized corneal permeability
$\boldsymbol{P_{conj}}$	$P_{conj}^{tiss} V_w c_0/(\varepsilon U)$	0.06	Normalized conjunctival permeability
$\boldsymbol{\phi}$	$\varepsilon_f f_{cr} d'$	0.141	Normalized Naperian optical density
$\mathbf{Pe}_c$	UL'/D_c	1.56×10^3	Ratio of advective to diffusive transport
$\mathbf{Pe}_f$	UL'/D_f	6.41×10^4	Ratio of advective to diffusive transport
$\boldsymbol{S}$	$\sigma\varepsilon^3/(\mu U)$	3.09×10^{-6}	Ratio of surface tension to viscous forces
$\boldsymbol{A}$	$A^*/(L'd'\mu U)$	6.11×10^{-6}	Ratio of van der Waals to viscous forces
$\boldsymbol{\delta}$	$\alpha\mu U/(\varepsilon 2L'\Delta T)$	38.2	Normalized evaporative pressure coefficient
$\boldsymbol{E}$	$k\Delta T/(d'L_m\varepsilon\rho U)$	241.	Normalized evaporation coefficient
$\boldsymbol{K}$	$kK'/(d'L_m)$	1.27×10^4	Nonequlibrium evaporation coefficient

7.2 FL equations and TF thinning

Following the works of Nichols et al 2012 and Braun et al 2012, calculate the fluorescent intensity for wide range of FL concentrations *f* using the relation

$$I = I_0 \frac{1 - e^{-\varphi h f}}{1 + f^2}. \qquad (9)$$

The variables *h* and *f* are the normalized thickness and FL concentration, respectively. The constant $\varphi = \varepsilon_f d' f_{cr}$ is non-dimenional version of the molar extinction coefficient ε_f, also known as the Naperian optical density. This expression for *I* is the product of the efficiency, which drops

off as the inverse square of the FL concentration, and the absorptance which increases to a constant value as f increases:

$$E_f = \frac{C_1}{1+f^2} \quad \text{and} \quad A_f = C_2\left(1 - e^{-\varphi h f}\right). \tag{10}$$

The product of the two constants C_1 and C_2 is I_0, the response scaling factor, which must be determined for each experimental set up. For a detailed discussion of the changes in FL intensity during TF thinning, see Braun et al 2014.

When thinning occurs, h and f are related via mass conservation; the problem was studied in detail in (Braun et al., 2014). Solute concentrations rise with evaporation and decreasing tear film thickness. Mass conservation for the spatially uniform case (that is, all dependent variables are independent of space) requires that the product of the thickness and a given solute is constant at all times. In our normalization, this would mean $hc = 1$ and $hf = f_0$; if one can solve for h, then one can compute c and f from these relations. Thus, the equations to solve that conserves water and solutes are:

$$\frac{dh}{dt} = P_c(c + 3Bf - 1) - J, \tag{11}$$

$$J = \frac{E}{K+h}(1 - \delta A h^{-3}), \tag{12}$$

$$hc = 1, \quad \text{and} \quad hf = f_0. \tag{13}$$

Because J, c and f are all positive, the equations show that the thickness decreases and the solute concentrations rise due to evaporation. The last equations are conservation of solutes, respectively for osmolarity and fluorescein. (A derivation is given in Braun et al. (2014).) The initial values at $t = 0$ are $h(0) = c(0) = 1, f(0) = f_0$, when normalized with d, c_0 and f_{cr}, respectively.

For these choices, and after normalizing the osmolarity with the isotonic value and the fluorescein concentration with the critical concentration ($f_{cr} = 0.2\%$, or 5.3 mOsM), the osmotic supply may be written as

$$P_c(c + 3Bf - 1). \tag{14}$$

Here P_c is the nondimensional permeability and B is the ratio of the characteristic concentrations, with each respectively given by

$$P_c = \frac{c_0 P_f^{tiss} V_w}{v_0} \quad \text{and} \quad B = \frac{f_{\mathrm{cr}}}{c_0}. \tag{15}$$

The factor of three in the osmotic supply appears because the fluorescein dissociates to two sodium ions and one dianionic fluorescein molecule in the pH range of tears (Evinger et al., 1991). Then, substitution gives $3B = 0.053$, and so there is small number multiplying the fluorescein concentration in the supply of water from the ocular surface. Thus, in all places in this paper, osmotic flow dure to f will be neglected in this paper.

7.3 Tangential flow over a model rough corneal surface

The equation that governs the film thickness dynamics without evaporation is a nonlinear partial differential equation which is difficult to solve:

$$\frac{\partial h}{\partial t}+\frac{\partial}{\partial x}\left(h^2\frac{1}{2\mu}\frac{\partial \sigma}{\partial x}+h^3\frac{\sigma}{3\mu}\frac{\partial^3 h}{\partial x^3}\right)=0. \qquad (16)$$

Here σ is the surface tension of the tear/air interface and μ is the viscosity of tears. There are partial derivatives of the thickness in both space and time (which represents the rate of change of h with respect to that variable while the other is held fixed).

The linearized analysis is considered first. Imagine a time-independent film of mean thickness, d', driven in the x direction by a constant surface tension gradient, dσ/dx, over a rough surface of height $z_c = Z_c e^{ik_c x}$ where the amplitude $|Z_c| \ll d'$. Suppose that the thickness of the film is

$$h = d' + He^{ik_c x}, \qquad (17)$$

where it is assumed that $|H| \ll d'$. It will be assumed that the surface tension gradient is small in that σ does not vary much over one wavelength of the rough surface.

In the steady state case assumed here, the total flux, q (mean velocity × thicknes; in Eq. (16), the sum in parentheses), must be independent of the location along the film x, which requires that

$$\frac{dq}{dx}=0. \qquad (18)$$

This flux may be considered to be the sum of two contributions, with one from the surface tension gradient flux, q_σ, and pressure gradient flux, q_p. The surface tension gradient and pressure gradient fluxs are given by, respectively,

$$q_\sigma=\frac{d\sigma}{dx}\frac{h^2}{2\mu}, \text{ and } q_p=-\left(\frac{\sigma}{3\mu}\right)h^3\frac{d^3(h+z_c)}{dx^3}. \qquad (19)$$

Using Equations (19) and linearizing, one finds

$$\frac{dq_\sigma}{dx}=\frac{d\sigma}{dx}\frac{d'}{\mu}Hik_c e^{ik_c x}, \text{ and } \frac{dq_p}{dx}=-\left(\frac{\sigma d'^3}{3\mu}\right)(H+Z_c)k_c^4\frac{\partial^3(h+z_c)}{\partial x^3}. \qquad (20)$$

Substituting Equations (20) into Eq. (18) and simplifying gives

$$H\left(3i\frac{d\sigma}{dx}-\sigma d' k_c^3\right)=Z_c\sigma d'^2 k_c^3 \qquad (21)$$

The relative amplitude of the air/tear film interface is given by

$$\frac{H+Z_c}{Z_c}=-\frac{i\alpha}{1-i\alpha}, \qquad (22)$$

where

$$\alpha = \frac{1}{\sigma}\frac{d\sigma}{dx}\frac{3}{d'^2 k_c^3}. \qquad (23)$$

The amplitude of surface roughness is therefore given by

$$\frac{|H + Z_c|}{|Z_c|} = \frac{\alpha}{\sqrt{1+\alpha^2}}. \qquad (24)$$

If the fluid motion is primarily caused by the surface tension gradient (the Marangoni effect), then the mean velocity (averaged over thickness) is approximately given (cf. Equation 19) by

$$u_m = \frac{d\sigma}{dx}\frac{d'}{2\mu}. \qquad (25)$$

Rearranging gives an estimate for the surface tension gradient if all of the other quantities are viewed as inputs:

$$\frac{d\sigma}{dx} = \frac{2\mu u_m}{d'}. \qquad (26)$$

Eliminating the surface tension gradient from (23) yields

$$\alpha = \frac{6\mu u_m}{\sigma d'^2 k_c^3}. \qquad (27)$$

Next, the second, time-dependent nonlinear model is discussed. The nonlinear thin film model is derived using so-called lubrication theory, which makes very effective approximations that exploit the thinness of the tear film (Braun 2012). The process reduces the problem to an equation for the thickness of the tear film, namely

$$\frac{\partial h}{\partial t} + \frac{h}{2}\frac{dX}{dt}\left(\frac{1-x}{1-X}\right) + \frac{\partial q}{\partial x} = 0, \quad q = \frac{h^3}{12}\frac{\partial}{\partial x}\left[S\frac{\partial^2(h+z)}{\partial x^2}\right]. \qquad (28)$$

On the moving domain $-X(t) \le x \le X(t)$; the ends move symmetrically on either side of $x = 0$. We used the boundary conditions

$$h(\pm X, t) = h_0 - z(\pm X) \quad \text{and} \quad q(\pm X, t) = \pm[h_e - z(\pm X)]\frac{dX}{dt}, \qquad (29)$$

where h_e is the thickness of the tear film that exists underneath the moving lid. The location of the corneal surface z is subtracted from the boundary value to keep the thickness constant as the lid moves over the ocular surface. We assumed $h_e = 1$ and $h_0 = 23$, both relative to the assumed nominal tear film thickness of $d = 3.5$ μm (King-Smith et al., 2004). For the initial condition, we used $X(0) = 0.3$ or 1 as indicated in the corresponding figure. For the initial tear film thickness, we used a polynomial function that gave a flat interior and a reasonably-sized meniscus:

$$h(x, 0) = h_{min} + (h_0 - h_{min})\left[\frac{x}{X(0)}\right]^{2m}. \qquad (30)$$

Here m is an exponent chosen to set the meniscus width; for $X(0) = 0.3$, we used typically used $m = 8$.

7.4 Mathematical model for leveling

In this section, simple tangential flow is studied without solutes; the first case considered is without evaporation or osmotic supply. The equation that governs the thickness dynamics in this case is a nonlinear partial differential equation which is difficult to solve:

$$\frac{\partial h}{\partial t} + \frac{\partial}{\partial x}\left(h^3 \frac{\sigma}{3\mu}\frac{\partial^3 h}{\partial x^3}\right) = 0, \qquad (31)$$

Here σ is the (assumed) constant surface tension of the tear/air interface and μ is the viscosity of tears. There are partial derivatives of the thickness in both space and time (which represents the rate of change of h with respect to that variable while the other is held fixed). In the tangentially immobile case, the tear/air interface is assumed to be far from "clean" and the presence of an insoluble surfactant is so strong that it renders the free surface immobile along itself. This limit is like having plastic wrap on top of the aqueous layer. The dynamics of the tear/air interface are then given by the same equation except that the three in the denominator is replaced by a 12. This will have the effect of slowing down the dynamics by a factor of four compared to the clean or stress free case.

Linearizing about d' for small h' gives, in the stress free case,

$$\frac{\partial h'}{\partial t} + \frac{d'^3\sigma}{3\mu}\frac{\partial^4 h'}{\partial x^4} = 0. \qquad (32)$$

This linear partial differential equation is much easier to solve, and one finds that

$$h'(x,t) = A_1 \exp\left[-\frac{d'^3\sigma}{3\mu}\left(\frac{2\pi}{\lambda_c}\right)^4 t\right]\cos\left(\frac{2\pi}{\lambda_c}x\right), \qquad (33)$$

where A_1 is an arbitrary constant. Thus the time to decay to half of the original amplitude (or half life) $t_{1/2}$ is given by solving

$$\exp\left[-\frac{d^3\sigma}{3\mu}\left(\frac{2\pi}{\lambda}\right)^4 t_{1/2}\right] = \frac{1}{2}. \qquad (34)$$

Solving for $t_{1/2}$ results in Eq. (5) in Section 5.2.1.

The nonlinear model with evaporation is now specified. The non-dimensional equations that we study are

$$\frac{\partial h}{\partial t} + \frac{\partial q}{\partial x} = -J, \qquad (35)$$

$$q = \frac{h^3}{3}\frac{\partial}{\partial x}\left(S\frac{\partial^2 h}{\partial x^2} + Ah^{-3}\right), \qquad (36)$$

$$J = \frac{E}{K+h}\left[1 - \delta\left(S\frac{\partial^2 h}{\partial x^2} + Ah^{-3}\right)\right]. \qquad (37)$$

Periodic boundary conditions are used on a domain corresponding to 1 cm for this model. Here the first equation is conservation of mass, saying that the rate of change of the tear film thickness h is set by the rate of change of the flux q along the film and that the thickness is reduced by the evaporative flux J. The second equation defines q as a derivative of the capillary pressure due to surface tension of the tear film surface (the term with S) and a van der Waals pressure term representing the wettability of the epithelial surface (the term with A); in terms of fluid mechanics, this term is a pressure gradient along the film. Finally, the last equation specifies J whereby the tear film loses water to the environment. We choose the non-dimensional quantities to match experimentally measured values (Braun, 2012; Li et al., 2014b; Li and Braun, 2012; Winter et al., 2010).

At the tear film surface, the model assumes that the lipid layer only has any effect by significantly slowing down the evaporation compared to that of an air/pure water interface. This model is that of Winter et al. (2010); this model does not take into account the transport of water vapor outside the tear film.

7.5 TF tangential flow with thinning and solutes

When the tear film is time dependent (dynamic) and contains solutes, the following non-dimensional model, appropriate for studying TBU, may be used:

$$\frac{\partial h}{\partial t} + \frac{\partial q}{\partial x} = P_c(c-1) - J, \qquad (38)$$

$$q = \frac{h^3}{3}\frac{\partial}{\partial x}\left(S\frac{\partial^2 h}{\partial x^2} + Ah^{-3}\right), \qquad (39)$$

$$J = \frac{E}{K+h}\left[1 - \delta\left(S\frac{\partial^2 h}{\partial x^2} + Ah^{-3}\right)\right], \qquad (40)$$

$$h\left(\frac{\partial c}{\partial t} + u\frac{\partial c}{\partial x}\right) = \frac{1}{\mathrm{Pe}_c}\frac{\partial}{\partial x}\left(h\frac{\partial c}{\partial x}\right) + P_c(c-1)c - Jc, \qquad (41)$$

$$h\left(\frac{\partial f}{\partial t} + u\frac{\partial f}{\partial x}\right) = \frac{1}{\mathrm{Pe}_f}\frac{\partial}{\partial x}\left(h\frac{\partial f}{\partial x}\right) + P_c(c-1)f - Jf \qquad (42)$$

Eq. (38) conserves water in the tear film that is evaporating with rate J. The more complex solute conservation equations are required in this case (Braun, 2012; Jensen and Grotberg, 1993). The evaporation term J was additionally given spatial distribution when breakup was studied. This was accomplished by making E dependent on x; as an example, we used

$$E = E_0 + E_1 e^{-\frac{1}{2}\left(\frac{x}{x_w}\right)^2}, \qquad (43)$$

where E_0 corresponds to a chosen background rate such as 2.5 μm/min and $E_1 = 9E_0$ caused a peak evaporation rate that is ten times larger than the background rate (25 μm/min in this example). Unless otherwise noted, we used $x_w = 0.026$ (non-dimensionally), corresponding to a width of six standard deviations being 0.78 mm. The Peclet numbers Pe_c and Pe_f measure the relative importance of flow and diffusion in transporting the respective solutes; they are defined and their values given in Appendix 7.1.

These equations were solved on the domain $-1 \le x \le 1$, when this coordinate was normalized with $L = 5$ mm representing half of the width of the palpebral fissure. Periodic boundary conditions were chosen because the ends were far enough away that they didn't affect the TBU dynamics, and because this allowed us to use a fast and efficient numerical method (Fourier spectral discretization in space with backward differentiation formulas in time via Matlab's ode15s function). The initial conditions were the constant values $h(x,0) = c(x,0) = 1$ and $f(x,0) = f_0$.

7.6 Eye-shaped domain models

We have solved for tear film flow on two-dimensional eye-shaped domains; as an abbreviation, we use the symbol Ω to represent the domain. The domain is created from a digital photograph of an eye. Selected points along the lid margin were used to fit four connected polynomials in Cartesian coordinates around the lid margin. Quadratic polynomials in *x* were used for the upper and lower lids, and ninth degree polynomials in *y* were used at the canthi. The high degree at the canthi was needed to ensure that the eye shape and its first four derivatives were all continuous. The boundary was required to be so smooth to avoid introducing error from the boundary into the fluid flow. Details of the boundary shape can be found in our previous papers (Li et al., 2014b; Maki et al., 2010; Maki et al., 2010). We have used this shape for several kinds of mathematical models, including the new results in Section 5.3.4 of this paper.

The two-dimensional PDEs that are solved within Ω are:

$$\frac{\partial h}{\partial t} + \nabla \cdot \boldsymbol{Q} = P_c(c-1) - J, \qquad (44)$$

$$\boldsymbol{Q} = \frac{h^3}{12}\nabla(S\nabla^2 h + Ah^{-3}), \qquad (45)$$

$$J = \frac{E}{K+h}[1 - \delta(S\nabla^2 h + Ah^{-3})], \qquad (46)$$

$$h\left(\frac{\partial c}{\partial t} + \boldsymbol{u}\cdot\nabla c\right) = \frac{1}{\mathrm{Pe}_c}\nabla\cdot\,(h\nabla c) + P_c(c-1)c - Jc, \qquad (47)$$

$$h\left(\frac{\partial f}{\partial t} + \boldsymbol{u}\cdot\nabla f\right) = \frac{1}{\mathrm{Pe}_f}\nabla\cdot\,(h\nabla f) + P_c(c-1)f - Jf. \qquad (48)$$

Here $\boldsymbol{Q}$ is the flux along the tear film, which is a vector function in this model, ∇ is the gradient operator in the plane of the substrate (model ocular surface), and $\boldsymbol{u} = \boldsymbol{Q}/h$ is the (depth-averaged) velocity along the film.

We need to specify boundary conditions around the edge of the domain corresponding to the lid margins; as an abbreviation, we denote the boundary with $\partial\Omega$. On $\partial\Omega$, we specify the thickness at the lid margins to be the constant value $h_0 = 13$ (corresponding to 65 μm) and the flux (amount) of fluid that enters the domain, $\boldsymbol{n}_b \cdot \boldsymbol{Q}|_{\partial\Omega} = Q_{lg}(s,t) + Q_p(s,t)$. The flux of fluid entering the domain is a sum of influx from the lacrimal gland (lg) and efflux via the puncta (p). They are complicated functions that are given in Li et al 2014a or Li et al 2014b. The flux boundary condition is shown as specific time in Fig. 33. We supply fluid into the tear film from a part of the lid margins that corresponds to the lacrimal gland for 5 s, and drain aqueous tear fluid from two locations on the lid margin corresponding to the puncta for the last 4 s of the same interval. Then, there is no flux for the next 5 s, and the cycle (of duration 10 s) repeats.

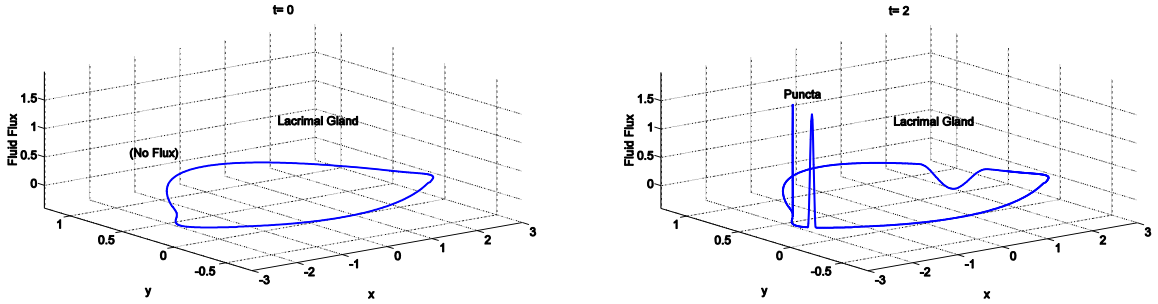

Fig. 33. Plots of flux boundary condition at two different times. When no flux occurs ($t = 0$ here), all points on the curve are at zero. At $t = 2$, both lacrimal gland supply and punctal drainage are active. Negative values at the lacrimal gland indicate an influx of fluid; positive values at the puncta indicate an efflux of fluid. (color on web only)

For the initial conditions, a smooth bowl-shaped tear film is used that is flat in the interior and increases at the lid margin with a meniscus; details appear in (Li et al., 2014b). The initial conditions for the concentrations are uniform (constant) in Ω. The osmolarity is always initially isotonic (c_0=302 mOsM in this section). The initial fluorescein concentration is either 0.05 or 1, when normalized with the critical concentration of $f_{cr} = 0.2\%$. In this section, we used $d' = 5$ μm, $\mu = 1.3 \times 10^{-3}$ Pa s (Tiffany, 1991), and $D_c = D_f = 2.6 \times 10^{-5}$ cm²/s after the properties used in Zubkov et al. (2012).

Acknowledgements

Supported by Grants 1022706 (RJB) from the National Science Foundation (NSF), R01EY021794 (CGB) and R01EY017951 (PEK-S) from the National Eye Institute (NEI). The content is solely the responsibility of the authors and does not necessarily represent the official views of the NSF, NEI,or the National Institutes of Health. The Institute for Mathematics and its Applications at the University of Minnesota also provided partial support during the completion of this work (RJB and LL). We thank Drs. Jason and Kelly Nichols for helpful discussion of some ideas presented here.

References

Acosta, M.C., Belmonte, C., Gallar, J., 2001. Sensory experiences in humans and single-unit activity in cats evoked by polymodal stimulation of the cornea. J Physiol 534, 511-525.

Aydemir, E., Breward, C.J., Witelski, T.P., 2011. The effect of polar lipids on tear film dynamics. Bull Math Biol 73, 1171-1201.

Baudouin, C., Aragona, P., Messmer, E.M., Tomlinson, A., Calonge, M., Boboridis, K.G., Akova, Y.A., Geerling, G., Labetoulle, M., Rolando, M., 2013. Role of hyperosmolarity in the pathogenesis and management of dry eye disease: proceedings of the OCEAN group meeting. Ocul Surf 11, 246-258.

Begley, C., Simpson, T., Liu, H., Salvo, E., Wu, Z., Bradley, A., Situ, P., 2013. Quantitative analysis of tear film fluorescence and discomfort during tear film instability and thinning. Invest Ophthalmol Vis Sci 54, 2645-2653.

Begley, C.G., Caffery, B., Nichols, K., Mitchell, G.L., Chalmers, R., 2002. Results of a dry eye questionnaire from optometric practices in North America. Adv Exp Med Biol 506, 1009-1016.

Begley, C.G., Himebaugh, N., Renner, D., Liu, H., Chalmers, R., Simpson, T., Varikooty, J., 2006. Tear breakup dynamics: a technique for quantifying tear film instability. Optom Vis Sci 83, 15-21.

Berger, R.E., Corrsin, S., 1974. A surface tension gradient mechanism for driving the pre-corneal tear film after a blink. J Biomech 7, 225-238.

Braun, R., King-Smith, P., 2007. Model problems for the tear film in a blink cycle: single-equation models. J Fluid Mech 586, 465-490.

Braun, R.J., 2012. Dynamics of the Tear Film. Annual Review of Fluid Mechanics, Vol 44 44, 267-297.

Braun, R.J., Fitt, A.D., 2003. Modelling drainage of the precorneal tear film after a blink. Math Med Biol 20, 1-28.

Braun, R.J., Gewecke, N.R., Begley, C.G., King-Smith, P.E., Siddique, J.I., 2014. A model for tear film thinning with osmolarity and fluorescein. Invest Ophthalmol Vis Sci 55, 1133-1142.

Bron, A.J., Tiffany, J.M., Gouveia, S.M., Yokoi, N., Voon, L.W., 2004. Functional aspects of the tear film lipid layer. Exp Eye Res 78, 347-360.

Bron, A.J., Tiffany, J.M., Yokoi, N., Gouveia, S.M., 2002. Using osmolarity to diagnose dry eye: a compartmental hypothesis and review of our assumptions. Adv Exp Med Biol 506, 1087-1095.

Bron, A.J., Tomlinson, A., Foulks, G.N., Pepose, J.S., Baudouin, C., Geerling, G., Nichols, K.K., Lemp, M.A., 2014. Rethinking dry eye disease: a perspective on clinical implications. Ocul Surf 12, S1-31.

Bruna, M., Breward, C., 2014. The influence of non-polar lipids on tear film dynamics. J Fluid Mech 746, 565-605.

Casalini, T., Salvalaglio, M., Perale, G., Masi, M., Cavallotti, C., 2011. Diffusion and aggregation of sodium fluorescein in aqueous solutions. J Phys Chem B 115, 12896-12904.

Chen, Z., Tong, L., Li, Z., Yoon, K.C., Qi, H., Farley, W., Li, D.Q., Pflugfelder, S.C., 2008. Hyperosmolarity-induced cornification of human corneal epithelial cells is regulated by JNK MAPK. Invest Ophthalmol Vis Sci 49, 539-549.

Cruz, A.A., Garcia, D.M., Pinto, C.T., Cechetti, S.P., 2011. Spontaneous eyeblink activity. Ocul Surf 9, 29-41.

Deng, Q., Braun, R.J., Driscoll, T.A., King-Smith, P.E., 2013. A Model for the Tear Film and Ocular Surface Temperature for Partial Blinks. Interfacial Phen Ht Trans 1, 357-381.

Denoyer, A., Rabut, G., Baudouin, C., 2012. Tear film aberration dynamics and vision-related quality of life in patients with dry eye disease. Ophthalmology 119, 1811-1818.
DEWS, 2007. The definition and classification of dry eye disease: Report of the Definition and Classification Subcommittee of the International Dry Eye WorkShop (2007). Ocul Surf 5, 75-92.
Dingeldein, S.A., Klyce, S.D., 1989. The topography of normal corneas. Arch Ophthalmol 107, 512-518.
Doane, M.G., 1980. Interactions of eyelids and tears in corneal wetting and the dynamics of the normal human eyeblink. Am J Ophthalmol 89, 507-516.
Doane, M.G., 1981. Blinking and the mechanics of the lacrimal drainage system. Ophthalmology 88, 844-851.
Doane, M.G., 1989. An instrument for in vivo tear film interferometry. Optom Vis Sci 66, 383-388.
Dubra, A., Paterson, C., Dainty, C., 2004. Study of the tear topography dynamics using a lateral shearing interferometer. Opt Express 12, 6278-6288.
Efron, N., Young, G., Brennan, N.A., 1989. Ocular surface temperature. Curr Eye Res 8, 901-906.
Evinger, C., Manning, K.A., Sibony, P.A., 1991. Eyelid movements. Mechanisms and normal data. Invest Ophthalmol Vis Sci 32, 387-400.
Fatt, I., 1991. Observations of tear film break up on model eyes. CLAO Journal 17, 267-281.
Fatt, I., Weissman, B.A., 1992. Physiology of the Eye: An Introduction to the Vegetative Functions. Elsevier Science.
Ferrer-Blasco, T., Garcia-Lazaro, S., Montes-Mico, R., Cervino, A., Gonzalez-Meijome, J.M., 2010. Dynamic changes in the air-tear film interface modulation transfer function. Graefes Arch Clin Exp Ophthalmol 248, 127-132.
Fogt, N., King-Smith, P.E., Tuell, G., 1998. Interferometric measurement of tear film thickness by use of spectral oscillations. J Opt Soc Am A Opt Image Sci Vis 15, 268-275.
Gaffney, E.A., Tiffany, J.M., Yokoi, N., Bron, A.J., 2010. A mass and solute balance model for tear volume and osmolarity in the normal and the dry eye. Prog Retin Eye Res 29, 59-78.
Gaskell, P.H., Jimack, P.K., Sellier, M., Thompson, H.M., 2006. Flow of evaporating, gravity-driven thin liquid films over topography. Phys Fluids 18.
Gilbard, J.P., Farris, R.L., Santamaria, J., 2nd, 1978. Osmolarity of tear microvolumes in keratoconjunctivitis sicca. Arch Ophthalmol 96, 677-681.
Goto, E., Tseng, S.C., 2003. Kinetic analysis of tear interference images in aqueous tear deficiency dry eye before and after punctal occlusion. Invest Ophthalmol Vis Sci 44, 1897-1905.
Goto, T., Zheng, X., Okamoto, S., Ohashi, Y., 2004. Tear film stability analysis system: introducing a new application for videokeratography. Cornea 23, S65-70.
Govindarajan, B., Gipson, I.K., 2010. Membrane-tethered mucins have multiple functions on the ocular surface. Exp Eye Res 90, 655-663.
Guillon, M., Maissa, C., 2010. Tear film evaporation--effect of age and gender. Cont Lens Anterior Eye 33, 171-175.
Harrison, W.W., Begley, C.G., Liu, H., Chen, M., Garcia, M., Smith, J.A., 2008. Menisci and fullness of the blink in dry eye. Optom Vis Sci 85, 706-714.
Heryudono, A., Braun, R.J., Driscoll, T.A., Maki, K.L., Cook, L.P., King-Smith, P.E., 2007. Single-equation models for the tear film in a blink cycle: realistic lid motion. Math Med Biol 24, 347-377.
Himebaugh, N.L., Begley, C.G., Bradley, A., Wilkinson, J.A., 2009. Blinking and tear break-up during four visual tasks. Optom Vis Sci 86, E106-114.
Himebaugh, N.L., Nam, J., Bradley, A., Liu, H., Thibos, L.N., Begley, C.G., 2012. Scale and spatial distribution of aberrations associated with tear breakup. Optom Vis Sci 89, 1590-1600.
Himebaugh, N.L., Wright, A.R., Bradley, A., Begley, C.G., Thibos, L.N., 2003. Use of retroillumination to visualize optical aberrations caused by tear film break-up. Optom Vis Sci 80, 69-78.
Holly, F.J., 1973. Formation and rupture of the tear film. Exp Eye Res 15, 515-525.

Howison, S.D., Moriarty, J.A., Ockendon, J.R., Terrill, E.L., Wilson, S.K., 1997. A mathematical model for drying paint layers. Journal of Engineering Mathematics 32, 377-394.
Iskander, D.R., Collins, M.J., 2005. Applications of high-speed videokeratoscopy. Clin Exp Optom 88, 223-231.
Jensen, O., Grotberg, J., 1993. The spreading of heat or soluble surfactant along a thin liquid film. Phys Fluids A 5, 58.
Jones, M.B., McElwain, D.L., Fulford, G.R., Collins, M.J., Roberts, A.P., 2006. The effect of the lipid layer on tear film behaviour. Bull Math Biol 68, 1355-1381.
Jones, M.B., Please, C.P., McElwain, D.L., Fulford, G.R., Roberts, A.P., Collins, M.J., 2005. Dynamics of tear film deposition and draining. Math Med Biol 22, 265-288.
Kalliadasis, S., Homsy, G.M., 2001. Stability of free-surface thin-film flows over topography. J Fluid Mech 448, 387-410.
Keech, A., Senchyna, M., Jones, L., 2013. Impact of time between collection and collection method on human tear fluid osmolarity. Curr Eye Res 38, 428-436.
Khanal, S., Millar, T.J., 2010. Nanoscale phase dynamics of the normal tear film. Nanomedicine 6, 707-713.
Kimball, S.H., King-Smith, P.E., Nichols, J.J., 2010. Evidence for the major contribution of evaporation to tear film thinning between blinks. Invest Ophthalmol Vis Sci 51, 6294-6297.
King-Smith, P.E., Bailey, M.D., Braun, R.J., 2013a. Four characteristics and a model of an effective tear film lipid layer (TFLL). Ocul Surf 11, 236-245.
King-Smith, P.E., Fink, B.A., Fogt, N., Nichols, K.K., Hill, R.M., Wilson, G.S., 2000. The thickness of the human precorneal tear film: evidence from reflection spectra. Invest Ophthalmol Vis Sci 41, 3348-3359.
King-Smith, P.E., Fink, B.A., Hill, R.M., Koelling, K.W., Tiffany, J.M., 2004. The thickness of the tear film. Curr Eye Res 29, 357-368.
King-Smith, P.E., Fink, B.A., Nichols, J.J., Nichols, K.K., Braun, R.J., McFadden, G.B., 2009. The contribution of lipid layer movement to tear film thinning and breakup. Invest Ophthalmol Vis Sci 50, 2747-2756.
King-Smith, P.E., Fink, B.A., Nichols, J.J., Nichols, K.K., Hill, R.M., 2006. Interferometric imaging of the full thickness of the precorneal tear film. J Opt Soc Am A Opt Image Sci Vis 23, 2097-2104.
King-Smith, P.E., Kimball, S.H., Nichols, J.J., 2014. Tear film interferometry and corneal surface roughness. Invest Ophthalmol Vis Sci 55, 2614-2618.
King-Smith, P.E., Nichols, J.J., Braun, R.J., Nichols, K.K., 2011. High resolution microscopy of the lipid layer of the tear film. Ocul Surf 9, 197-211.
King-Smith, P.E., Nichols, J.J., Nichols, K.K., Fink, B.A., Braun, R.J., 2008. Contributions of evaporation and other mechanisms to tear film thinning and break-up. Optom Vis Sci 85, 623-630.
King-Smith, P.E., Ramamoorthy, P., Braun, R.J., Nichols, J.J., 2013b. Tear film images and breakup analyzed using fluorescent quenching. Invest Ophthalmol Vis Sci 54, 6003-6011.
King-Smith, P.E., Reuter, K.S., Braun, R.J., Nichols, J.J., Nichols, K.K., 2013c. Tear film breakup and structure studied by simultaneous video recording of fluorescence and tear film lipid layer images. Invest Ophthalmol Vis Sci 54, 4900-4909.
Klyce, S.D., Russell, S.R., 1979. Numerical solution of coupled transport equations applied to corneal hydration dynamics. J Physiol 292, 107-134.
Knop, E., Knop, N., Millar, T., Obata, H., Sullivan, D.A., 2011. The international workshop on meibomian gland dysfunction: report of the subcommittee on anatomy, physiology, and pathophysiology of the meibomian gland. Invest Ophthalmol Vis Sci 52, 1938-1978.
Koh, S., Maeda, N., Hirohara, Y., Mihashi, T., Bessho, K., Hori, Y., Inoue, T., Watanabe, H., Fujikado, T., Tano, Y., 2008. Serial measurements of higher-order aberrations after blinking in patients with dry eye. Invest Ophthalmol Vis Sci 49, 133-138.

Kojima, T., Ishida, R., Dogru, M., Goto, E., Takano, Y., Matsumoto, Y., Kaido, M., Ohashi, Y., Tsubota, K., 2004. A new noninvasive tear stability analysis system for the assessment of dry eyes. Invest Ophthalmol Vis Sci 45, 1369-1374.
Leiske, D.L., Miller, C.E., Rosenfeld, L., Cerretani, C., Ayzner, A., Lin, B., Meron, M., Senchyna, M., Ketelson, H.A., Meadows, D., Srinivasan, S., Jones, L., Radke, C.J., Toney, M.F., Fuller, G.G., 2012. Molecular structure of interfacial human meibum films. Langmuir 28, 11858-11865.
Lemp, M.A., Bron, A.J., Baudouin, C., Benitez Del Castillo, J.M., Geffen, D., Tauber, J., Foulks, G.N., Pepose, J.S., Sullivan, B.D., 2011. Tear osmolarity in the diagnosis and management of dry eye disease. Am J Ophthalmol 151, 792-798 e791.
Leung, B.K., Bonanno, J.A., Radke, C.J., 2011. Oxygen-deficient metabolism and corneal edema. Prog Retin Eye Res 30, 471-492.
Levin, M.H., Kim, J.K., Hu, J., Verkman, A.S., 2006. Potential difference measurements of ocular surface Na+ absorption analyzed using an electrokinetic model. Invest Ophthalmol Vis Sci 47, 306-316.
Levin, M.H., Verkman, A.S., 2004. Aquaporin-dependent water permeation at the mouse ocular surface: in vivo microfluorimetric measurements in cornea and conjunctiva. Invest Ophthalmol Vis Sci 45, 4423-4432.
Li, L., Braun, R.J., Driscoll, T.A., Henshaw, W.D., Banks, J.W., King-Smith, P.E., 2014a. Computed Tear Film and Osmolarity Dynamics on an Eye-Shaped Domain. Submitted, 37.
Li, L., Braun, R.J., Maki, K.L., Henshaw, W.D., King-Smith, P.E., 2014b. Tear film dynamics with evaporation, wetting, and time-dependent flux boundary condition on an eye-shaped domain. Phys Fluids 26, 052101.
Li, L.F., Braun, R.J., 2012. A model for the human tear film with heating from within the eye. Phys Fluids 24.
Liu, H., Begley, C., Chen, M., Bradley, A., Bonanno, J., McNamara, N.A., Nelson, J.D., Simpson, T., 2009. A link between tear instability and hyperosmolarity in dry eye. Invest Ophthalmol Vis Sci 50, 3671-3679.
Liu, H., Begley, C.G., Chalmers, R., Wilson, G., Srinivas, S.P., Wilkinson, J.A., 2006. Temporal progression and spatial repeatability of tear breakup. Optom Vis Sci 83, 723-730.
Liu, H., Thibos, L., Begley, C.G., Bradley, A., 2010. Measurement of the time course of optical quality and visual deterioration during tear break-up. Invest Ophthalmol Vis Sci 51, 3318-3326.
Maki, K.L., Braun, R.J., Driscoll, T.A., King-Smith, P.E., 2008. An overset grid method for the study of reflex tearing. Math Med Biol 25, 187-214.
Maki, K.L., Braun, R.J., Henshaw, W.D., King-Smith, P.E., 2010. Tear film dynamics on an eye-shaped domain I: pressure boundary conditions. Math Med Biol 27, 227-254.
Maki , K.L., Braun, R.J., Ucciferro, P., Henshaw, W.D., King-Smith, P.E., 2010. Tear film dynamics on an eye-shaped domain. Part 2. Flux boundary conditions. J Fluid Mech 647, 361-390.
Mapstone, R., 1968. Measurement of corneal temperature. Exp Eye Res 7, 237-243.
McDonald, J.E., 1969. Surface phenomena of the tear film. Am J Ophthalmol 67, 56-64.
Mochizuki, H., Yamada, M., Hatou, S., Tsubota, K., 2009. Turnover rate of tear-film lipid layer determined by fluorophotometry. Br J Ophthalmol 93, 1535-1538.
Montes-Mico, R., Alio, J.L., Charman, W.N., 2005. Dynamic changes in the tear film in dry eyes. Invest Ophthalmol Vis Sci 46, 1615-1619.
Montes-Mico, R., Cervino, A., Ferrer-Blasco, T., Garcia-Lazaro, S., Madrid-Costa, D., 2010. The tear film and the optical quality of the eye. Ocul Surf 8, 185-192.
Mota, M.C., Carvalho, P., Ramalho, J., Leite, E., 1991. Spectrophotometric analysis of sodium fluorescein aqueous solutions. Determination of molar absorption coefficient. Int Ophthalmol 15, 321-326.

Nemeth, J., Erdelyi, B., Csakany, B., Gaspar, P., Soumelidis, A., Kahlesz, F., Lang, Z., 2002. High-speed videotopographic measurement of tear film build-up time. Invest Ophthalmol Vis Sci 43, 1783-1790.
Nichols, J.J., King-Smith, P.E., 2003. Thickness of the pre- and post-contact lens tear film measured in vivo by interferometry. Invest Ophthalmol Vis Sci 44, 68-77.
Nichols, J.J., King-Smith, P.E., Hinel, E.A., Thangavelu, M., Nichols, K.K., 2012. The use of fluorescent quenching in studying the contribution of evaporation to tear thinning. Invest Ophthalmol Vis Sci 53, 5426-5432.
Nichols, J.J., Mitchell, G.L., King-Smith, P.E., 2005. Thinning rate of the precorneal and prelens tear films. Invest Ophthalmol Vis Sci 46, 2353-2361.
Norn, M.S., 1969. Desiccation of the precorneal film. I. Corneal wetting-time. Acta Ophthalmol 47, 865-880.
Orchard, S.E., 1962. On surface leveling in viscous liquids and gels. Appl. Sci. Res. A 11, 451-464.
Owens, H., Phillips, J., 2001. Spreading of the tears after a blink: velocity and stabilization time in healthy eyes. Cornea 20, 484-487.
Pandit, J.C., Nagyova, B., Bron, A.J., Tiffany, J.M., 1999. Physical properties of stimulated and unstimulated tears. Exp Eye Res 68, 247-253.
Parra, A., Gonzalez-Gonzalez, O., Gallar, J., Belmonte, C., 2014. Tear fluid hyperosmolality increases nerve impulse activity of cold thermoreceptor endings of the cornea. Pain 155, 1481-1491.
Peng, C.C., Cerretani, C., Braun, R.J., Radke, C.J., 2014. Evaporation-driven instability of the precorneal tear film. Adv Colloid Interface Sci 206, 250-264.
Riquelme, R., Lira, I., P´erez-L´opez, C., Rayas, J.A., Rodr´ıguez-Vera, R., 2007. Interferometric measurement of a diffusion coefficient: comparison of two methods and uncertainty analysis. J. Phys. D: Appl. Phys. 40, 2769 - 2776.
Rosenfeld, L., Cerretani, C., Leiske, D.L., Toney, M.F., Radke, C.J., Fuller, G.G., 2013. Structural and rheological properties of meibomian lipid. Invest Ophthalmol Vis Sci 54, 2720-2732.
Schaumberg, D.A., Sullivan, D.A., Buring, J.E., Dana, M.R., 2003. Prevalence of dry eye syndrome among US women. Am J Ophthalmol 136, 318-326.
Schiffman, R.M., Christianson, M.D., Jacobsen, G., Hirsch, J.D., Reis, B.L., 2000. Reliability and validity of the Ocular Surface Disease Index. Arch Ophthalmol 118, 615-621.
Schwartz, L., Cairncross, R., Weidner, D., 1996. Anomalous behavior during leveling of thin coating layers with surfactant. Phys Fluids 8, 1693-1695.
Sharma, A., Ruckenstein, E., 1985. Mechanism of tear film rupture and its implications for contact lens tolerance. Am J Optom Physiol Opt 62, 246-253.
Szczesna, D.H., Alonso-Caneiro, D., Iskander, D.R., Read, S.A., Collins, M.J., 2010. Lateral shearing interferometry, dynamic wavefront sensing, and high-speed videokeratoscopy for noninvasive assessment of tear film surface characteristics: a comparative study. J Biomed Opt 15, 037005.
Szczesna, D.H., Jaronski, J., Kasprzak, H.T., Stenevi, U., 2006. Interferometric measurements of dynamic changes of tear film. J Biomed Opt 11, 34028.
Szczesna, D.H., Kasprzak, H.T., 2009. Numerical analysis of interferograms for evaluation of tear film build-up time. Ophthalmic Physiol Opt 29, 211-218.
Szczesna, D.H., Kasprzak, H.T., Jaronski, J., Rydz, A., Stenevi, U., 2007. An interferometric method for the dynamic evaluation of the tear film. Acta Ophthalmol Scand 85, 202-208.
Tiffany, J.M., 1991. The viscosity of human tears. Int Ophthalmol 15, 371-376.
Tiffany, J.M., Todd, B.S., Baker, M.R., 1998. Computer-assisted calculation of exposed area of the human eye. Adv Exp Med Biol 438, 433-439.
Tomlinson, A., Khanal, S., Ramaesh, K., Diaper, C., McFadyen, A., 2006. Tear film osmolarity: determination of a referent for dry eye diagnosis. Invest Ophthalmol Vis Sci 47, 4309-4315.
Tutt, R., Bradley, A., Begley, C., Thibos, L.N., 2000. Optical and visual impact of tear break-up in human eyes. Invest Ophthalmol Vis Sci 41, 4117-4123.

Uchino, M., Nishiwaki, Y., Michikawa, T., Shirakawa, K., Kuwahara, E., Yamada, M., Dogru, M., Schaumberg, D.A., Kawakita, T., Takebayashi, T., Tsubota, K., 2011. Prevalence and risk factors of dry eye disease in Japan: Koumi study. Ophthalmology 118, 2361-2367.
Varikooty, J., Simpson, T.L., 2009. The interblink interval I: the relationship between sensation intensity and tear film disruption. Invest Ophthalmol Vis Sci 50, 1087-1092.
Versura, P., Profazio, V., Campos, E.C., 2010. Performance of tear osmolarity compared to previous diagnostic tests for dry eye diseases. Curr Eye Res 35, 553-564.
Viso, E., Rodriguez-Ares, M.T., Gude, F., 2009. Prevalence of and associated factors for dry eye in a Spanish adult population (the Salnes Eye Study). Ophthalmic Epidemiol 16, 15-21.
Webber, W.R., Jones, D.P., 1986. Continuous fluorophotometric method of measuring tear turnover rate in humans and analysis of factors affecting accuracy. Med Biol Eng Comput 24, 386-392.
Wilson, S.E., Klyce, S.D., 1991. Quantitative descriptors of corneal topography. A clinical study. Arch Ophthalmol 109, 349-353.
Winter, K.N., Anderson, D.M., Braun, R.J., 2010. A model for wetting and evaporation of a post-blink precorneal tear film. Math Med Biol 27, 211-225.
Wong, H., Fatt, I.I., Radke, C.J., 1996. Deposition and Thinning of the Human Tear Film. J Colloid Interface Sci 184, 44-51.
Wu, Z., Begley, C.G., Situ, P., Simpson, T., Liu, H., 2014. The effects of mild ocular surface stimulation and concentration on spontaneous blink parameters. Curr Eye Res 39, 9-20.
Zhang, Y.L., Matar, O.K., Craster, R.V., 2003. Analysis of tear film rupture: effect of non-Newtonian rheology. J Colloid Interface Sci 262, 130-148.
Zubkov, V.S., Breward, C.J., Gaffney, E.A., 2012. Coupling fluid and solute dynamics within the ocular surface tear film: a modelling study of black line osmolarity. Bull Math Biol 74, 2062-2093.